Technische Universität München
Fakultät für Physik
Lehrstuhl für Experimentalphysik E21

Further developments and applications of radiography and tomography with thermal and cold neutrons

Nikolay Kardjilov

Vollständiger Abdruck der von der Fakultät für Physik der Technischen Universität München zur Erlangung des akademischen Grades eines

Doktors der Naturwissenschaften

genehmigten Dissertation.

Vorsitzender:	Univ.-Prof. Dr. A. Groß
Prüfer der Dissertation:	1. Univ.-Prof. Dr. W. Gläser
	2. Univ.-Prof. Dr. W. Petry

Die Dissertation wurde am 28.04.2003 bei der Technischen Universität München eingereicht und durch die Fakultät für Physik am 25.06.2003 angenommen.

Contents

Abstract

English

In the current study various new experimental methods and computation procedures in the field of neutron radiography and tomography are presented. These methods have a significant technical importance in the non-destructive material investigations. Different techniques for a contrast enhancement, contrast variations and an increase of the image sharpness were developed.

In a beam geometry with a high lateral coherency of the neutron waves for the first time phase contrast radiography experiments with polychromatic neutrons were performed and analytically simulated. Therewith very fine structures were visualized which was impossible with the standard absorption radiography technique. By the utilization of a neutron velocity selector radiography and tomography experiments below and above the Bragg cut offs for objects, composed from different materials, were performed and the possibility for a material identification was tested. Using the method of the neutron topography the quality of single crystals was investigated.

For some of these experiments Monte Carlo simulations were performed using the powerful MCNP-code. This method was used also for the development of a mobile neutron radiography setup.

Some of the achieved developments will be used at the radiography and tomography facilities at the new research reactor FRM II in Munich, Germany.

Abstract

Deutsch

In der vorliegenden Arbeit werden verschiedene neue experimentelle Methoden und Rechenverfahren aus dem Gebiet der Radiographie und Tomographie mit Neutronen vorgestellt. Diese Durchstrahlungsverfahren gewinnen zunehmend technische Bedeutung für die zerstörungsfrei Materialprüfung. Es wurden verschiedene Verfahren zur Kontrastverstärkung, Kontrastvariation und Abbildungsschärfe theoretisch und experimentell untersucht.

In einer Strahlgeometrie mit großer lateraler Kohärenz der Neutronenwelle konnten erstmals Phasenkontrast-Radiographien mit polychromatischen Neutronen abgebildet und rechnerisch analysiert werden. Damit können Strukturen deutlich gemacht werden, die in normaler Absorptionsradiographie nicht sichtbar sind.

Unter Verwendung eines Neutronengeschwindigkeitsselektors wurden Untersuchungen diesseits und jenseits der Bragg-Kanten von Objekten, die aus verschiedenen Materialen zusammengesetzt waren, ausgeführt und die Möglichkeit einer Materialidentifikation geprüft. Mit der Methode der Neutronentopographie wurde die Qualität von Einkristallen untersucht.

Für eine Reihe dieser Experimente wurden Monte-Carlo Simulationen mit dem mächtigen MCNP-Code durchgeführt. Diese Methode wurde auch in Rahmen der Entwicklung einer tragbaren Neutronenquelle verwendet.

Einige der hier erarbeiteten Fortschritte sollen an den Radiographie- und Tomographieanlagen des neuen Forschungsreaktors FRM-II angewendet werden.

to my parents

Chapter 1: Introduction

The radiography with thermal and cold neutrons is a powerful non-destructive method for the investigation of materials and samples from various fields of activity. The radiography image is formed due to an attenuation of the neutron beam at its propagation through the investigated object. Different types of position-sensitive detector systems are available for the recording of the radiography information – photographic films, imaging plates, electronic camera based systems, flat panels and track-etch foils. From a number of radiography images obtained at different rotation angles of the sample a three-dimensional representation of the object can be computed. The method is known as neutron computed tomography.

The current study treats new experimental and computation methods in the field of neutron radiography and tomography. The following methods are presented:

Phase contrast radiography is an experimental method which is used for the visualisation of materials with low neutron absorption properties. Instead of conventional radiography the phase contrast imaging visualises not only the beam absorption but also the phase shifts induced by the sample. For this purpose a neutron beam with high spatial but not necessarily chromatic coherence is needed.

Energy selective radiography and tomography exploits partially monochromatised beams. This allows to change the material contrast in radiography images due to the energy-dependent attenuation properties of the materials. In the cold neutron energy range energy selective radiographs above and below the Bragg cut off for the investigated crystalline material can be performed.

Neutron topography visualises the diffracted beam from crystal objects. It allows to exploit the scattering information as complete as possible in a reasonable time. In comparison with the conventional micro beam techniques where only a small region of the sample is irradiated, in the topography experiments a large beam in the order of several square centimeters is used.

The *computation methods* are based on the application of the powerful Monte Carlo code for particle transport simulations – MCNP. It is used for the design and

optimization of a mobile neutron source as well as for a complete simulation of radiography experiments helping to estimate the contribution of undesired experimental effects as neutron scattering and beam hardening to the radiography imaging.

The main developments described in the current study will be used as a basis for further methodological improvements at the new thermal/cold neutron radiography facility ANTARES which is now under construction at the research reactor FRM II at TU-Munich, Germany.

Chapter 2: Phase Contrast Neutron Radiography

2.1 Basics

The wave-particle dualism and in particular the *de Broglie* postulate [Bro23] allows us to treat the neutron beam as particles possessing a defined mass and a kinetic energy or to regard it as a propagating wave with corresponding amplitude and a wavelength. In case of conventional radiography we are mainly interested in the intensity variations produced by absorption in the investigated object, where the intensity is usually considered in terms of particles as the number of neutrons transmitted through a defined area for a defined time. If we translate this in terms of a wave representation, the intensity variations behind the object will be related to the superposition of secondary spherical waves generated by the scattering centres in the object. For a transmission of waves with the same frequency through a matter, a measure of the relative shift between the waves can be introduced by their phase. The different materials or material thicknesses provide different wave shift relative to the wave propagation in vacuum, which are called phase variations. Some objects produce much bigger phase than intensity variations, the so-called phase objects. Many objects of interest in biology and material science can be considered as phase objects. They cannot be visualized with standard radiography methods, because of their low absorption properties. The phase contrast technique is a very powerful method for imaging of such kind of objects. In this case the phase changes obtained by the propagation of an appropriate radiation through the sample are transformed to intensity variations detected by a position-sensitive detector. The Dutch physicist Fritz Zernike received the Nobel Prize in 1953 for inventing the optical phase contrast [Bor59], which led to a break-through in medicine and biology by making essentially transparent cell or bacteria samples clearly visible under a microscope. There are a lot of examples of phase contrast imaging using monochromatic light or synchrotron radiation [Bar98], [Clo96], [Baj00]. Recently a phase contrast imaging with neutrons was also reported [All00]. A monochromatic radiation with high order of spatial coherence is usually used for phase contrast

imaging. The synchrotron sources are very suitable for such purposes because of the possible small size and high intensity of their beams [Clo99]. These conditions combined with a long source to sample distance l give an extremely high transverse coherence length l_t. The requirement for highly monochromatic radiation and the sophisticated optics make the use of phase-contrast technique non-trivial.

The phase contrast imaging with neutrons at steady neutron sources has its own specific properties. The main problem is the very low neutron intensity. The monochromatization of the beam reduces the intensity by 2-3 orders of magnitude. If we want to achieve a higher coherence length then a small pinhole should be used. So that for a typical flux of ~10^8 n/cm^{2}s after the monochromatization and the spatial reduction of the beam (pinhole with a diameter of 500 μm) only ~ 10^3 n/cm^{2}s will be available at the sample position for a phase-contrast experiment. This leads of course to a considerable increase of the measuring time, reaching several days at the typical neutron flux mentioned above. Therefore the phase contrast neutron imaging until now was a very exotic technique almost without any practical applications.

We can gain more intensity if a polychromatic beam is used. The first experiments based on an x-ray source having high spatial, but essentially no chromatic coherence are demonstrated in [Wil96]. The shown successful phase contrast images with polychromatic radiation gave us an inspiration to perform phase contrast experiments with a polychromatic thermal neutron beam available at the thermal neutron radiography setup NEUTRA at PSI.

2.2 Theoretical considerations

First we will start with the classical representation of the phase-contrast effect as a whole and after that a more detailed description in terms of Fresnel diffraction will be given.

A. Classical phase-contrast effect

For waves with a wavelength λ a complex refractive index can be introduced at their propagation through a defined medium as following:

$$n(x, y, z, l) = 1 - d(x, y, z, l) - ib(x, y, z, l) \tag{2.1}$$

where the real part d corresponds to the phase of the propagating wave and b represents the absorption in the medium. In that terminology one can say that the phase contrast imaging exploits the real part of the refractive index 1-d and the neutron radiography the imaginary part b so that the definition for a phase object can be given as an object of which the refractive index possesses a negligible imaginary part b.

The definition of phase is usually introduced in case of a coherent wavefield. Such wavefields are described by a complex function $u(\mathbf{r}) = [I(\mathbf{r})]^{1/2}\exp[i\,j\,(\mathbf{r})]$, where $\mathbf{r}$ is the position in space, $I(\mathbf{r})$ is the intensity of the wave, and $j\,(\mathbf{r})$ is its phase at a position $\mathbf{r}$. The surfaces where $j\,(\mathbf{r})$ is constant are represented as wavefronts. The phase gradient $\nabla j\,(\mathbf{r})$ describes the local propagation direction, as shown in Fig. 2.1.

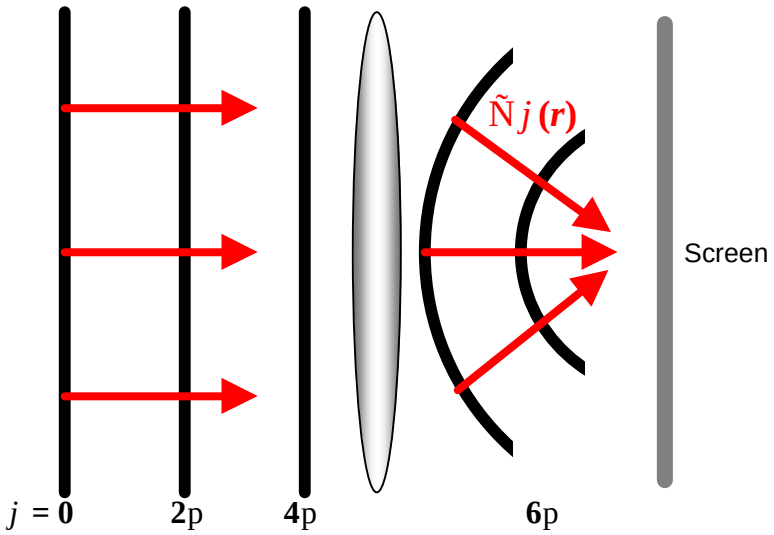

Figure 2.1: The wavefronts (black) coincide with the surfaces of constant phase j (**r**) = 0π, 2π, 4π, and so on, and the local propagation direction is given in free space by the gradient of the phase.

Suppose that the wave propagating direction in an orthogonal coordinate system *xyz* is + *z*. Consequently the wave amplitude concerning the above defined coherent wavefield can be written as $u_z(\mathbf{r}_\perp)=[I_z(\mathbf{r}_\perp)]^{1/2}\exp[i\,j_z(\mathbf{r}_\perp)]$, where $\mathbf{r}_\perp=(x, y)$ is a two-dimensional vector in the transverse direction. Then, as is discussed extensively in [Tea83], the amplitude $u_z(\mathbf{r}_\perp)$ satisfies in paraxial approximation (small angular width of the source as viewed from the observation position) the parabolic equation:

$$\left(i\frac{\partial}{\partial z}+\frac{\nabla_\perp^{\,2}}{2k}+k\right)u_z(\mathbf{r}_\perp)=0 \qquad (2.2)$$

where $\nabla_\perp^{\,2}=\left[(\partial^2/\partial x^2)+(\partial^2/\partial y^2)\right]$ and $k = 2p/l$.

Let (2.2) be multiplied by u_z^* and the complex conjugate of Eq. (2.2) be multiplied by u_z. If the two resulting equations are subtracted, one gets the so-called Transport-of-Intensity Equation (TIE) [Gur95]:

$$\frac{2p}{l}\frac{\partial}{\partial z}I_z(\mathbf{r}_\perp)=-\nabla_\perp.[I_z(\mathbf{r}_\perp)\nabla_\perp j_z(\mathbf{r}_\perp)] \qquad (2.3)$$

which just determines the mechanism of transformation of the phase inhomogeneity to intensity variations.

The expression (2.3) relates the rate of intensity variations in the direction of the beam axis to the intensity and phase in a plane perpendicular to the propagating direction. Thus variations in thickness and refractive index of a sample lead to different phase variations and consequently to a change of intensity with the wave propagation. The connection between the phase and wave intensity can be explained more intuitively as a deformation of the shape of a defined wavefront on passing through the sample due to the obtained phase differences. This wavefront deformation as shown in Fig. 2.1 will cause a redistribution of the wave intensity on a vertical plane at some distance behind the sample. We will try to define the parameters of such a deformation.

The phase difference j, for a ray path through an object relative to vacuum, is given in the classical optics approximation by:

$$j(x,y;z,k) = -k\int_{-\infty}^{z} d(x,y,z';k)dz' \tag{2.4}$$

where the axis of propagation is parallel to z. In this case the phase of the wavefront will be given as $kz\text{-}j$, so that $j < 0$ corresponds to a phase advance. An example for phase changes at the propagation of a coherent wave through a spherical object, Ω, with a refractive index $n = 1 - d_W$ is shown in Fig 2.2 [Wil96].

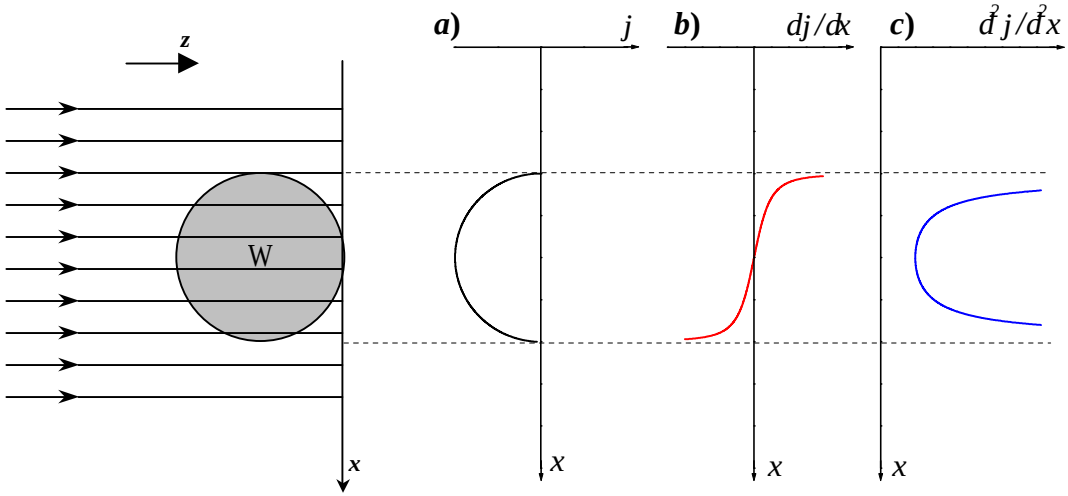

Figure 2.2: Geometrical optics approximation of the propagation of a coherent wave through a spherical object. The phase difference after the transmission j is represented in *a*); the gradient of the phase in a plane transversal to the propagation direction $\partial j/\partial x$ is shown in *b*); the second derivation of the phase $\partial^2 j/\partial^2 x$ is given in *c*).

As seen in Fig. 2.2 the gradient of the phase difference in a plane transversal to the propagation direction behind the object, $\partial j/\partial x$, possesses singularities on the edges of the object. There the refractive index changes from $n_W = 1 - d_W$ to $n_o = 1$ in a very short distance and through equation (2.4) this sharp break is transformed into a very rapid phase change. Taking into account the TIE (2.3), these high values of $\nabla_\perp j_z(\mathbf{r})$ will be visualized in the corresponding areas as strong variations of the intensity in the propagation direction. Let us see how the changes in the intensity look like.

As shown in Fig. 2.1 the local propagation vector $\mathbf{s}(x, y, z)$ is dependent on the gradient of the phase in the direction perpendicular to the local incident vector and can be written in the paraxial approximation as:

$$\mathbf{s}(x, y, z) \approx \left(-\frac{\partial j}{\partial x}, -\frac{\partial j}{\partial y}, k \right) \tag{2.5}$$

so that $\mathbf{s}(x, y, z)$ is normal to the wavefront at the point (x, y, z).

The angular deviation of the normal to the wavefront, Δa, can be expressed as:

$$\Delta a \approx \frac{1}{k} \left| \nabla_\perp j\,(x, y, z) \right| \tag{2.6}$$

and is thus dependent on the variation of the projected refractive index perpendicular to the propagation vector, **k**.

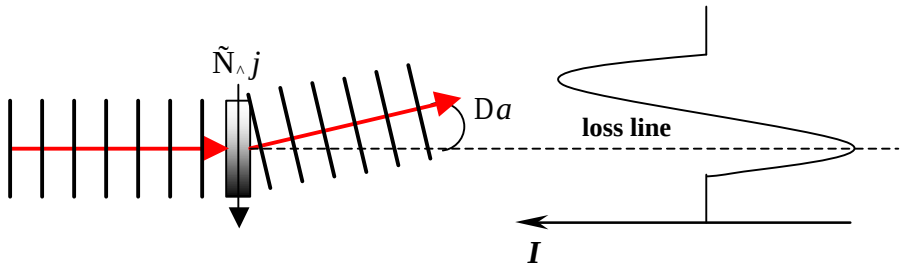

Figure 2.3: An example of deflection of a coherent wave from its propagation direction due to a gradient of the refractive media index in a transversal direction.

This means that the areas which produce a strong phase gradient (the edges in the sample) will deform the wavefront in a way that the rays will be deflected from their original propagation direction and a loss of intensity will be detected in a forward direction (loss line), Fig. 2.3. This diffraction process will cause a considerable edge enhancement in the obtained image.

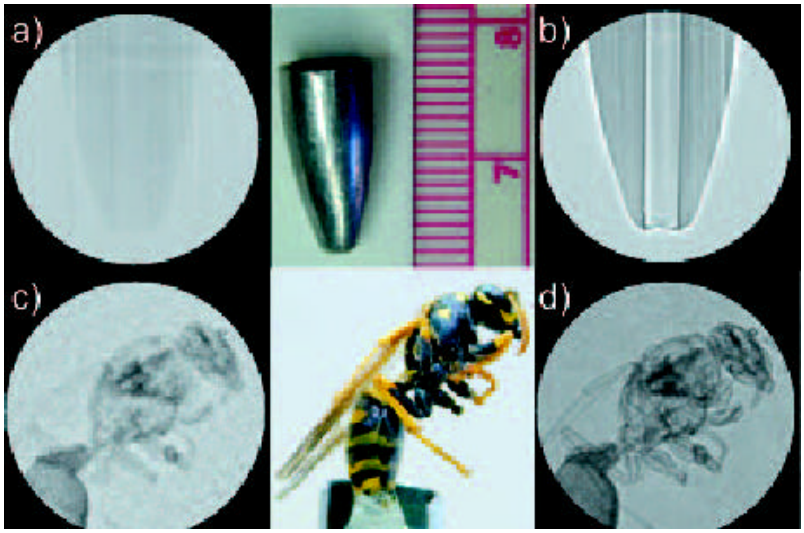

Figure 2.4: Examples of phase contrast imaging with a monochromatized neutron beam with a high spatial coherence. (a) contact and (b) phase contrast images of a lead sinker shown between them. (c) contact and (d) phase contrast images of a wasp [All00].

The edge-enhancement effect can be clearly seen in Fig. 2.4 b and Fig. 2.4 d, where a phase-contrast experiment with monoenergetic neutrons is presented [All00]. The intensity variation on the border of the sample in Fig. 2.4 b is in a good agreement with the simple model shown in Fig. 2.3. The bright halo on the borders of the sample can be related to the deflected rays in direction out of the sample due to the high gradient of the refractive index in these areas, see Fig. 2.3.

Phase contrast with a partially coherent neutron beam

To emit radiation of high coherence, the radiating region of a source must be small in extent (in the limit, a single atom) and the emitted radiation should have a narrow energy bandwidth (in the limit, with $\Delta\lambda$ equal to zero). For real radiation sources, neither of these conditions is achievable. Real radiation sources emit via the uncorrelated action of many atoms, involving different wavelengths. To achieve some degree of coherence two modifications to the emitted radiation can be made. First, a pinhole can be placed in front of the source to limit the spatial extent of the source (spatial coherence). Second, a narrow band-filter can be used to decrease significantly the linewidth $\Delta\lambda$ of the radiation (time coherence). Each modification improves the coherence of the radiation emitted by the source – but only with a drastic loss of intensity.

The phase contrast effect is based on the Transport-of-Intensity-Equation, (2.3), where the phase gradient in a plane transversal to the propagation direction defines intensity variations. Therefore the level of the spatial coherence directly affects the quality of the phase contrast imaging.

The measure for the achieved level of spatial coherence is the transverse coherence length l_t. This represents a distance in a plane transversal to the main propagation direction over which the phases at two points remain correlated. The individual phases may fluctuate, but the two fluctuate together. Because for two points separated by a distance less than or about equal to l_t there is a defined phase relationship.

The definition of the transverse coherence length l_t can be done in terms of the classical optics, as shown below [Ped62].

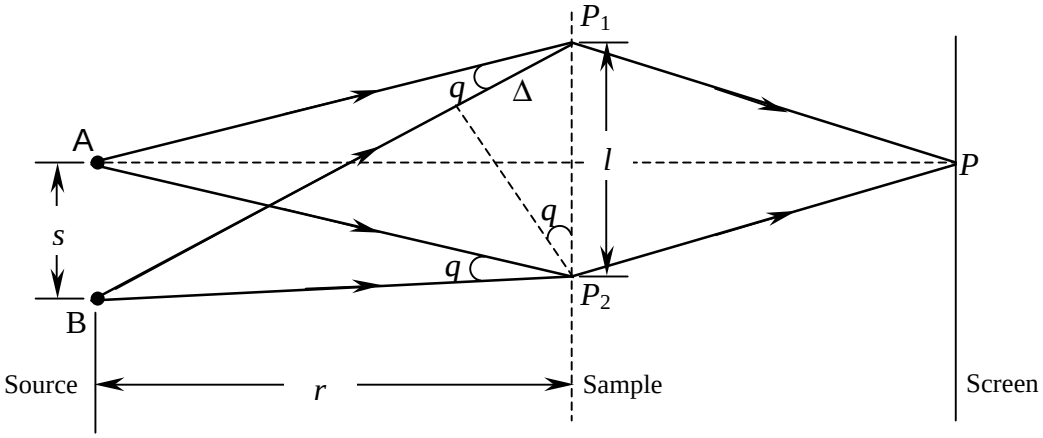

Figure 2.5: Classical optics representation of the definition of transverse coherent length.

Transverse coherence length

Lets us now consider the spatial coherence at points P_1 and P_2 in the radiation field of a quasi-monochromatic extended source, simply represented by two mutually incoherent emitting points A and B at the edges of the source, Fig. 2.5. We may think of P_1 and P_2 as two slits that conduct light to a screen, where interference fringes may be viewed. Each point source, acting alone, then produces a set of double-slit interference fringes on the screen. When both sources act together, however, the fringe systems overlap. If the fringe systems nearly overlap with their maxima and minima coinciding, the resulting fringe pattern is highly visible, and the radiation from the two incoherent sources is considered highly coherent. When the fringe systems are relatively displaced, however, so that the maxima of one fall on the minima of the other, the composite pattern is nearly visible and the radiation is considered incoherent. If we consider the situation shown in Fig. 2.5, points A and P lie on the perpendicular bisector of the two slits, then for the difference of optical paths for sources A and B can be written:

$$AP_2 - AP_1 = 0 \quad \text{and} \quad BP_2 - BP_1 = \Delta$$

For a small angle q the following relations are valid:

$$\Delta \cong lq \quad \text{and} \quad q = s/r$$

where l is the distance between slits and r is the distance to the source.

If $\Delta = \lambda/2$ then the source B gives a minimum in the center of the fringe pattern (point P), while the source A causes a maximum on the same place, so that the composite fringe pattern disappears. In this case it can be written that:

$$\frac{l}{2} = \frac{sl}{r} \text{ or } s = \frac{rl}{2l} \tag{2.7}$$

When the line area from A to B is considered to be a continuous array of point sources, the individual fringe systems do not give complete cancellation until the spatial extent AB of the source reaches twice the value s in Eq. (2.7). If extreme points are separated by an distance $s < rl/l$, then fringe definition is assumed. Regarding this result as describing instead the maximum slit separation l, given a source dimension s, we have for the transversal coherence length:

$$l_t < \frac{rl}{s} \cong \frac{l}{q} \tag{2.8}$$

So to get a wavefield with a high transversal coherence length at the sample position the source size s has to be small and/or the distance between the source and the sample r has to be large.

In case of high transversal spatial coherence all rays emanating from our point source, defined by a small pinhole, are associated with a single set of spherical waves that have the same phase in a surrounding smaller than the coherence length on any given wave front.

A simple representation of a configuration for phase-contrast imaging exploiting a pinhole source to produce a high spatial coherence is shown in Fig. 2.6. The distances r and R are the source-object and object-image distances, respectively. It can be seen also how the spherical wavefront W_1 emanating from the point source s becomes distorted to W_2 on passing through the object.

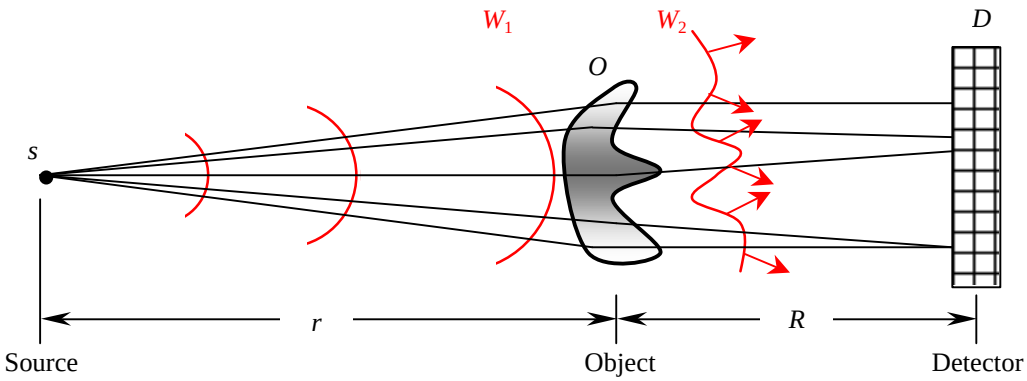

Figure 2.6: A model of a phase-contrast configuration using a pinhole

In case of a neutron beam a refractive index for neutrons can be introduced at their propagation through a defined medium as following:

$$n(x,y,z) = 1 - d(x,y,z) = 1 - \frac{2p}{k^2} a^{coh} r(x,y,z) \qquad (2.9)$$

where a^{coh} and r are the coherent scattering length and the atomic density for the corresponding medium.

The refractive index is very close to unity. For neutrons with a wavelength of 4 Å, it differs from unity by about 10^{-5}.

To show that rapid variations in refractive index ("boundary effect") can lead to strong phase-contrast even with polychromatic radiation, we can consider the example shown in Fig. 2.2 in more detail. The neutron optical path length differences through the sample lead, via equation (2.4), to a phase difference $j(x, y)$ and hence to a phase gradient $\nabla_{\perp} j$ in the direction transverse to the direction of propagation.

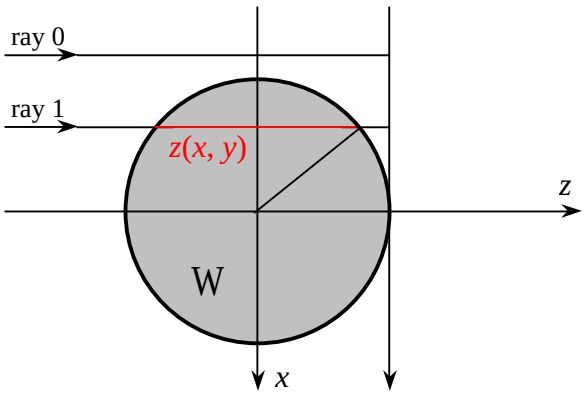

Figure 2.7: A graphical representation of rays passing beside (ray 0) and through (ray 1) a spherical sample.

The phase difference between ray1, which passes through the object Ω parallel to the *z*-axis at constant distance from it, and the reference ray0 is, from equation (2.4), $j(x, y; k) = - kd_W(k)z(x, y)$, where $z(x, y) = 2(r^2 - x^2 - y^2)^{1/2}$ is the length of the intersection of ray 1 with Ω, and *r* is the radius of Ω, Fig. 2.7.

We can then derive from equation (2.6) the angular deviation of rays through Ω to be:

$$\Delta a = \frac{1}{k}\left|\nabla_{\perp} j\right| = 2d_{\Omega}(k)\frac{\sqrt{x^2 + y^2}}{\sqrt{r^2 - x^2 - y^2}} \qquad (2.10)$$

Thus the phase gradient diverges at $x^2 + y^2 = r^2$, where the rays can deviate by large angles from the optical axis even though $d_W(k)$ is small. This can lead to an observable redistribution ("loss") in intensity in the corresponding forward direction, which position is essentially independent of the wavelength. More generally, any rapid variations in refractive index or thickness of a sample may be imaged as sharp losses (variations in intensity) at corresponding points in the image even when a polychromatic source is used, Fig 2.8.

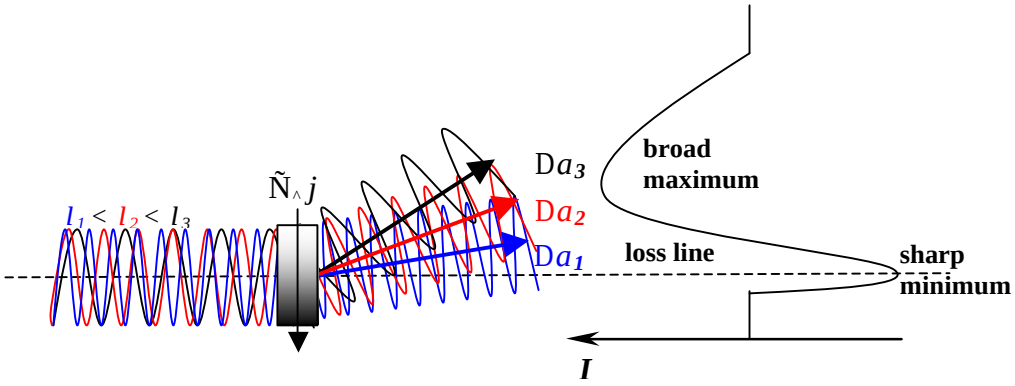

Figure 2.8: Wave deflection caused by a gradient of the refractive index in a perpendicular plane to the propagation direction in case of a polychromatic beam, consisting of a superposition of three waves with wavelengths $l_1 < l_2 < l_3$.

The described phenomenon can be considered also in terms of Fresnel diffraction, where interferential effects will take place on the detector surface due to the superposition of waves transmitted through the sample coming from areas of coherence, defined by the spatial coherent length. The Fresnel diffraction theory [Cow75] will be used in the next paragraph for a more detailed description of the phase contrast effect.

B. Analytical description

For neutrons or other particles, the corresponding wave equation is the *Schroedinger equation* which may be written in its time-independent form as:

$$\left[\nabla^2 + k^2 - \frac{2m}{\hbar^2}V(\mathbf{r})\right]\psi(\mathbf{r}) = 0, \qquad (2.11)$$

where $\psi(\mathbf{r})$ is a wave function such that $|\psi|^2$ represents the probability of a neutron being present in unit volume and $V(\mathbf{r})$ represents the potential function of the external field.

The simple, non-trivial solution of the wave equation, which can be verified by substitution is

$$\psi = \psi_0 \exp\{-i\mathbf{kr}\}, \qquad (2.12)$$

representing a plane wave proceeding in the direction specified by the propagation vector k.

A further solution of importance, corresponding to a spherical wave radiating from a point source, taken to be the origin, is

$$y = y_0 \frac{\exp\{-ikr\}}{r}, \tag{2.13}$$

where $r = |\mathbf{r}|$, since the direction of propagation is always radial $\mathbf{kr} = kr$.

These solutions possess a fundamental property that the sum of them is also a solution. For any number of waves propagating in space, described by their wave functions y_n, this means that the resultant wave function will be represented as $y = S_n y_n$. This property is known as the *Principle of superposition*.

On the principle of superposition is based the *Huygens principle* which describes the wave propagation through space. It states that secondary waves are generated at each point of a wave front so that the sum of these secondary waves defines a new wave-front. In these terms each point on a wave front is considered to be a source of a spherical secondary wave with an initial amplitude proportional to the amplitude of the incident wave. Then the amplitudes of the secondary waves are added to form the amplitude of the resultant wave.

To introduce the disturbance of the object on the amplitude and the phase of the incident wave a simplified case can be considered using a planar, two dimensional object, placed between a point source Q and a plane of observation P, (Fig. 2.9). In this case a transmission function $q(X,Y)$ can be defined which is multiplied by the incident wave function to represent the effect of the object on the incident wave. Then, for a point source of radiation, the wave incident on the object is $\frac{\exp\{-ikr_q\}}{r_q}$, the wave emerging from the object is $q(X,Y)\frac{\exp\{-ikr\}}{r}$ and the wave function $y(x,y)$ at a point of observation is given by the Kirchhoff formula:

$$y(x,y) = \frac{i}{2l}\iint \frac{\exp\{-ikr_q\}}{r_q} q(X,Y) \frac{\exp\{-ikr\}}{r} \{\cos \hat{\mathbf{Zr}} + \cos \hat{\mathbf{Zr}}_q\} dXdY, \tag{2.14}$$

where $\hat{\mathbf{Zr}}$ and $\hat{\mathbf{Zr}}_q$ are the angles between the vectors $\mathbf{r}$ and $\mathbf{r_q}$ and the propagation direction given by the coordinate axis $\mathbf{Z}$.

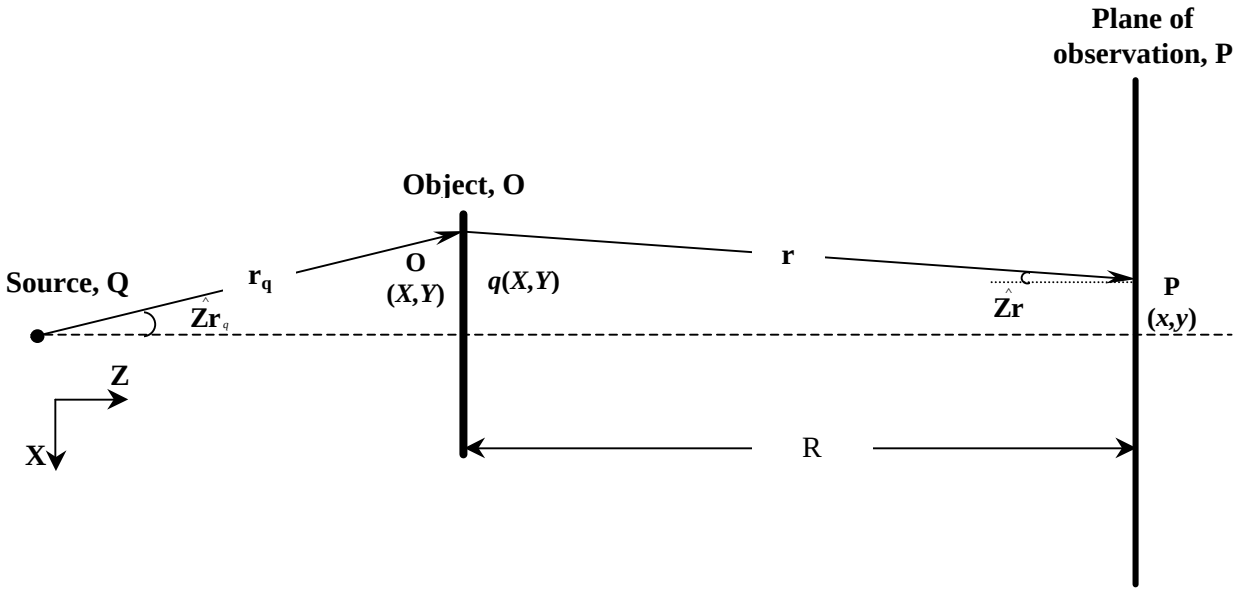

Figure 2.9: Simple representation of the wave propagation through an ideal planar object defined by a transmission function q(X,Y)

From the general Kirchhoff formula (2.14) it is possible to derive a relatively simple form in the particular case of illumination of a two-dimensional object by plane parallel incident waves, known as "Fresnel diffraction". If the object plane is perpendicular to the direction of incidence the incident radiation in (2.14) can be replaced by $y_0 = 1$, which represents a plane wave of unity amplitude having zero phase at $Z = 0$. Then the amplitude on the plane of observation P at a distance R beyond the object is

$$y(x,y) = \frac{i}{2l}\int\int q(X,Y)\frac{\exp\{-ikr\}}{r}\{\cos\hat{\mathbf{Z}}\mathbf{r}+1\}dXdY\,, \qquad (2.15)$$

where for the radius r the following expression can be written

$$r^2 = (x-X)^2 + (y-Y)^2 + R^2$$

so that

$$r = \sqrt{(x-X)^2 + (y-Y)^2 + R^2} \approx R + \frac{(x-X)^2 + (y-Y)^2}{2R} \qquad (2.16)$$

If the wavelength is small compared to the dimensions of the object the angles of deflection of the radiation will be small and a small angle approximation can be assumed, putting $\cos \hat{\mathbf{Zr}} = 1$ and $r = R$ in the denominator of (2.15):

$$y(x,y) = \frac{i \exp\{-ikR\}}{Rl} \int\int q(X,Y) \exp\left\{\frac{-ik[(x-X)^2 + (y-Y)^2]}{2R}\right\} dXdY \qquad (2.17)$$

For the special case that the object has a transmission function $q(X)$, which varies in one dimension only, as in the idealized cases of straight edges, slits and so on, the integral over Y can be carried out to give

$$\int_{-\infty}^{\infty} \exp\left\{\frac{-ik(y-Y)^2}{2R}\right\} dY = \left(\frac{Rl}{i}\right)^{1/2} \qquad (2.18)$$

so that

$$y(x) = \left(\frac{i}{Rl}\right)^{1/2} \exp\{-ikR\} \int_{-\infty}^{\infty} q(X) \exp\left\{\frac{-ik(x-X)^2}{2R}\right\} dX \qquad (2.19)$$

The obtained expression (2.19) is very similar to the definition of one dimensional convolution of two functions $f(x)$ and $g(x)$ which is given by the integral

$$C(x) = f(x) * g(x) = \int_{-\infty}^{\infty} f(X) g(x-X) dX \qquad (2.20)$$

If the following substitution is carried out

$$f(x) = q(x)$$
$$g(x) = \left(\frac{i}{Rl}\right)^{1/2} \exp\{-ikR\} \exp\left\{\frac{-ikx^2}{2R}\right\}$$

then the amplitude distribution on the plane of observation at a distance R from the object can be rewritten in terms of two-functional convolution as

$$y(x) = q(x) * \left[\left(\frac{i}{Rl}\right)^{1/2} \exp\{-ikR\} \exp\left\{\frac{-ikx^2}{2R}\right\}\right] \qquad (2.21)$$

Using the Huygens principle definition the obtained expression (2.21) can be considered as spreading out of the original wave front $q(x)$ by a function which represents the spherical secondary wave $\exp\left\{\frac{-ikx^2}{2R}\right\}$ emitted by a single point on the wave front.

If the object is a pure phase object, i.e. it changes the phase but not the amplitude of the incident wave, the transmission function can be written as

$$q(x) = \exp\{i\,j\,(x)\}, \tag{2.22}$$

where the phase change $j(x)$ depends on the thickness and the refractive index of the material.

Let us consider the amplitude distribution on the plane of observation at a distance R in that case. The wave function on P can be written through (2.21) as

$$y\,(x) = q(x) * \exp\left\{\frac{-ikx^2}{2R}\right\} \tag{2.23}$$

For convenience the convolution operation will be performed in the Fourier space. For this purpose a function $F(u)$ will be defined as

$$q(x) = \exp\{i\,j\,(x)\} \equiv \int \Phi(u) \exp\{-2piux\}du\,, \tag{2.24}$$

where the right side of (2.24) is the Fourier transformation of the transmission function $q(x)$ so that the convolution in (2.23) gives

$$y\,(x) = \int\int \Phi(u) \exp\{-ikX^2/2R\} \exp\{-2piu(x-X)\}dXdu \tag{2.25}$$

Making use of the standard integral

$$\int_{-\infty}^{\infty} \exp\{-a^2x^2\} \cos bx dx = \frac{p^{1/2}}{a} \exp\{-b^2/4a^2\},$$

we obtain

$$y\,(x) = \int \Phi(u) \exp\{-2piux\} \exp\{ipRlu^2\}du \tag{2.26}$$

Then if Rl is sufficiently small we may put

$$\exp\{ipRlu^2\} \approx 1 + iplRu^2 \tag{2.27}$$

and obtain

$$\begin{aligned} y(x) &= \int \Phi(u)\exp\{-2piux\}(1+iplRu^2)du = \\ &= \exp\{ij(x)\} + ipRl\int u^2\Phi(u)\exp\{-2piux\}du \end{aligned} \tag{2.28}$$

Using that the Fourier transform of $\frac{d^n}{dx^n}f(x)$ is $(-2piu)^n F(u)$ the following relation can be written

$$\frac{d^2}{dx^2}[\exp\{ij(x)\}] = \int(-4p^2u^2)\Phi(u)\exp\{-2piux\}du,$$

but the straight-forward differentiation gives

$$\frac{d^2}{dx^2}[\exp\{ij(x)\}] = -\exp\{ij(x)\}[\{j'(x)\}^2 + ij''(x)],$$

so that

$$y(x) = \exp\{ij(x)\}\left[1 + \frac{Rl}{4p}j''(x) + \frac{iRl}{4p}\{j'(x)\}^2\right]. \tag{2.29}$$

Then the intensity distribution on the plane of observation P at a distance R from a one-dimensional phase-object producing a phase change $j(x)$ under plane-wave illumination with wavelength λ will be

$$I(x) = y(x)y^*(x) = 1 + \frac{Rl}{2p}j''(x) \tag{2.30}$$

Of course at the wave propagation through the object volume some absorption and scattering take place so that for enough thin object its transmission function can be represented as a combination of phase and amplitude terms.

$$q(x) = \exp\{ij(x) - m(x)\}, \tag{2.31}$$

where $m(x)$ is the corresponding attenuation coefficient for the defined material. If a plane incident wave falls on this object, the transmitted intensity will be

$$|q(x)|^2 = \exp\{-2m(x)\}, \tag{2.32}$$

so that the effect of the beam attenuation must be added to the phase contrast effect for a complete description of the intensity distribution on the plane of observation.

The obtained expression (2.30) for the intensity distribution due to phase variations induced by the propagation of a coherent radiation through the object was used for simple simulations of phase contrast imaging of simple objects.

Straight edge

For the simulation an iron slab with a thickness d = 3 mm was used. The beam attenuation for a monochromatic neutron beam with a wavelength λ = 2.0 Å was assumed to be exponential $I/I_0 = \exp\{- S_{Fe}\, d\}$ with an attenuation coefficient S_{Fe} = 1.2 cm^{-1}. The ideal step-profile was convoluted with a Gaussian Point Spread Function (FWHM = 150 μm), which represents the response of our detector system and the image blurring due to the beam divergence. The obtained profile is shown in Fig. 2.10 a. The phase variation induced by the iron slab is shown in Fig. 2.10 b. The graph was obtained by a simple application of the formula (2.4) for a coherent scattering length for iron of a_{Fe}^{coh} = 9.45 fm. The refractive index of iron was calculated as

$$d_{Fe} = \frac{2p}{k^2} a_{Fe}^{coh} r_{Fe} = 5.12\text{x}10^{-6},$$

which leads to a phase difference of

$j = -k\int_{-\infty}^{z} d(z')dz = -\frac{2p}{l} d_{Fe} d$ = -153.6 π = - 482.5 rad in relation to vacuum, i.e. a phase advance.

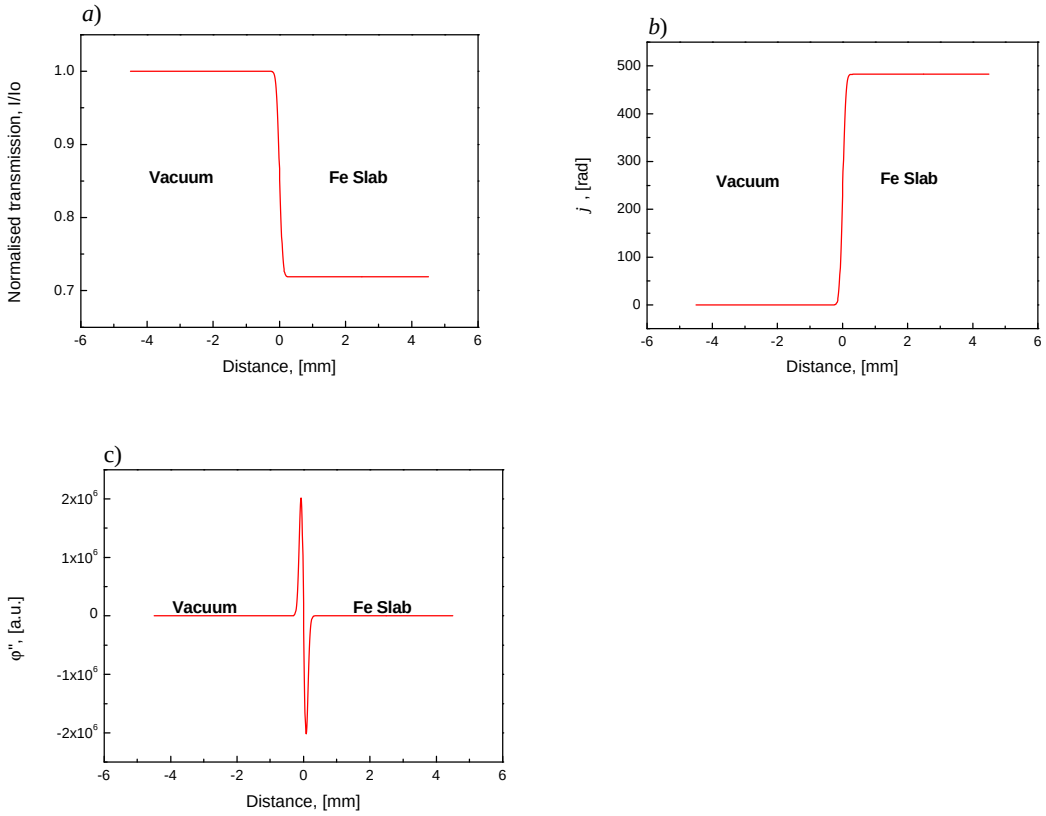

Figure 2.10: A numerical simulation of the neutron transmission through an iron slab (3 mm of thickness) at a beam with high spatial coherence. The attenuation profile is shown in *a)*. The induced phase change in *b)* and the second derivation *j* ''of the phase is presented in *c).*

The second derivation of the phase which is responsible for the phase contrast is shown in Fig. 2.10 c in arbitrary units.

Small capillary

A small Fe capillary was used as an input for the next simulation. The capillary had an outer diameter of 0.8 mm and an inner diameter of 0.6 mm. The performed analysis was analogous to the one shown above. First the attenuation profile was calculated as shown in Fig. 2.11 a. The phase profile and its second derivation are presented correspondingly in Fig. 2.11 b and Fig. 2.11 c.

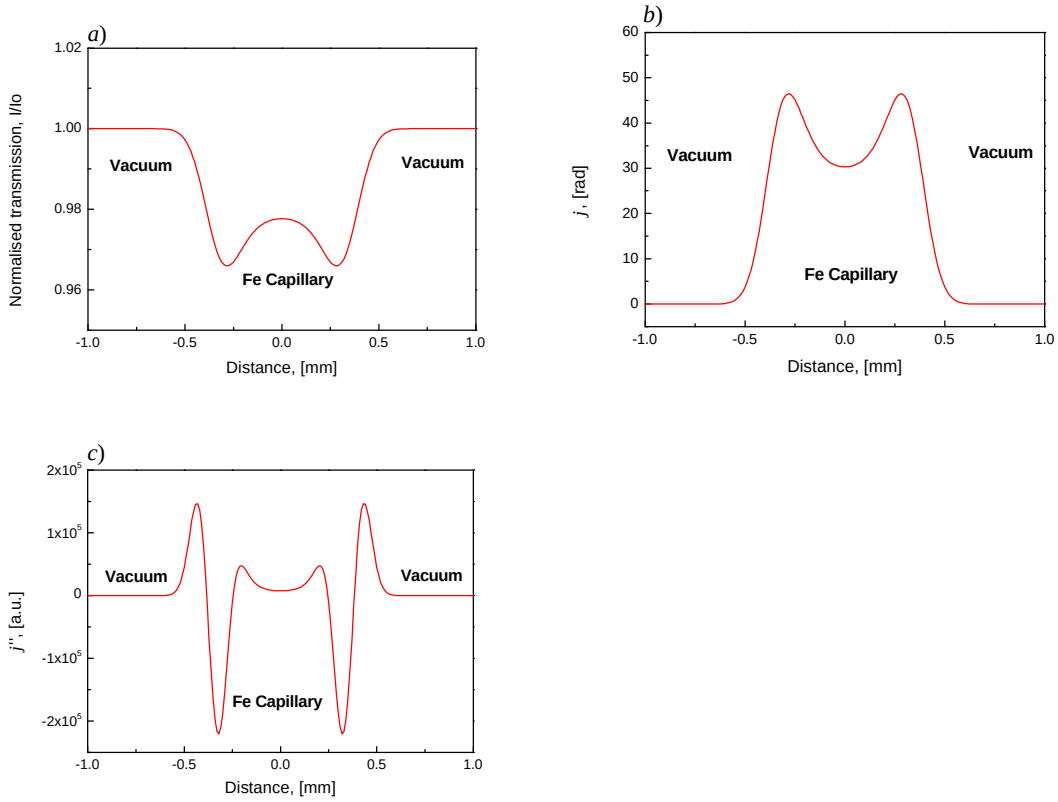

Figure 2.11: A numerical simulation of the neutron transmission through an iron capillary with a 0.8 mm outer and 0.6 mm inner diameter at a beam with high spatial coherence. The attenuation profile is shown in *a)*. The induced phase change in *b)* and the second derivation j'' of the phase is presented in *c).*

Obviously the phase contrast provides different intensity variations than those provided by the beam attenuation.

The used samples for the simulations were not pure phase objects, so that the obtained profiles in a real radiography image under phase contrast conditions would be a superposition of an absorption and a phase contrast contribution. This was proved by a set of experiments presented in the next chapter.

2.3 Experimental setup

Beam characteristics

The experiments were performed at the thermal neutron radiography facility NEUTRA at PSI [Leh99]. A schematic layout of the experimental setup is shown in Fig. 2.12.

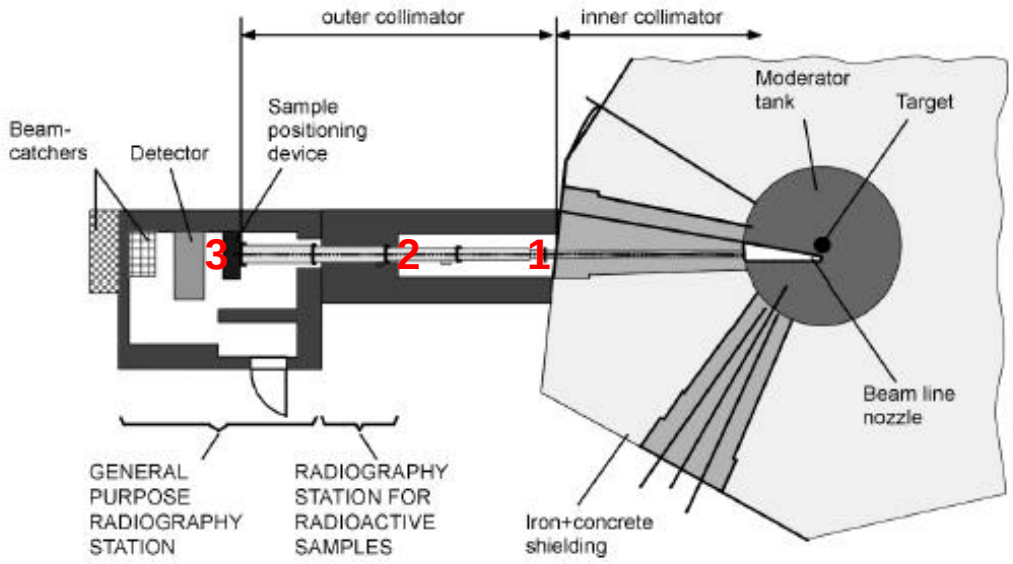

Figure 2.12: A schematic layout of the thermal neutron radiography facility NEUTRA at PSI

The facility is located at a thermal beam port of SINQ and consists of the following elements:

A convergent and a divergent collimator part separated by a Bi-filter where the convergent part limits the view from the collimator towards the neutron source and the Bi-filter reduces the gamma-ray content of the beam. The divergent collimator consists of a divergent channel leading through the bulk shielding around the source and of a divergent evacuated tube, which continues the collimator outside the bulk shielding. Neutrons passing through the filter enter the divergent collimator through an initial circular aperture of 2 cm diameter.

Three irradiation positions are available for radiography purposes, (Fig. 2.12). Since the positions are located at different distances along the beam, the parameters of the beam (flux and collimation ratio) will differ for these positions. Their parameters are shown in Table 2.1.

Table 2.1 :

Irradiation positions	**1**	**2**	**3**
Distance from the pinhole position [mm]	0	3472	6675
Neutron flux [cm^{-2} s^{-1} mA^{-1}]	1.60E+07	5.00E+06	3.00E+06
L/D	200	350	550
Cd-ratio	100	100	100

The neutron spectrum is thermal, mainly given by the moderator (heavy water), the position where the beam tube nozzle looks into the moderator tank and the bismuth crystal in the beam line (for gamma background reduction). The measured spectrum (TOF) is shown in Fig. 2.13.

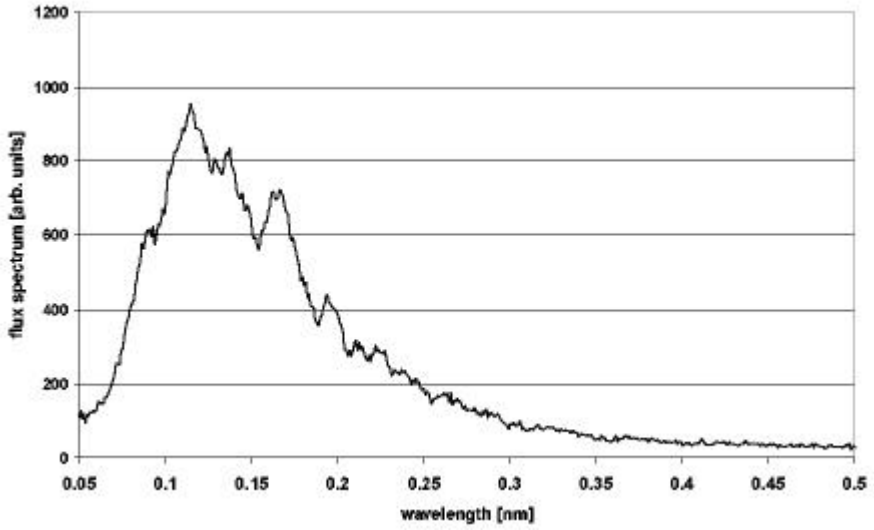

Figure 2.13: The neutron spectrum at NEUTRA

Spatial coherence

In case of a polychromatic neutron beam, the only possibility to achieve a high spatial coherent length defined by eq. (2.7) is to apply some spatial restrictions to the beam. The smaller the size of the source and the larger the source to sample distance, the higher is the achieved spatial coherence length. The change of the source size was performed by a small pinhole drilled in a Gd (macroscopic cross-section for thermal neutrons Σ = 1391 cm^{-1}) foil with a thickness of 100 μm. At that thickness nearly all thermal neutrons (99.99991 %) will be absorbed and the only background at large distance from the pinhole will be the epithermal and fast neutrons transmitted through the foil as well as a small amount of gamma radiation.

For the first experiments a diaphragm with a diameter *s* of 0.5 mm that already existed at PSI was used. The quality of the pinhole can be seen in Fig. 2.14.

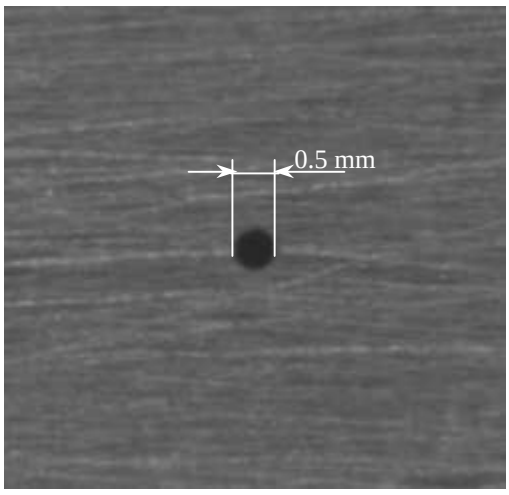

Figure 2.14: Optical microscopy of the used pinhole drilled in a Gd foil

Later pinholes with various diameters were prepared by laser-drilling in the laboratories of the Lehrstuhl für Feingerätebau und Mikrotechnik at TU München.

The maximum possible distance between the pinhole and the sample r was at the irradiation position No. 3 (Fig. 2.12) with approx. 6.5 m, (see Table 1) so for the transverse coherence length given by (2.7) a value of $l_t = r\,l/s$ = 2.5 μm was obtained, where r is the source to sample distance, s is the pinhole diameter and λ = 1.8 Å is the mean wavelength.

Detector system

The requirements for the used detector system were determined by the peculiarities of the experimental conditions.

- First, a high spatial resolution was needed due to the fine effect which we expected to observe. The performed analytical simulations in Fig. 2.10 c and Fig. 2.11 c show that the width of the obtained intensity peaks at the edge positions is in the order of 100 μm, which can be used as a resolution requirement for the detection system.
- Second, a high efficiency and a good signal to noise ratio were needed due to the low beam intensity. The small pinhole considerably reduces the neutron flux, as for a round diaphragm with a diameter of s = 0.05 cm the reduction would be 1600x taking into account that the initial aperture has a diameter of 2 cm as mentioned above. Without the diaphragm the neutron flux at the irradiation position No. 3 is $3x10^6$ n/cm^{2}s, so that using the small pinhole the available neutron flux for phase contrast experiments will be $1.9x10^3$ n/cm^{2}s.
- Third, the detector should have a very low constant background noise (dark current). The strong neutron flux reduction will of course increase the exposure times and consequently the noise level integrated during this time.

Considering all the mentioned requirements to our detection system we chose the Imaging Plate to be appropriate using it for this kind of measurements. The plates which we had at our disposal were produced especially for neutron imaging – Fuji IP-ND. Their best spatial resolution is in the range of 100 μm. They possess very high neutron efficiency due to the used Gd_2O_3 powder as converter material and negligible dark current because of the lack of any electronic noise during the exposure.

2.4 Experiment

All the experiments were performed at the thermal neutron radiography station NEUTRA at PSI using the whole thermal spectrum of the beam, (Fig. 2.13). The experiment geometry was configured as described above: a round diaphragm with a

diameter of 0.5 mm in the beginning of the beam, a diaphragm to sample position distance of 6.5 m and the sample to detector distance was set to be variable.

First the beam profile without sample was taken at an exposure time of 180 min as shown in Fig. 2.15. It can be seen that the profile was almost flat. This fact was used to perform a qualitative analysis without image normalization. The signal to noise ratio was calculated as a ratio of the beam level to the background level obtained from the profile – signal/noise = 240/75 = 3.2.

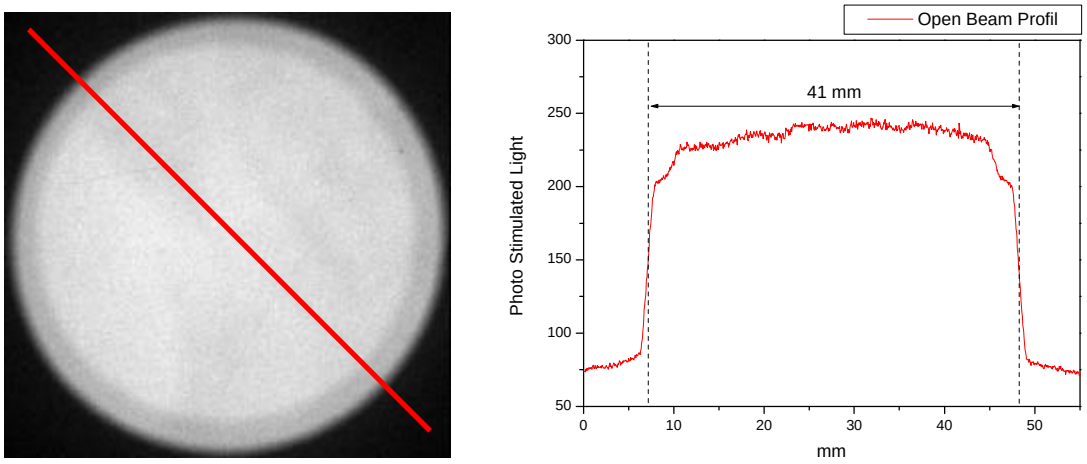

Figure 2.15: Image of the neutron beam without sample at the following parameters:
Distance pinhole to sample: 7.5 cm
Pinhole diameter: 0.05 cm
Exposure time: 180 min
The intensity profile taken through the beam is shown on the right-hand side.

The diameter of the obtained round spot *S* was measured to be 41 mm. This parameter defines exactly the beam collimation ratio L/D at the diaphragm position as shown in Fig 2.16 .

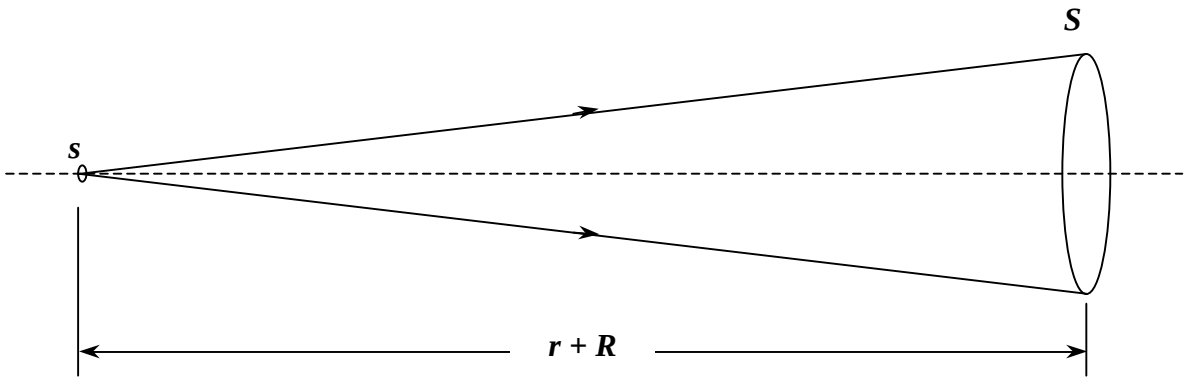

Figure 2.16: The beam divergence produced by a round diaphragm with diameter *s* at a distance *r* + *R*.

If we assume the small pinhole with a diameter s = 0.5 mm as a point source in comparison to the source to detector distance of $r + R$ = 7.5 m then for the L/D ratio will be valid: L/D = $(r + R)/S$ = 183, where S = 41 mm is the diameter of the measured open beam spot, (Fig. 2.16). This result correlates very well with the value 200 given in Table 2.1 for the L/D ratio at the irradiation position No. 1, where the diaphragm was placed.

Our further tasks were to observe edge-enhancement effects in neutron radiography images with the so defined geometry and to explain the observed effects in terms of phase contrast imaging. For that purpose we change the main parameters of the beam geometry – sample to detector and diaphragm to sample distances as well as the diameter of the pinhole.

Basic experiment

To prove that phase contrast imaging is possible with the so arranged setup, one basic experiment was performed in the beginning. The idea was to check the validity of formula (2.30) in general.

Most materials possess a positive coherent scattering length a^{coh} and thus by (2.4) they induce a negative phase difference j by propagation of coherent neutron waves through them, which corresponds to a phase advance.

There are few materials, which are characterized by a negative a^{coh}, e.g. Ti and V. Consequently the phase difference for them will be positive, which corresponds to a phase delay.

If two materials with coherent scattering lengths of equal absolute value, but opposite signs are taken (e.g. Ti with a_{Ti}^{coh} = -3.4 fm and Al with a_{Al}^{coh} = 3.5 fm) then their phase profiles should behave opposite. The second derivations of the phase change in case of Ti and Al plates with a constant thickness will give consequently an opposite intensity variation at the edge positions. For the Al plate the intensity maximum should be obtained outside the sample area while for the Ti plate the maximum should be inside the sample area or in other words, if we use the intuitive model, the neutrons will be deflected outwards of the sample at a positive phase variation (Al) and inwards to the sample by a negative phase variation (Ti).

The experiment was performed with two plates of Ti (3 mm thickness) and Al (5 mm thickness) imaged together at the phase contrast arrangement described above at a distance of 100 cm from the detector for an exposure time of 120 min. The plate thicknesses were chosen in the way that the module of the calculated phase difference to be the same for the two materials, which means that $|d_{Al} d_{Al}| = |d_{Ti} d_{Ti}|$ (see eq. 2.4). Taking into account the expression for $d = \frac{2p}{k^2} a^{coh} r$ (see eq. 2.9) we will obtain the following relation for the thicknesses: $\frac{d_{Al}}{d_{Ti}} = \frac{|d_{Ti}|}{|d_{Al}|} = \frac{|a_{Ti}^{coh} r_{Ti}|}{|a_{Al}^{coh} r_{Al}|} = \frac{3.4x4.5}{3.5x2.7} \approx \frac{5}{3}$, where r_{Al} and r_{Ti} are the densities for aluminum and titanium correspondingly.

The obtained experimental profiles are presented in Fig. 2.17. The position of the edges of the plates is marked as a zero position in the plots.

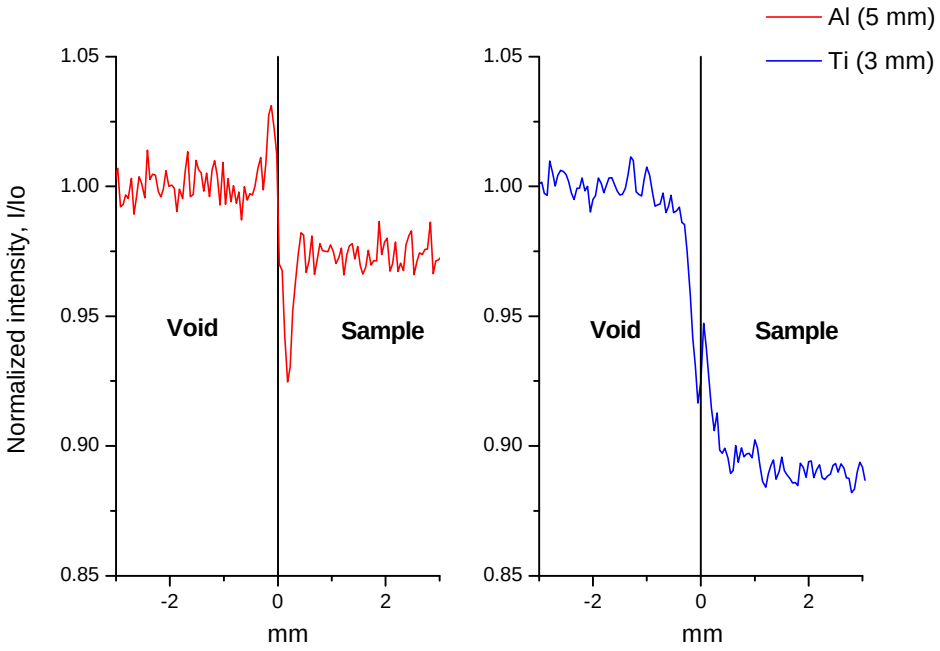

Figure 2.17: Experimental edge profiles for Al and Ti plates measured under phase contrast conditions.

The good agreement with the theoretical prediction given above can be clearly seen, which proves qualitatively the validity of expression (2.30) in case of phase contrast imaging.

Variation of the sample to detector distance

The obtained expression (2.30) shows that the phase contrast varies linearly with the sample to detector distance. This relation was checked by a set of experiments where the sample was positioned at an irradiation position No. 3 and radiography images at different sample to detector distances were taken. As a test object stainless steel capillaries (syringe needles) with different diameters – 0.3, 0.5, 0.6, 0.8 and 0.9 mm were used. The obtained images are shown in Fig. 2.18.

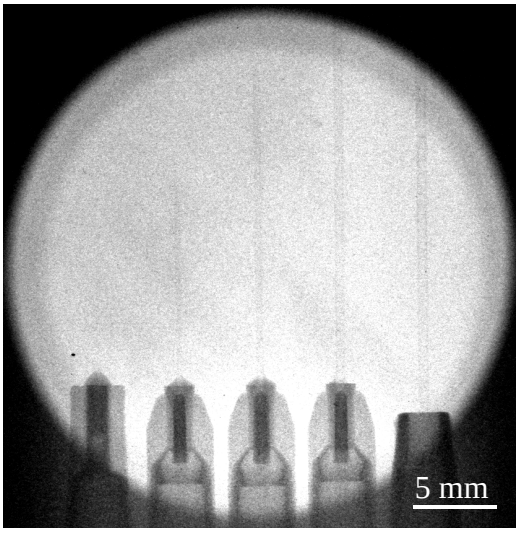

Distance sample to detector: 0 cm
Distance pinhole to sample: 650 cm
Pinhole diameter: 0.5 mm
Exposure time: 180 min

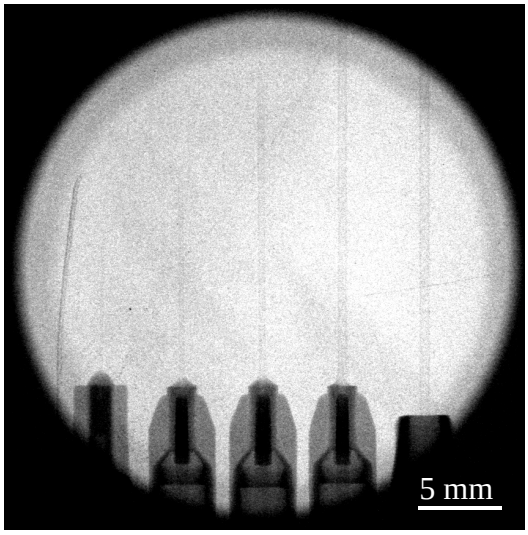

Distance sample to detector: 5 cm
Distance pinhole to sample: 650 cm
Pinhole diameter: 0.5 mm
Exposure time: 180 min

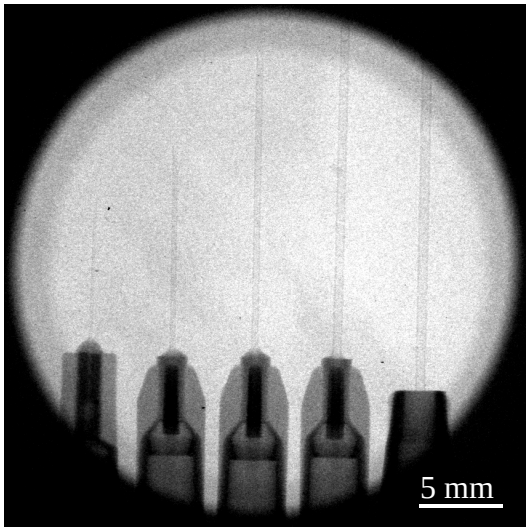

Distance sample to detector: 15 cm
Distance pinhole to sample: 650 cm
Pinhole diameter: 0.5 mm
Exposure time: 180 min

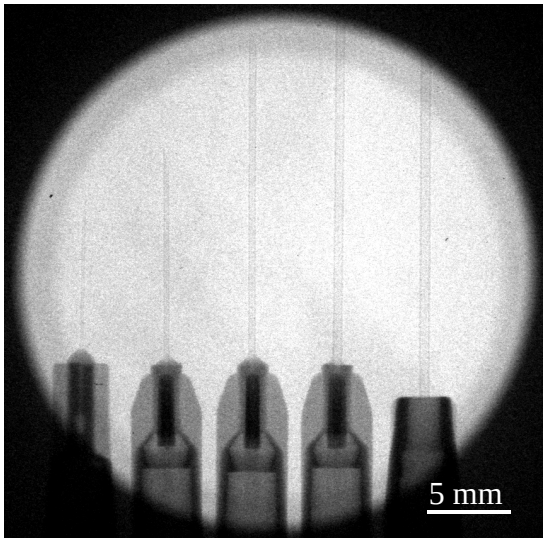

Distance sample to detector: 25 cm
Distance pinhole to sample: 650 cm
Pinhole diameter: 0.5 mm
Exposure time: 180 min

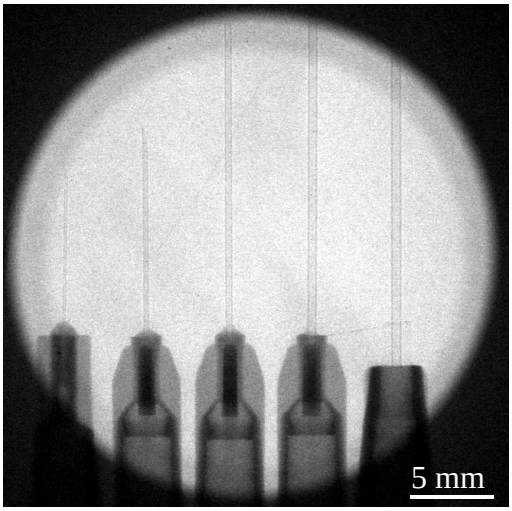

Distance sample to detector: 50 cm
Distance pinhole to sample: 650 cm
Pinhole diameter: 0.5 mm
Exposure time: 180 min

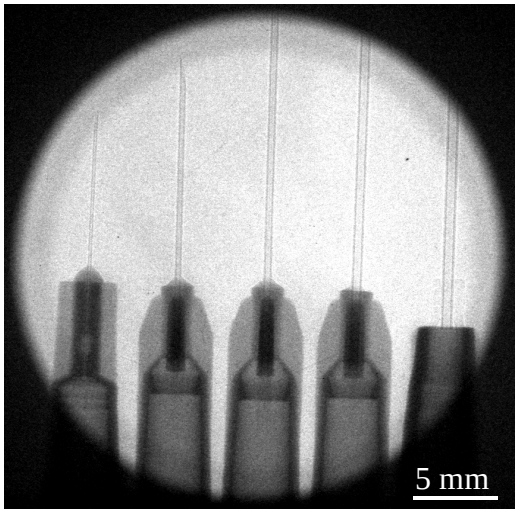

Distance sample to detector: 100 cm
Distance pinhole to sample: 650 cm
Pinhole diameter: 0.5 mm
Exposure time: 180 min

Figure 2.18: Phase contrast images of a set of stainless steel capillaries (syringe needles) with diameters – 0.3, 0.5, 0.6, 0.8 and 0.9 mm at different distances to the detector.

After the qualitative analysis of the obtained radiography images it can be concluded that increasing the distance between the sample and the detector, the images become sharper and sharper. For instance in the last radiograph taken at a 100 cm distance from the detector, one can see even the channel of the smaller capillary with a diameter of 0.3 mm. This means that the achieved resolution is smaller than the half of the needle's diameter i.e. smaller than 150 μm. Unfortunately the setup equipment does not allow to set sample to detector distances between 120 cm and 400 cm due to the flight-tube construction at NEUTRA. This was the reason to limit our investigations in the distance interval from 0 cm to 100 cm. To obtain some quantitative picture of the observed phenomena, horizontal image profiles through the capillaries were taken by plotting of the values of the pixel brightness with the distance. The profiles for all the images, shown in Fig. 2.18, are presented together in Fig. 2.19.

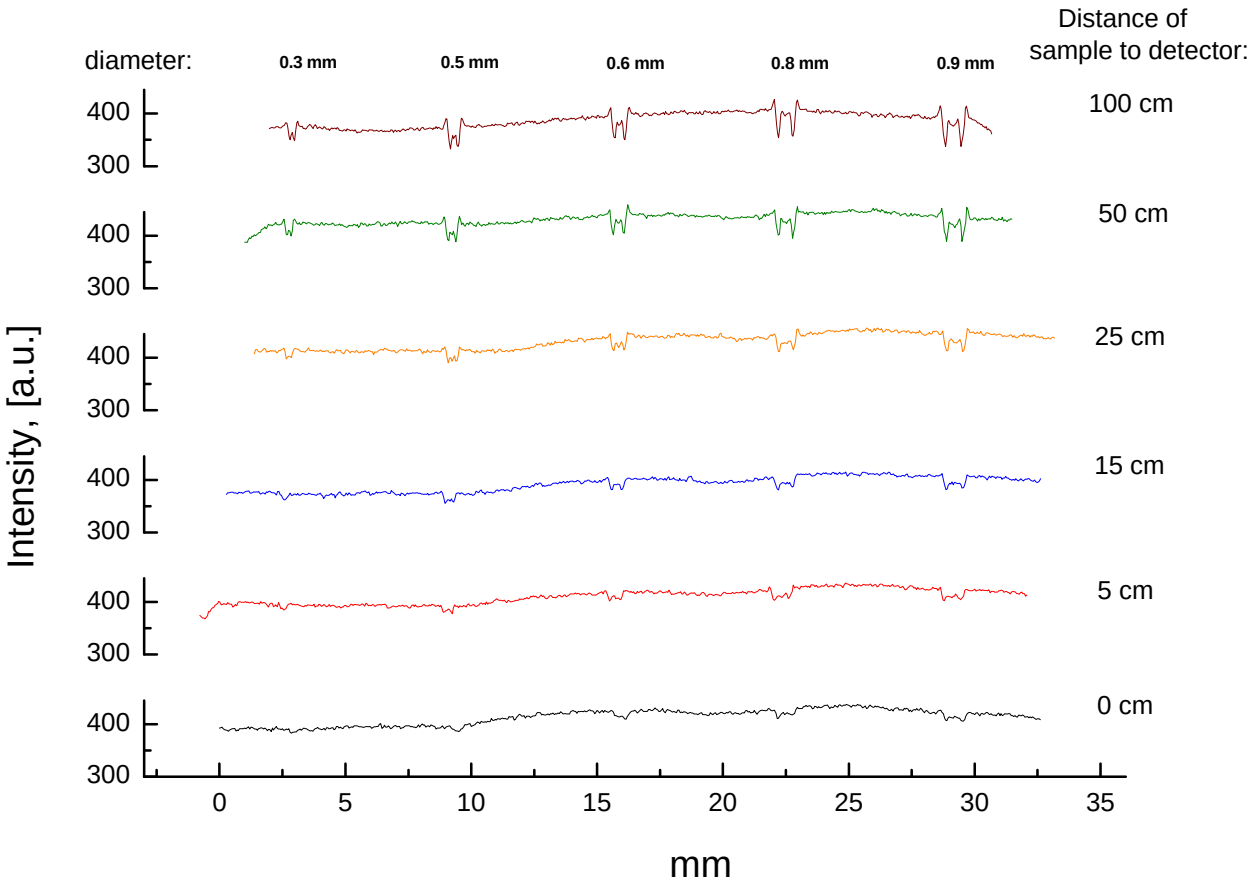

Figure 2.19: Horizontal profiles through the capillaries at different distances to the detector.

One can see that the edge-enhancement on the capillary borders at larger distances to the detector in the presented profiles, Fig. 2.19, follows the behavior shown in Fig. 2.8 – a consequence of minimum and maximum of the intensity at rapid variations of the refractive index.

A conventional thermal neutron radiography is shown in Fig. 2.20 The comparison between the normalized intensity profiles through the capillaries investigated by the conventional and the phase contrast (a sample to detector distance of 100 cm) radiography techniques is presented in Fig. 2.21.

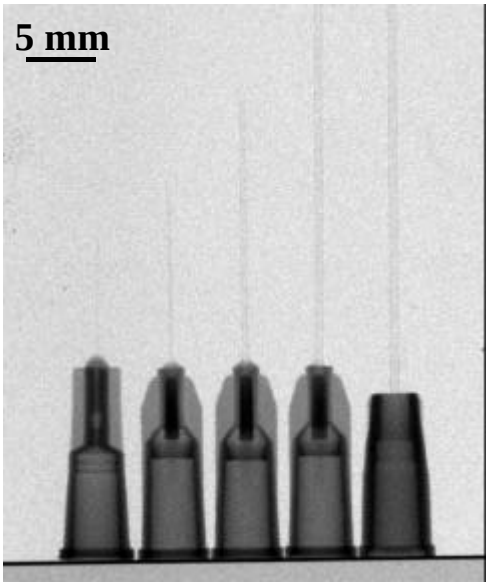

Figure 2.20: Conventional radiography of the test sample performed at the thermal neutron radiography station NEUTRA under the following conditions:
Used detector: Imaging Plate Fuji IP-ND
Measuring time: 15 s
Distance sample-detector: 10 cm

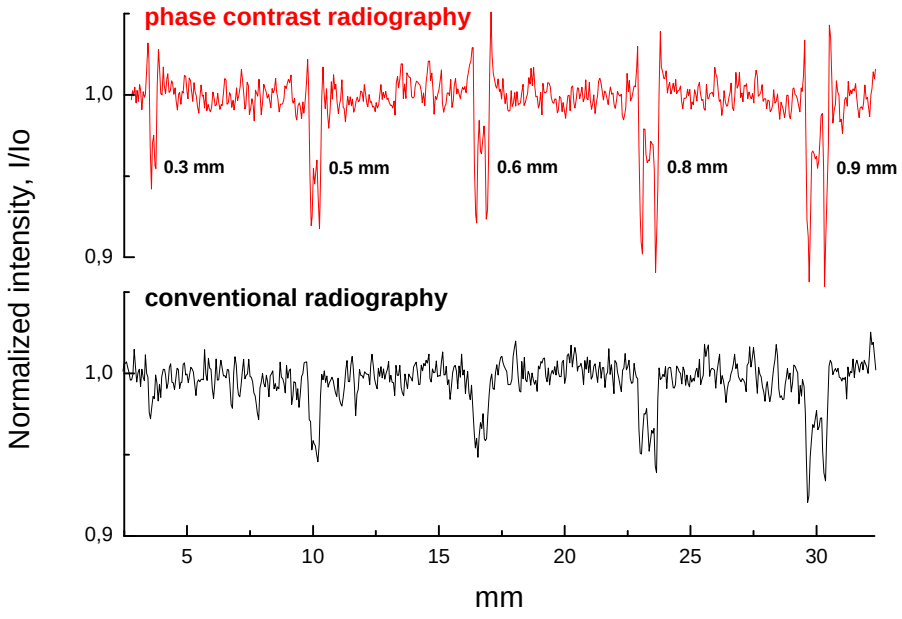

Figure 2.21: Intensity profiles taken through the needle edges for two kinds of radiography imaging: phase contrast radiography at a sample to detector distance of 1 m and conventional thermal radiography at a distance of 10 cm from the detector.

Obviously the edge-enhancement of the needle borders presented in case of phase contrast radiography is missing in the conventional radiography profile. Furthermore the

smallest capillary of 0.3 mm can not be recognized with the conventional method while the phase contrast technique makes possible to resolve even the capillary channel.

Increasing the distance between the sample and the detector even more, the contrast rises, but the image blurring due to the beam divergence also increases. A small pinhole together with a large distance to the sample determines a very parallel beam at the sample position with a L/D ratio of 13000 [Appendix A] for the setup parameters presented above. In spite of this the image blurring can be seen at large sample to detector distances. For example at a 1 m sample to detector distance the imaging blurring due to the beam divergence will be 80 μm, which is in the order of the detector resolution of approximately 100 μm. At a distance of 4 m the image blurring will increase four times, which means that every sample point will be projected on a spot with a size of 320 μm. In this case the blurring effect will dominate over the phase contrast and the obtained images will be smoothed in comparison to the images taken at smaller distances to the detector. In Fig. 2.22 two phase contrast images of a biological object (dried hornet) obtained at approx. 0.45 m and 4 m from the detector are presented.

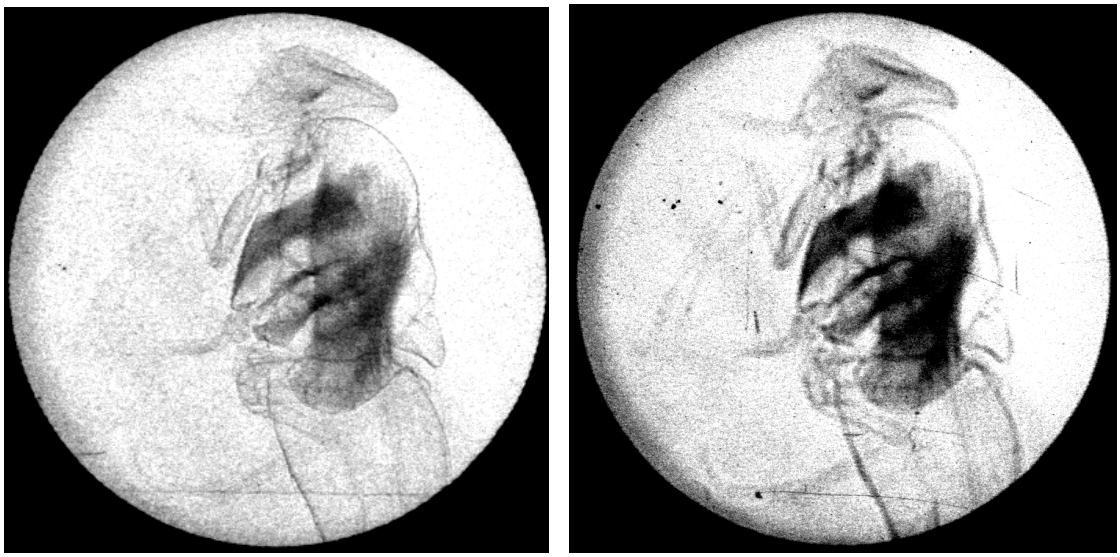

Distance pinhole-object ~4 m
Distance object-detector ~0.45 m
Exposure time 240 min

Distance pinhole-object ~4 m
Distance object-detector 4 m
Exposure time 60 min

Figure 2.22: Phase contrast images of a dried hornet taken at two different distances between the sample and the detector of 0.45 m (left) and of approx. 4 m (right).

The blurring in the far-away image is clearly visible. Thus a criterion for the maximum sample to detector distance can be defined, where the image blurring due to the beam divergence $d = l/(L/D)$ [Appendix A], where l is the sample to detector distance, should be smaller than the given detector resolution C or $l/(L/D) < C$. For imaging plates the specified resolution is in the order of $C \sim 100$ μm, so that at the above described setup

phase contrast experiments can be performed at sample to detector distances of $l < (L/D)C = (13000)\text{x}10^{-4}$ m = 1.3 m.

Dependence on the chromatic coherence

Following the image contrast description by formula (2.30) the next conclusions can be made:

- The structure of the image is λ-independent
- For a polychromatic source one can simply replace λ in the formula (2.30) by a spectral weighted sum.

To prove these conclusions the following procedure was performed. For one defined capillary with a diameter of 0.8 mm the phase contrast profile obtained at a distance 1 m from the detector was subtracted from the conventional radiography profile defined only by the absorption in the sample, (Fig 2.23). In this way the contribution only due to the phase contrast was separated for the used polychromatic (thermal) neutron spectrum. The obtained profile was compared in Fig. 2.24 with a phase contrast simulation for the same capillary by using a monochromatic neutron radiation with a wavelength of 2 Å (Fig. 2.11). The simulated profile was rescaled by a simple multiplication by a constant.

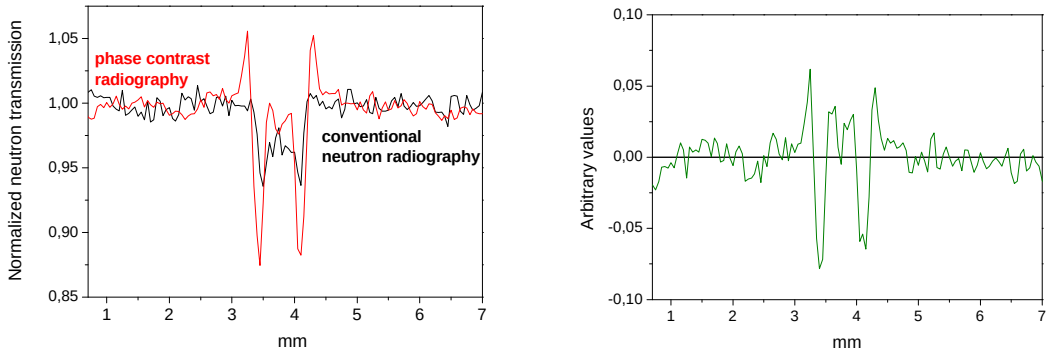

Figure 2.23: The horizontal profiles through the needle with a diameter of 0.8 mm in case of phase contrast imaging and conventional neutron radiography (left). The contribution only due to the phase contrast effect was obtained after the subtraction of the two profiles (right).

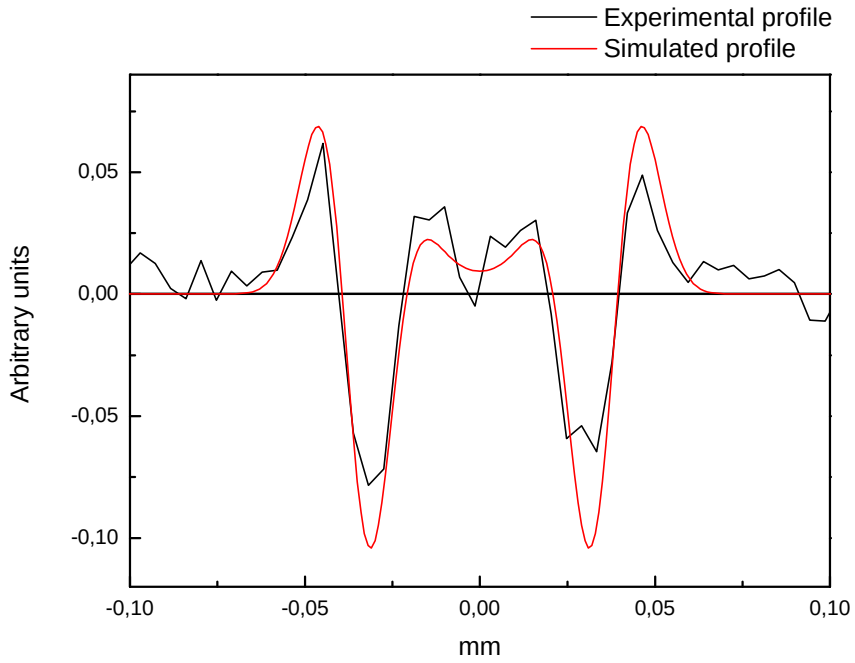

Figure 2.24: Comparison between experimental profile of a steel capillary (0.8 mm) obtained with a polychromatic (thermal) beam and a simulated profile where a monochromatic radiation (λ = 2 Å) was used.

From the comparison it can be seen that despite the different spectral distributions the agreement between the two profiles is very good. This proves the conclusion mentioned above that the neutron spectrum is not important for the phase contrast effect.

Dependence on the spatial coherence length

Pinholes with different openings were used to investigate the influence of various spatial coherence lengths on the image quality. The diaphragms were prepared by laser drilling in 100 μm Gd foil. The used openings were with diameters of 400 and 100 μm. The images obtained with these pinholes are shown in Fig. 2.25. A large sample to detector distance of 3.25 m was used in order to increase the contrast effect, of course, with some loss of spatial resolution.

The presented images show an increase of the blurring with a decrease of the pinhole aperture. A possible reason for the observed behavior could be the bad signal/noise ratio at small apertures (Fig. 2.26). In these cases the transmitted neutron flux through the diaphragm is comparable with the background level, so that the obtained image is blurred by the radiation transmitted through the Gd foil.

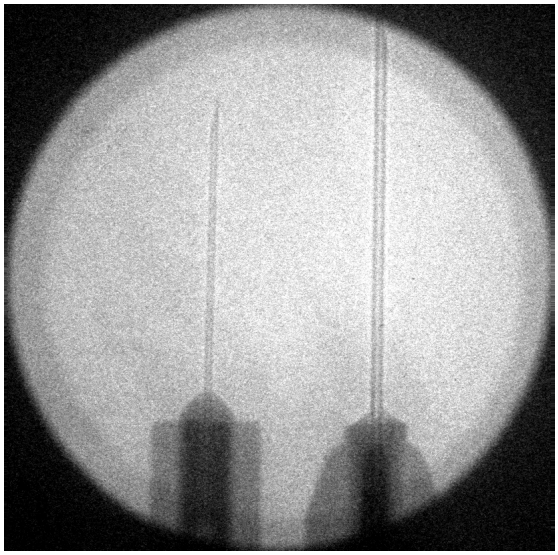

Distance sample to detector: 325 cm
Distance pinhole to sample: 325 cm
Pinhole diameter: 0.4 mm
Exposure time: 2 h

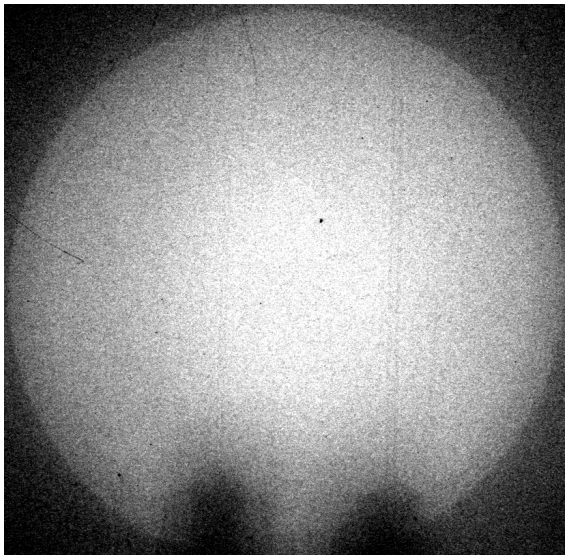

Distance sample to detector: 325 cm
Distance pinhole to sample: 325 cm
Pinhole diameter: 0.1 mm
Exposure time: 14 h

Figure 2.25: Phase contrast images of two steel capillaries of 0.3 mm and 0.5 mm at different pinhole apertures of 0.4 mm (left) and of 0.1 mm (right).

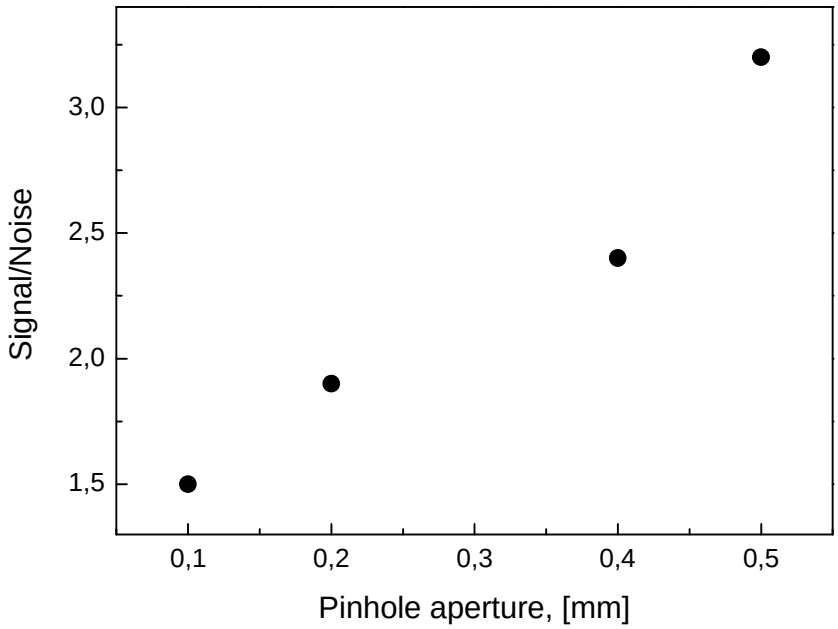

Figure 2.26: Signal to noise ratios for different pinhole apertures calculated as a ratio of the beam level to the background level obtained from the image intensity profiles (see Fig. 2.15).

2.5 Applications

The phase contrast imaging method was tested on a pure phase object for neutrons: aluminum foam. Aluminum is almost transparent for neutrons and if we want to obtain some contrast about the internal structure of the foam, the conventional thermal radiography will provide unsatisfactory results, (Fig. 2.27 left). Instead of that the phase contrast radiography gives very sharp contrast for the boundaries of the bubbles fixed in the foam volume during its production, (Fig. 2.27 right).

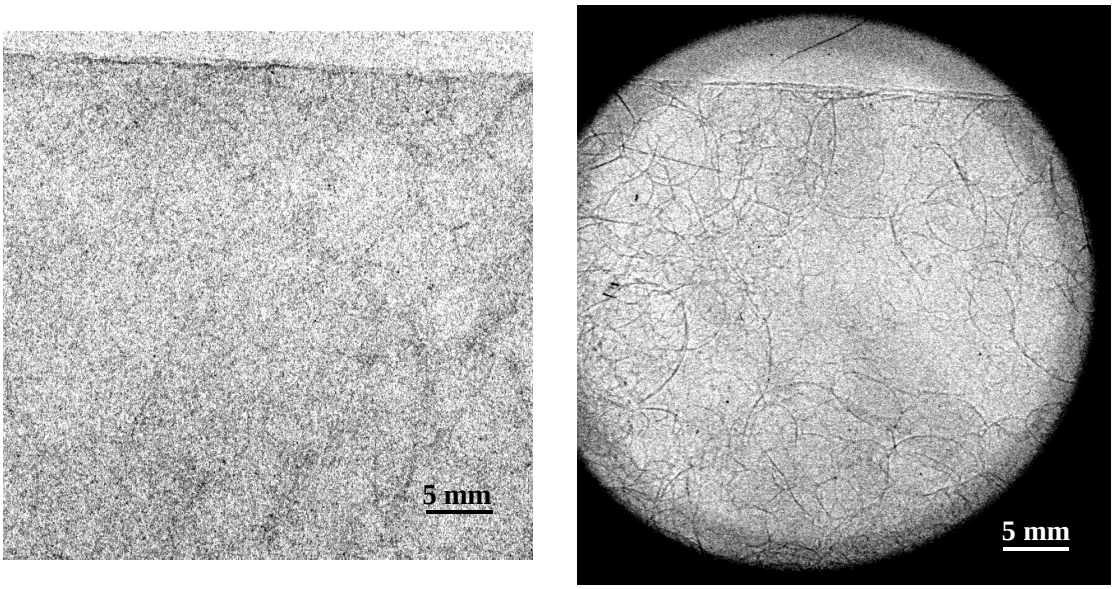

Figure 2.27: Conventional thermal neutron radiography at a distance 10 cm from the detector and 15 s exposure time (left) and phase-contrast neutron radiography of a piece of aluminum foam. The phase contrast experiment was performed at: 120 cm sample to detector distance; source-object distance: 7m; pin hole: 0.5 mm; exposure time: 120 min.

In that way useful information about the form and the size of the foam bubbles can be obtained. For example the thickness of the bubble walls was measured in the order of 0.3 mm.

The advantage of neutrons is that they easily penetrate heavy elements which are usually strong absorbers for X-rays. The next example shows a phase contrast investigation of a non pure phase object: a lead foam with a thickness of 0.5 cm. At this thickness for X-rays with an energy of 100 keV (att. coeff. of 62.98 cm^{-1} for Pb) the corresponding absorption will be approx. 100 % while for thermal neutrons it is only 38 % (att. coeff. of 0.96 cm^{-1}). Therefore the investigation of such materials can be performed only with neutrons or high energy gamma rays. The phase contrast imaging with a high-energy radiation has the serious drawback that the refractive index for the materials becomes so small that the deflection of the rays at the sample edges is negligible. This fact requires very large distances between the sample and the detector which is a non-trivial problem. Therefore the neutron phase contrast radiography appears to be the only method which can be applied in such cases, (Fig. 2.28).

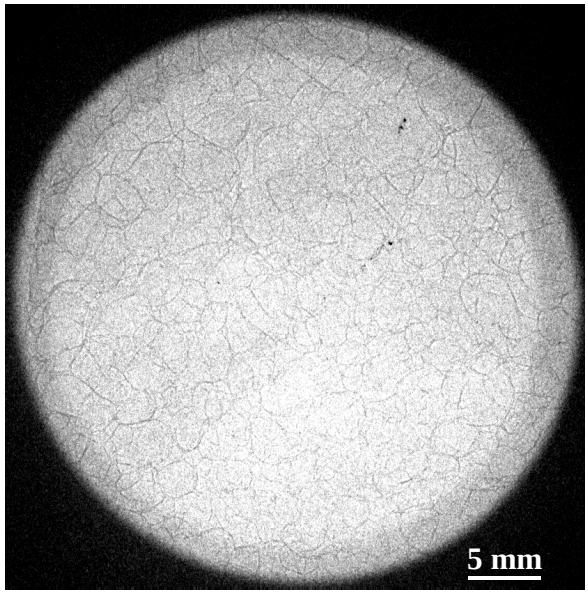

Figure 2.28: Phase-contrast neutron radiography of a piece of lead foam with a thickness of 0.5 cm. The experiment was performed at: 120 cm sample to detector distance; source-object distance: 7m; pinhole: 0.5 mm; exposure time: 120 min.

The obtained image (Fig. 2.28) clearly shows the borders of the separate bubbles (estimated to be in the order of 0.2 mm) which was impossible with the conventional neutron radiography imaging where the picture was similar to the one shown in Fig. 2.27 (left).

The phase-contrast imaging with thermal neutrons was tested also by non-destructive investigation of standard technical parts – a cogwheel, driven by a small cylindrical shaft. The comparison between conventional thermal and phase-contrast radiographies is shown in Fig. 2.29.

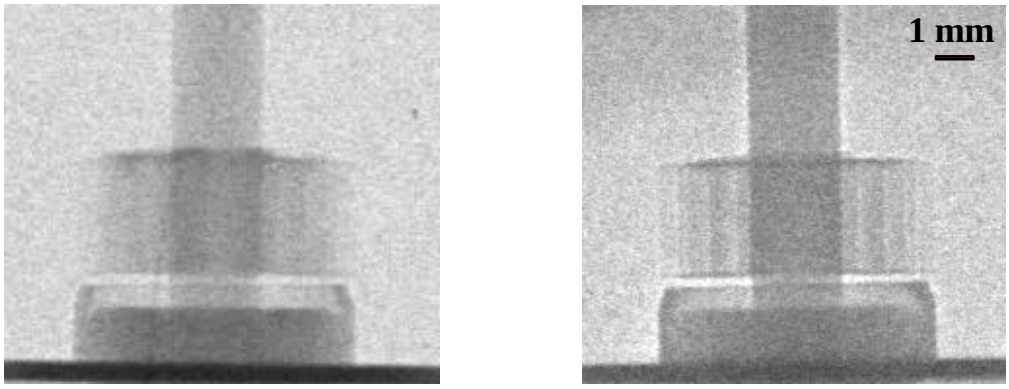

Figure 2.29: Conventional thermal radiography of a cogwheel (left) and a phase-contrast radiography taken at 120 cm sample to detector distance; source-object distance: 7m; pinhole: 0.5 mm; exposure time: 90 min.

The improved contrast in case of phase-contrast radiography can be seen easily in Fig. 2.29 (right). The observed edge-enhancement fits well with the expected consequence of maxima and minima in the image brightness around the sample edges.

This gives the possibility to recognize the cog borders and to perform measurements of the cogwheel with a high precision.

To test this option the diameters of the steel capillaries, shown in Fig. 2.18, were measured from their phase contrast profiles (Fig. 2.21). At the calculations the effect of the object magnification due to the sample to detector distance was taken into account also as for the mentioned above beam parameters the magnification ratio was estimated to be 1.16x. The obtained values were compared with the tabulated values for the needles in Table 2.2.

Table 2.2:

Tabulated value, [mm]	0.300	0.500	0.600	0.800	0.900
Measured value, [mm]	0.337	0.514	0.633	0.805	0.898
Relative error, $\Delta x/x$	12 %	3%	6%	0.6%	0.2%

The results in Table 2.2 show that even for distances below 0.5 mm measurements with a good resolution can be performed. To meet the limits of this feature two metal meshes were investigated by phase contrast radiography (Fig. 2.30). The finer mesh consisted of brass wires with a diameter of 0.17 mm and a distance of 0.25 mm between them, while for the steel coarser mesh these parameters were 0.25 mm (wire diameter) and 0.63 mm (distance between the wires) correspondingly.

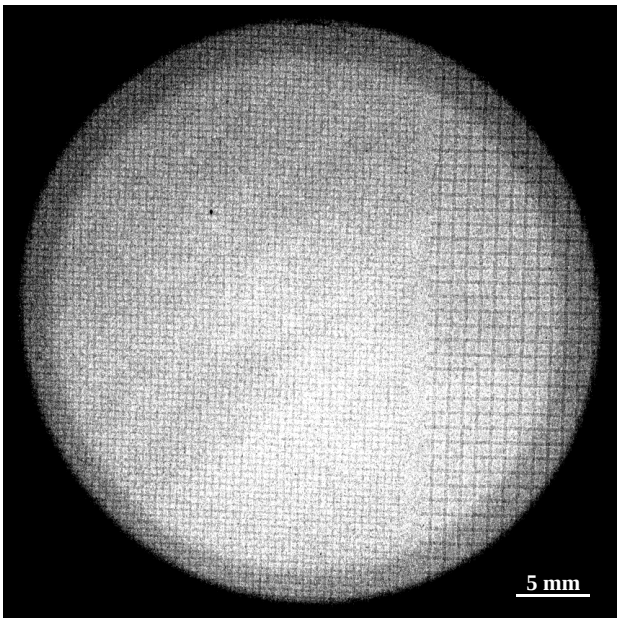

Figure 2.30: Phase-contrast neutron radiography of two meshes. The experiment was performed at: 120 cm sample to detector distance; source-object distance: 7m; pinhole: 0.5 mm; exposure time: 120 min.

The intensity profiles through the meshes are shown in Fig. 2.31.

The phase contrast effect is obvious in case of the coarse mesh. The well-known alternation of minima and maxima on the edges of the wires is clearly seen. In case of the finer mesh some periodical fluctuations on the borders of the wires can also be seen.

Measurements of the thickness of the wires and the distances between them were performed as for ten measurements the average value and the standard deviation were calculated. The comparison between measured and declared values is shown in Table 2.3.

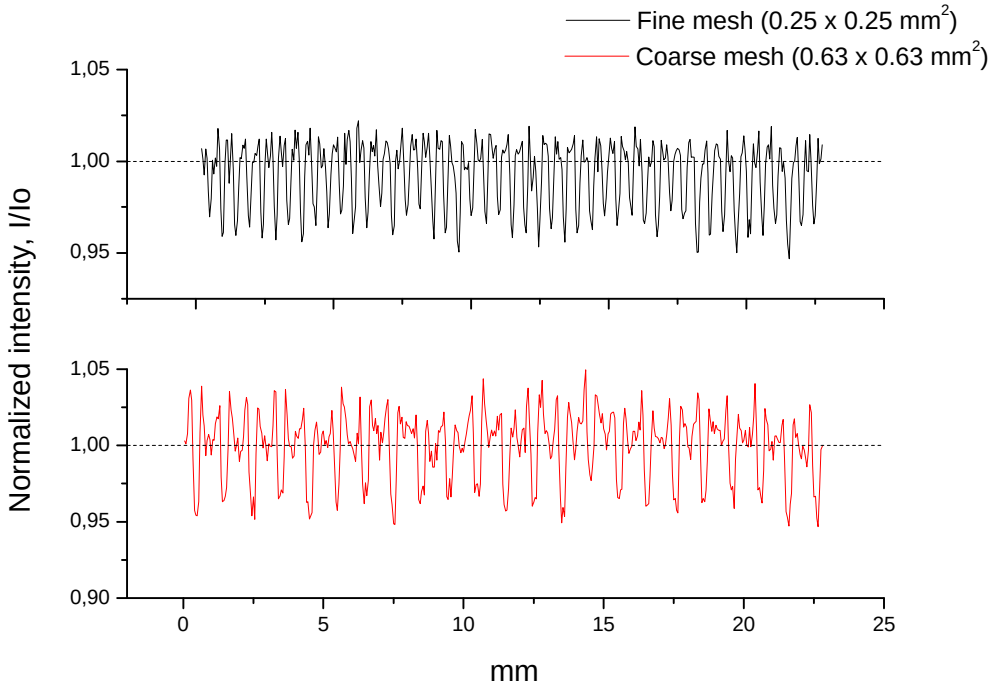

Figure 2.31 Intensity profiles taken through the meshes.

As seen the agreement between measured and declared values is excellent even for dimensions in the order of 0.2 mm.

Table 2.3:

	Fine mesh Wire diameter	Fine mesh Wire distance	Coarse mesh Wire diameter	Coarse mesh Wire distance
Tabulated value [mm]	0.17	0.25	0.25	0.63
Measured value [mm]	0.18 ± 0.02	0.23 ± 0.02	0.23 ± 0.02	0.63 ± 0.01

Increasing the neutron flux the statistics in phase contrast images will improve so that measurements with even better quality will be possible. With the new thermal radiography facility ANTARES, which is under construction at FRM II, the time for phase contrast measurements will be reduced to some minutes due to the higher neutron flux so that images with better quality in a reasonable time will be possible.

Chapter 3: Energy Selective Neutron Radiography and Tomography with Cold Neutrons

3.1. Definition

The neutron attenuation coefficient drops for many solid materials quite drastically at a defined cold neutron energy known as a Bragg cut-off in the cross-section diagrams. In many cases, the drop in attenuation for the corresponding elements is significant and this behaviour can be exploited to vary the material contrast in radiography and tomography images by modifying the spectrum of the applied neutron beam.

The reason for this phenomenon can be explained by the fact that neutrons with wavelengths larger than the lattice constant of the investigated crystal can not interfere coherently with it and therefore a drop in the total neutron cross-section is observed at a defined neutron wavelength.

The main advantage of the energy-selective radiography technique is the possibility to take pictures at different neutron energies. This feature can be used for very interesting neutron radiography and tomography applications such as material discrimination in composite samples, good transmission through thick objects and energy-dependent study of the neutron attenuation properties of various materials.

The inspiration and the motivation for further developing of this method came from the works of Th. Bücherl [Buc95] and McDonald [McD99] where the first energy-selective radiographs were shown.

Why cold neutrons

Depending on the employed neutron source the radiography techniques have their specific peculiarities. For cold neutron radiography the energies of the neutrons are between 1 and 10 meV. In todays existing steady or pulsed facilities cold neutrons are produced usually by so-called cold sources where a coolant with a very low temperature reduces the energy of moderated thermal neutrons to a few meV. The obtained neutron

beam possesses a broad Maxwellian-like spectrum with a mean energy value depending on the temperature of the cold source. The neutron transmission of different materials at these energies is very sensitive to the spectral characteristics of the neutron beam because of the above-mentioned Bragg cut off in their attenuation diagrams (Fig. 3.1).

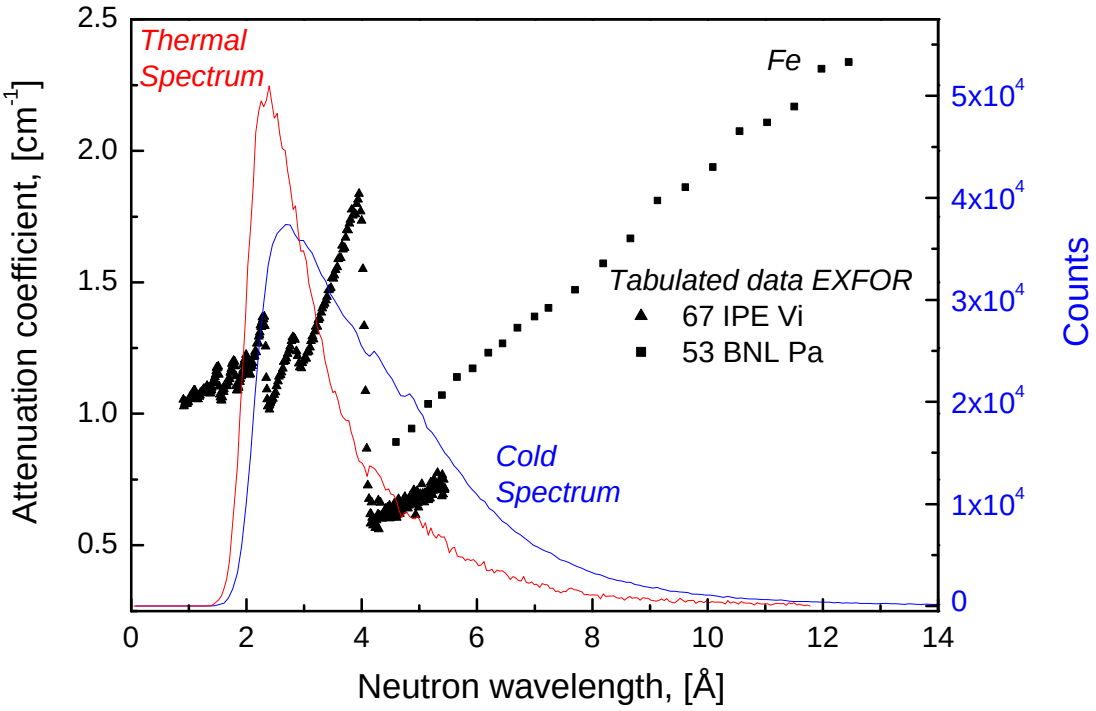

Figure 3.1: Two neutron spectra, measured at the QR beam position, FRM I with and without cold source in operation are shown together with the total cross-section diagram of iron. The Bragg cut of for Fe at 4 Å can be clearly seen.

In Table 3.1 the Bragg cut off wavelengths are given for various metals. It is obvious that the thermal spectrum can not be used effectively for radiography purposes in wavelength intervals above 4.0 Å because of the low neutron intensity (Fig. 3.1). On the contrary, the use of cold neutrons allows investigations with a high flux near the Bragg cut off energies of presented materials.

Table 3.1: Bragg cutoff wavelengths of some selected metals

Metal	Al	Be	Mg	Fe	Ni	Pb	Cu	Mo
λ (Å)	4.5	3.7	5.4	4.0	4.0	5.2	4.0	4.4

This was the reason that the energy-selective experiments were performed only on beam positions where cold neutrons were available – QR Meßhaus at FRM-I and PGA at SINQ.

Beam monochromatization

There are different ways to perform neutron radiography experiments at specific neutron energies. For instance, a Bragg reflection from a defined monocrystal can be used for a monochromatization of the neutron beam [Buc95]. Unfortunately, this method gives a weak intensity for the monochromated beam. At pulsed neutron sources a time-of-flight technique can be applied for achieving a narrow neutron energy distribution. In this way short, intense neutron pulses allow a very sharp spectrum in combination with a high flux [McD99].

Another way for an effective monochromatization of the neutron beam in the context of radiography and tomography experiments is the use of a neutron velocity selector [Kar01]. The advantages of the selector are its good transmission for a defined neutron wavelength and a sufficiently wide energy spectrum, yielding a high neutron flux, which allows the performance of tomography experiments in relatively short times. Other conveniences are its compact shape and the possibility to perform experiments in a straight geometry.

Velocity selector technique

The neutron velocity selector is a high-speed turbine, which is transparent only for those neutrons which manage to pass between the twisted lamellae inserted in the rotor in a time interval defined by the rotation speed of the selector. Thus neutrons in a certain speed range (or wavelength range) are selected (Fig. 3.2).

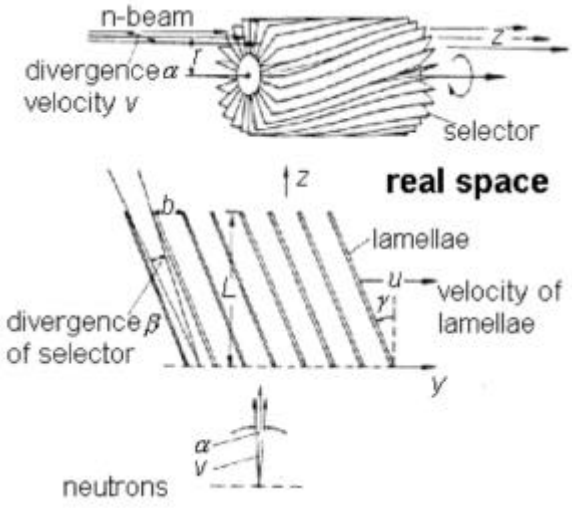

Figure 3.2: Selector of the helical lamella type

A simple formula for the selector transmission $T_m(\lambda)$ can be derived if the velocity selector is represented in the so-known velocity space (v-space) [Fri89] where the v-space distributions are approximated by Gaussian functions. In this case the transmission is also a Gaussian (Fig. 3.3) with a width

$$\Delta v(fwhm) = \frac{v_0\sqrt{a^2 + b_0^2}}{tgg} \tag{3.1}$$

and a maximum

$$T_m = T(v_0) = \frac{T_m^0 b_0}{\sqrt{a^2 + b_0^2}}, \tag{3.2}$$

where T_m^0 is the peak transmission for neutrons parallel to the rotor axis, b is the divergence defined between two adjacent lamellae, g is the tilted angle of the lamellae with respect to the beam and a is the beam divergence in front of the turbine. All the mentioned components and parameters are shown in the selector layout (Fig. 3.2) and in the v-space diagram presented in Fig. 3.3.

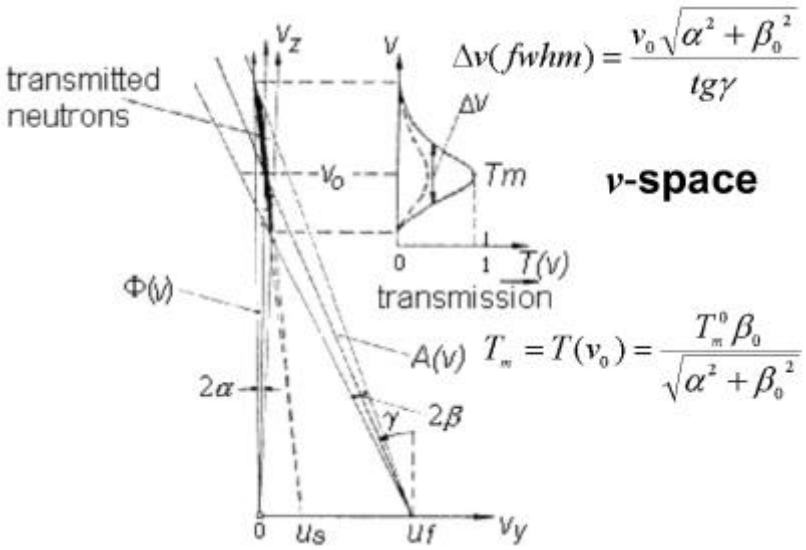

Figure 3.3: Selector representation in v-space. The bold line describes the transmitted neutrons for two different selectors with fast (u_f, solid lines) and slow (u_s, broken lines) angular speeds [Fri89].

The peak transmission T_m^0 can be calculated as the ratio of the transversal transmission area defined by the transmission channels in the selector to the whole transversal area defined by the rotor - $p\,r_{\max}^2$, where r_{max} is the radius of the rotor. The transmission cross-section of the rotor can be represented as the number of the channels, respectively the number of lamellae N, multiplied by the area of one transmission sector:

$$\frac{x}{360} p\, r_{\max}^2,$$

where x is the angle between two lamellae. Hence for the peak transmission T_m^0 we will obtain:

$$T_m^0 = N\frac{x}{360^o} \tag{3.3}$$

So that at known selector parameters as the number of lamellae N, the angle between two lamellae x, the selector divergence b, and at defined beam divergence a and neutron velocity v_o the velocity distribution of the neutrons transmitted through the selector can be simulated by formulae (3.1) and (3.2).

3.2 QR measuring position at FRM I

For the first test experiments a home made velocity selector of a helical lamella type was used at the end of the partially curved *Ni*-coated neutron guide QR at the FRM I reactor Garching. This beam position was preferred because of two reasons: First, the high neutron flux due to the neutron guide and second, the wide neutron spectrum due to the cold neutron source operated at this beam. These conditions are not typical for neutron radiography concerning the energy-dependent beam divergence produced by the neutron guide. Therefore an additional investigation was performed to obtain some quantitative estimation for the beam divergence. The parameters of the used home made selector at FRM I are described in Table 3.2.

Table 3.2 Velocity selector specifications

L, rotor length	D, diameter of the rotor	Number of lamellae	j, lamellae twist angle	r_0, effective radius of the rotor	b, distance between two lamellae at r_0	b_0, selector acceptance at r_0	g, lamellae tilt angle
1000 mm	232 mm	131	10.03^o	95 mm	3.99 mm	0.23^o	43.5^o

The selector housing was evacuated through a powerful turbo-molecular pump in order to eliminate the air resistance at the turbine rotation and to minimise the power dissipation in the system. A special magnetic coupling between the driving motor and the turbine has been developed to prevent large loads of the motor axis in case of strong accellerations. The selector did not need a cooling due to its relatively low maximum rotation speed of 6000 rpm. The speed was controlled through an external device which kept the speed constancy in order of 0.6 %.

The spectra obtained with the velocity selector for different circular velocities in revolutions per minute (rpm) measured with a standard time-of-flight technique (chopper in a combination with a ^{3}He detector) are presented in Fig. 3.4.

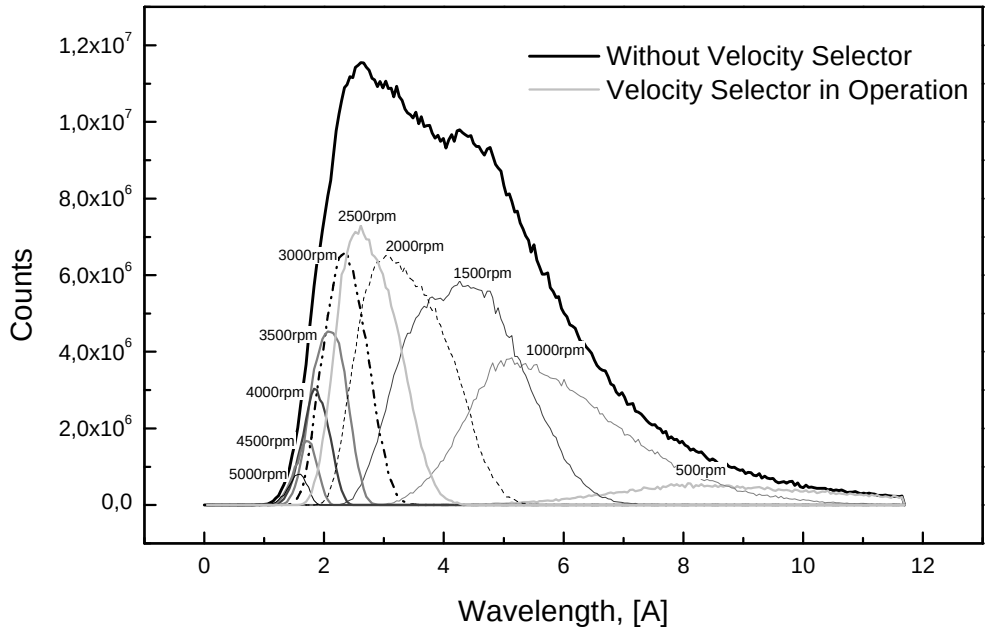

Figure 3.4: Spectra at different angular speeds of the selector

As it can be seen the selector covered the whole wavelength interval from 1.8 Å (max. 5000 rpm) to 8.5 Å (min. 500 rpm) which was optimal for our radiography purposes.

Spatial resolution

The influence of the beam divergence on the quality of the radiography picture and consequently on the tomography reconstruction is well known [Sch01]. That is why it is very important to know this characteristic for each neutron radiography setup - so-called L/D ratio [Appendix A1]. Since in our case the use of a neutron guide causes a considerable energy dependent beam divergence, an additional investigation was performed to estimate how the velocity selector influences the beam divergence. The representation of the velocity selector in the v-space mentioned above can help us to calculate the energy dependence of the neutron divergence. Considering formula (3.1) and the obtained spectra at different wavelengths (Fig. 3.4), we can calculate for these wavelengths the beam divergence $a(\lambda)$, using $\Delta v/v_0$ from experimental data and tan$g$, b_0 from the velocity selector's specification (Table 3.2). This dependence is presented in Fig. 3.5.

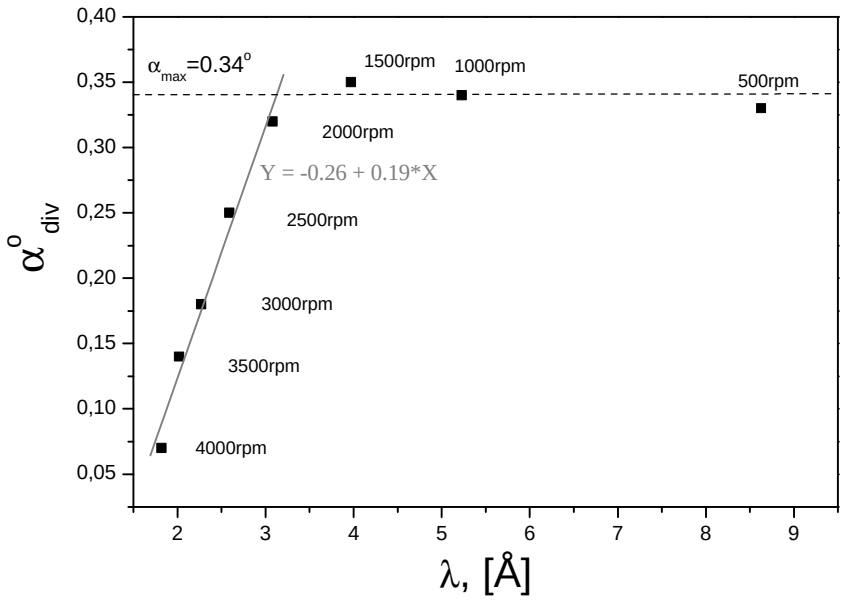

Figure 3.5: Dependence of the neutron divergence on the wavelength for a natural Ni coated guide

The slope of the fitted line shows how the divergence angle depends on the neutron wavelength. If we use the connection between the divergence angle a and the critical reflection angle of the used neutron guide q_C so that $a=2q_C$, we will obtain the wavelength dependence for q_C =0.095°/Å. The obtained result correlates very well with the calculated value for natural *Ni* of 0.099°/Å [Sch01a].

The points which are outside the linear regression can be explained with the maximum acceptance angle given from the velocity selector for a maximum radius of the rotor r_{max}=116 mm: $b_0(r_{max})=b_{max}/L$= 0.28° which is in a agreement with the value obtained from the graph a_{max}=0.34°±0.01° (Fig. 3.5). The obtained maximum divergence angle a_{max} will define in our case the L/D ratio = 1/tan(a_{max}) = 168. The so calculated value is much better than the measured value of 71 for the same measuring position without velocity selector [Sch01a]. The influence of the velocity selector on the neutron output beam acts as an additional collimator which improves the L/D ratio of the radiography setup.

Qualitative radiography measurements

A test radiography experiment was performed to check the performance of this new method. For this purpose a sample consisting of parallel Cu, Fe and Ti plates fixed together with a screw was produced. The plates were 21x16 mm with a defined thickness of 2 mm. The macroscopic attenuation coefficients of these three elements (Cu, Fe, Ti) together with the used neutron spectrum modification of the primary beam

(with a maximum correspondingly at 2.6 and 5.3Å) as a function of the neutron wavelength are plotted in Fig. 3.6.

A standard X-ray film Polaroid cassette with a 100 μm Gd converter was used as a detector. Because of the small beam hole size (rectangular shape 15x30mm), a scanning system was employed. The detector was scanned across the beam to illuminate the whole object.

Comparing the areas under the beam spectra in Fig. 3.6 one can calculate that the output neutron flux decreases approximately three times when a velocity selector is used in comparison with the intensity of the primary beam (the cold spectrum). Since the neutron flux without velocity selector in operation was measured in order of 10^8 n/cm^2/s, the expected value for the neutron intensity in the energy selective radiography experiments was estimated in order of 3.3×10^7 n/cm^2/s.

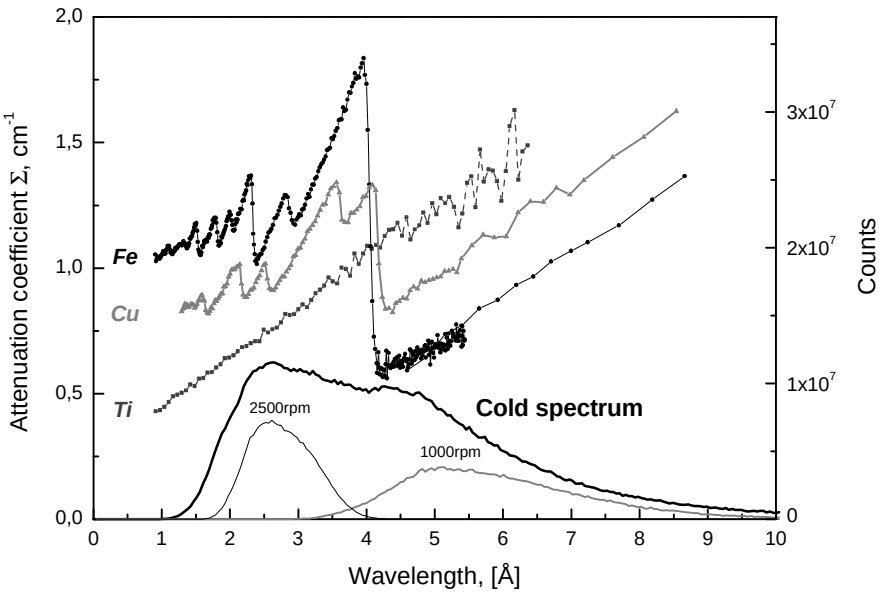

Figure 3.6: Energy dependence of the attenuation coefficients of titanium, copper and iron. The neutron spectra used at the radiography experiments are also shown.

The obtained radiography images for two spectral modifications of the beam (2.6Å and 5.3Å) are shown without normalisation in Fig. 3.7.

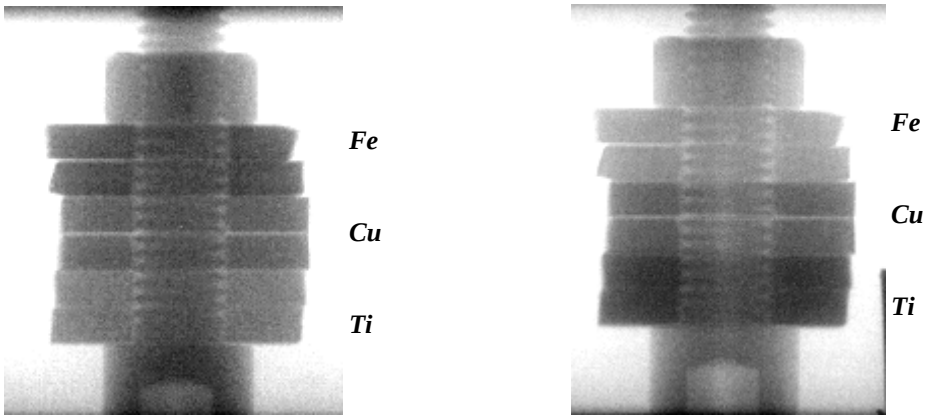

Figure 3.7: Neutron radiography of a test object at two neutron wavelengths 2.6Å (left) and 5.3Å (right).

At different neutron wavelengths different contrast between the metals was achieved as it is obvious in the pictures. The darker areas correspond to a bigger attenuation of the neutron beam. The result is in agreement with the presented cross-section diagram (Fig. 3.6). One can see that in the picture obtained at 2.6Å (Fig. 3.7 left) the darkest material is Fe and the lightest is Ti because iron possesses the biggest attenuation coefficient for this range of wavelengths and titanium the smallest. In contrary to this, titanium has the highest attenuation coefficient at a neutron wavelength 5.3Å and iron the lowest. This fact is in an agreement with the presented radiograph in Fig. 3.7 (right) where the lightest element is iron and the darkest is titanium.

Energy-selective tomography

These first qualitative results gave the motivation for further energy-selective tomography investigations. The tomography experiment was performed also at the QR beam position. For this purpose, a radiography detector available at the reactor FRM I of TU Munich was used in combination with a rotation table in front of it. The detector consisted of a ^{6}LiFZnS:Ag scintillator projected through a mirror and a lens system on a 10 x 10 mm^2 cooled CCD chip (Thompson TH7895 AVRLN) with 512 x 512 pixels, 19 x 19 μm^2 each. The dynamic range of the camera was 16 bit and at the so-used optical configuration the projection ratio was 332 μm/pixel. The detector design is described in details elsewhere [Sch96]. Because of the restricted neutron flux from the velocity selector the measuring time per one tomography projection was increased. Usually the experimental time per one projection without selector was within the range of 1 min. In our case with the velocity selector in operation the time per one projection reached 3 min. For this experiment a set of 100 projections was used which gives approximately 5 hours experimental time.

A small electromotor (3x3 cm^2) was investigated at a defined neutron spectrum with a maximum at 5.3Å (see Fig. 3.8). The distance between the object and the detector was as small as possible with 25 mm. In spite of the bigger beam divergence due to the neutron guide, 3D tomography pictures with a good quality were obtained (Fig. 3.8). A

small defect (a saw cut) with a width of ~1 mm in the corpus of the motor was used as a resolution test. The section is marked with an arrow in Fig. 3.8 a (photo of the motor) and Fig. 3.8 d (3D tomography reconstruction). The fact that the axis of the rotor does not coincide with the vertical geometric axis of the motor is obvious (Fig. 3.8 b - photo of the motor and Fig. 3.8 e - 3D tomography reconstruction).

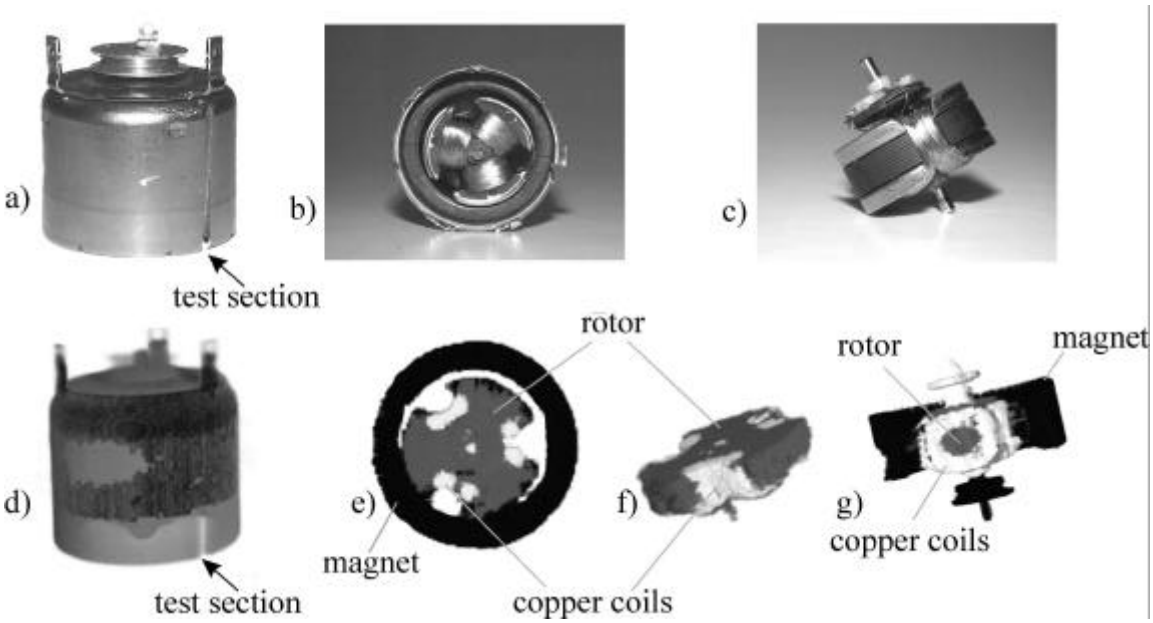

Figure 3.8: Comparison between photo pictures of the motor and results from a 3D-tomography reconstruction. A successful segmentation of different parts of the electric motor is also presented.

The obtained reconstructed images show that we have a good discrimination between the tomography values for copper (rotor coils) and iron based (the rotor) parts (Fig. 3.9 a). Such a discrimination is impossible in case of a standard neutron tomography, where a thermal neutron beam without spectral restrictions was used (Fig. 3.9 b). This result is one of the main advantages of the energy-selective neutron tomography because it gives a good opportunity for a segmentation of areas which correspond to different materials in the investigated object. Such a segmentation is presented in Fig. 3.8 e, f, g. where the discrimination between the copper coils and the rotor can also be seen.

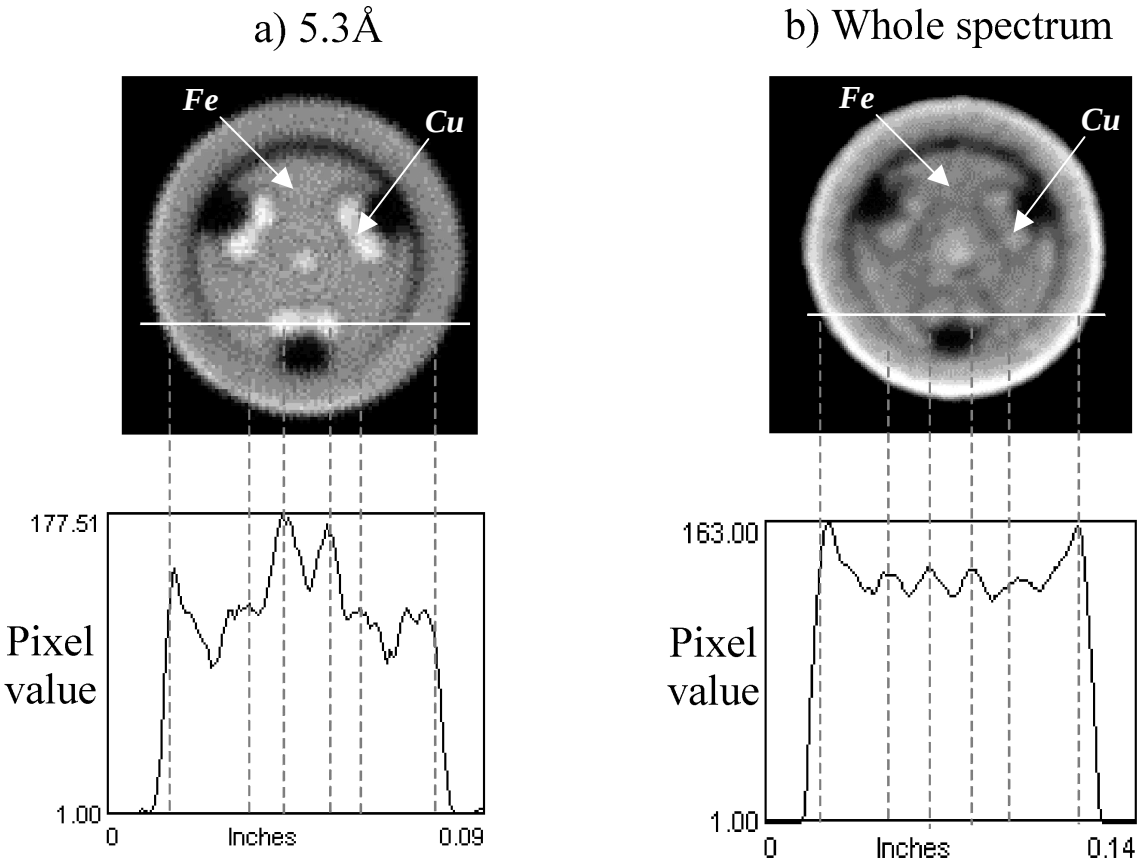

Figure 3.9: The level of obtained discrimination between the copper coils and the iron rotor in case of a) neutrons with mean energy at 5.3Å and b) whole neutron spectrum with mean energy at 2.3Å.

3.3 Measurements at SINQ, PSI - PGA beam position

The consecutive measurements were performed at PSI, Switzerland, where better experimental conditions were prepared. For this purpose a new type velocity selector produced by Astrium GmbH with larger input-, output-windows and better transmission was used.

The selector was installed at the PGA station using cold neutrons provided by the spallation source SINQ [Bau98]. At the Neutron Guide Hall, where the PGA beam position was located, (Fig. 3.10), the cold neutrons are transported to the experiments by means of super-mirror coated neutron guides. The coating gives an increase of the critical angle of reflection by a factor of two when compared with common Ni coated guides. Therefore, the flux at the end of the guides is considerably improved and the transmitted spectrum has a gain into the thermal range. However, a bigger critical angle of reflection implies a higher divergence of the beam. In other words, super-mirror guides have a lower L/D-ratio than Ni coated guides. The last 10 m of the PGA neutron

guide are coated with pure Ni. The beam size at the exit of the guide is 20 mm wide and 50 mm high and the neutron flux at the sample position is about $1.8 \cdot 10^8$ n/cm^{2}s.

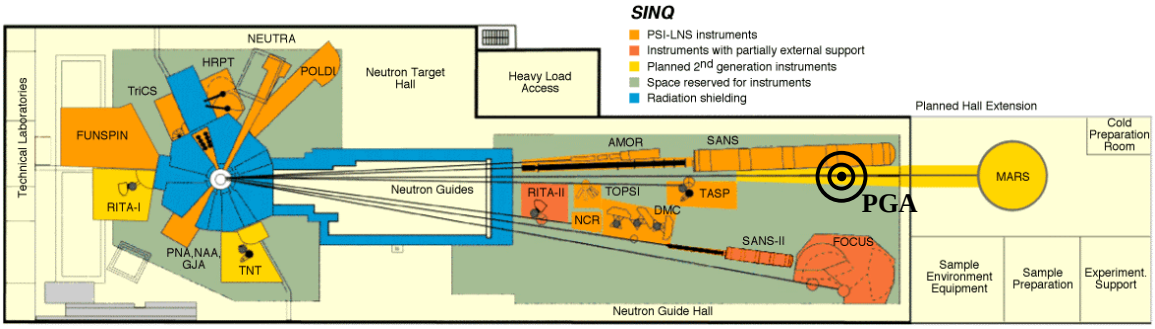

Figure 3.10: SINQ layout. The position of the PGA station is marked with concentric circles.

A detection system similar to the one used before at FRM I was placed behind the selector (Fig. 3.11). The visible light emitted from the ^{6}LiF/ZnS(Ag) scintillator plate exposed to the neutron beam was imaged with an optical lens onto a Peltier-cooled CCD camera via a mirror at a 45 degree angle. The CCD-sensor had a scan area of 8.6x6.9 mm^2 covered by 1280x1024 pixels (6.7 µm square pixels), a dynamic range of 12 bits (4096 gray-levels per pixel) and a fast read-out time of 8 full frames per second. The optical configuration resulted in a pixel size of 26 µm and thus a field of view of (2.7x3.4) cm^2. The data stream is transferred via a fiber optic cable connecting camera and PCI-Interface-Board. Software for controlling the camera settings, displaying and storing the images was developed on Labview©. The detection system has been described in more details elsewhere [Bae02].

The used velocity selector was a new generation selector produced by Astrium GmbH (the former Dornier Systems) [Wag92]. The turbine, which was 290 mm in diameter and 250 mm in length, consisted of 72 blades of carbon-fiber composite material coated with ^{10}B. The possible angular speeds of the turbine were between 3000 and 28300 rpm with a speed constancy of 0.2%. The case enclosing the rotor included two windows covered by 0.4-mm-thick aluminum foils for neutron entry and exit. In addition the rotor temperature was kept between 15-25°C and the vacuum below 10^{-3} mbar by vacuum and cooling systems. The selector was controlled and operated with its control and monitoring program on a PC.

The wavelength distribution of neutrons is not only dependent on the rotation speed, but also on the tilting angle between the rotation axis and the neutron beam [Wag92]. Thus, the velocity selector was fixed on a appropriate tilted table in order to achieve the desired neutron energy range (Fig. 3.11). The tilting angle z chosen at 12.7° gave a suitable energy interval from 2.56 Å (at maximal speed) to 10.50 Å (at minimal speed), except between 4.48 Å and 5.24 Å as well as 8.08 Å and 9.35 Å due to resonance frequencies of the selector. The energy resolution $\Delta\lambda/\lambda$ of the neutron distribution at the exit of the selector depends only on the tilting angle z and was in order of 30 %. So, neutron beams with relatively wide energy spectra were used for radiography

investigations. In this way, the beam intensity was still reasonable at different neutron energy ranges to perform radiography experiments in short measuring times. This advantage was particularly suitable for tomography measurements.

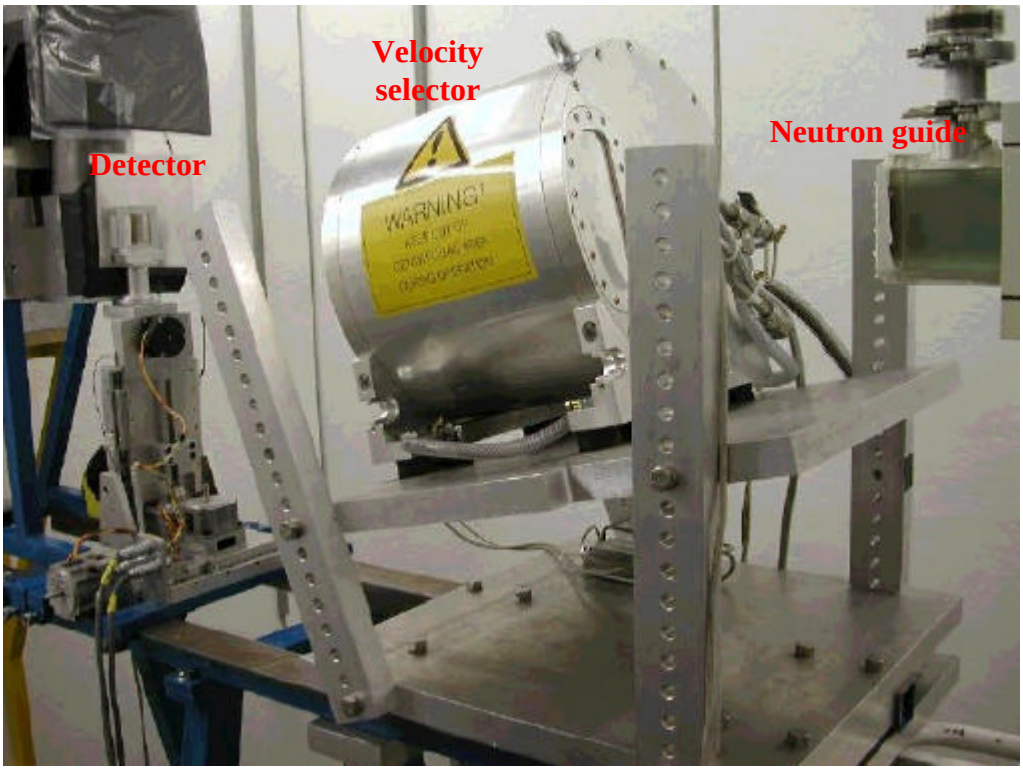

Figure 3.11: Positioning of the neutron velocity selector at the PGA beam line for radiography and tomography purposes.

Properties of the beam

A line profile was extracted horizontally across the image of the beam distribution for different neutron wavelengths. At short wavelengths, the line profile showed a significant breakdown on the right side. With increasing wavelength, this inhomogeneity was first leveled off more and more and finally translated to the left side (Fig. 3.12). The wavelength dependence of the distribution over the width resulted from the curvature of the guide and the structure of beam profiles could be qualitatively verified by phase-space considerations [Wag98]. To prove the reproducibility of inhomogenities, a beam distribution pattern was measured two times under the same conditions. After dividing both images, the arithmetic mean μ and the standard deviation σ were calculated over a region of interest. The signal variation given by σ/μ [%] never exceeded 1.5 % independently on the wavelength and thus showed a good reproducibility of the velocity selector in combination with the detector. The intensity of the transmitted beam was measured for different wavelengths and compared with the intensity of the white beam, i.e. the distribution without the velocity selector. For this purpose, the mean gray level value was calculated for each image and normalized by the

exposure time. Plotting the relative intensity versus the wavelength gave the spectral neutron distribution of the white beam at the PGA guide (Fig. 3.13). Then, a semi-empirical L/D = 1/tan($2\gamma_c$) was estimated by calculating the arithmetic mean value of all wavelengths as [Sch01a], [Appendix A1]:

$$l_{av} = \frac{\sum_i l_i \cdot n_i}{\sum_i n_i} = 5.0 \pm 0.2 \text{ Å} \tag{3.4}$$

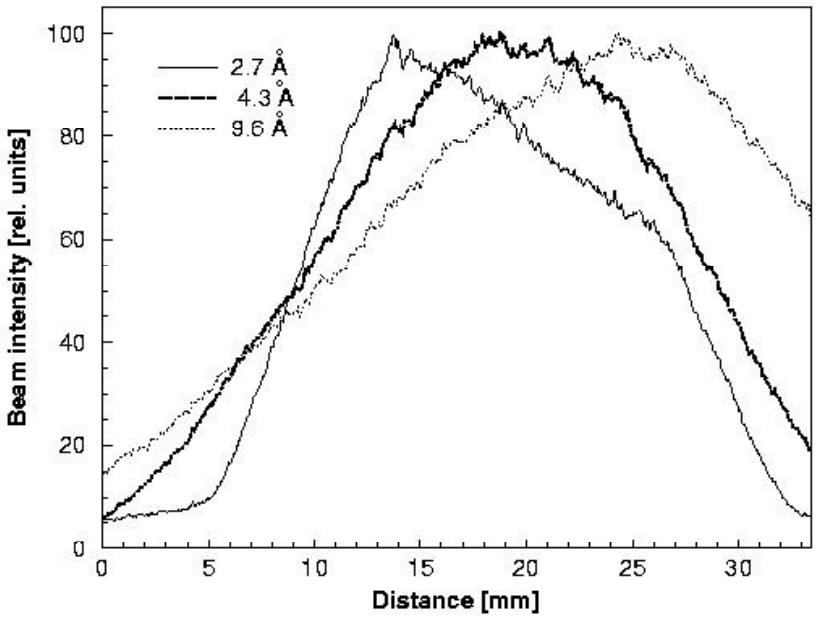

Figure 3.12*: Intensity profile over the width of monochromatic neutron beams at 2.7Å, 4.3Å and 9.6 Å.

With the critical angle $\gamma_c = 0.1°/Å$ of a guide coated with natural nickel, a L/D of 57 was obtained. This estimation was available for a constant angular distribution of neutrons. In reality, imperfection of the guide decreased the reflectivity essentially at big angles, leading to a smaller effective divergence and thus a greater L/D. Finally, the fully experimental L/D-ratio of 68 ± 2 determined previously [Bae02] was more reliable.

* The data represented in Fig. 3.12 were processed by Dr. S. Baechler, University of Fribourg, Switzerland.

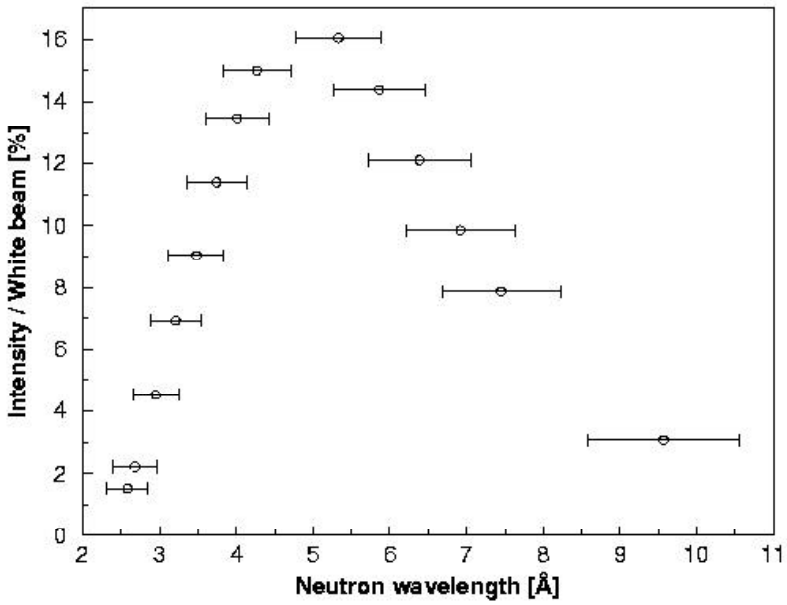

Figure 3.13[*]: Relative intensity of transmitted beams measured for different wavelengths yielding approximately the spectral neutron distribution of the white beam.

Energy and spatial resolution

Because of the lack of space behind the selector there was no possibility to use a time-of-flight technique for a measurement of the obtained neutron spectra at various angular speeds of the turbine, therefore the positions of the maxima of the transmitted spectra λ [Å] at different speeds of the selector turbine v[RPM] were defined by a calculation procedure based on the expression [SANS]:

$$l(v,z) = \frac{A(z)}{v} + B(z), \tag{3.5}$$

where $A(z)$ and $B(z)$ were experimentally determined parameters depending only on the rotor tilt angle z.

To ensure the calibration relation a simple experiment with a known test sample was performed. The sample consisted of plates from different materials (Cu, Fe, Al, Steel, Pb, Plexiglas (PMMA) and Teflon) with a constant thickness of 5 mm. Using an exponential attenuation for neutrons, $-\ln(I/I_0)=Sd$, the attenuation coefficient S for each material depending on the neutron wavelength was calculated. The ratio I/I_0 was determined by dividing radiography pictures taken with and without positioning of the sample in the beam. The calculated values for Cu and Fe were compared with tabulated cross-section data [EXFOR] in Fig. 3.14 a, b. In spite of the poor energy resolution of

[*] The data represented in Fig. 3.13 were processed by Dr. S. Baechler, University of Fribourg, Switzerland.

the velocity selector technique ($\Delta\lambda/\lambda$ ~ 30% in our case), the good agreement was a proof that the calibration was done in the right way.

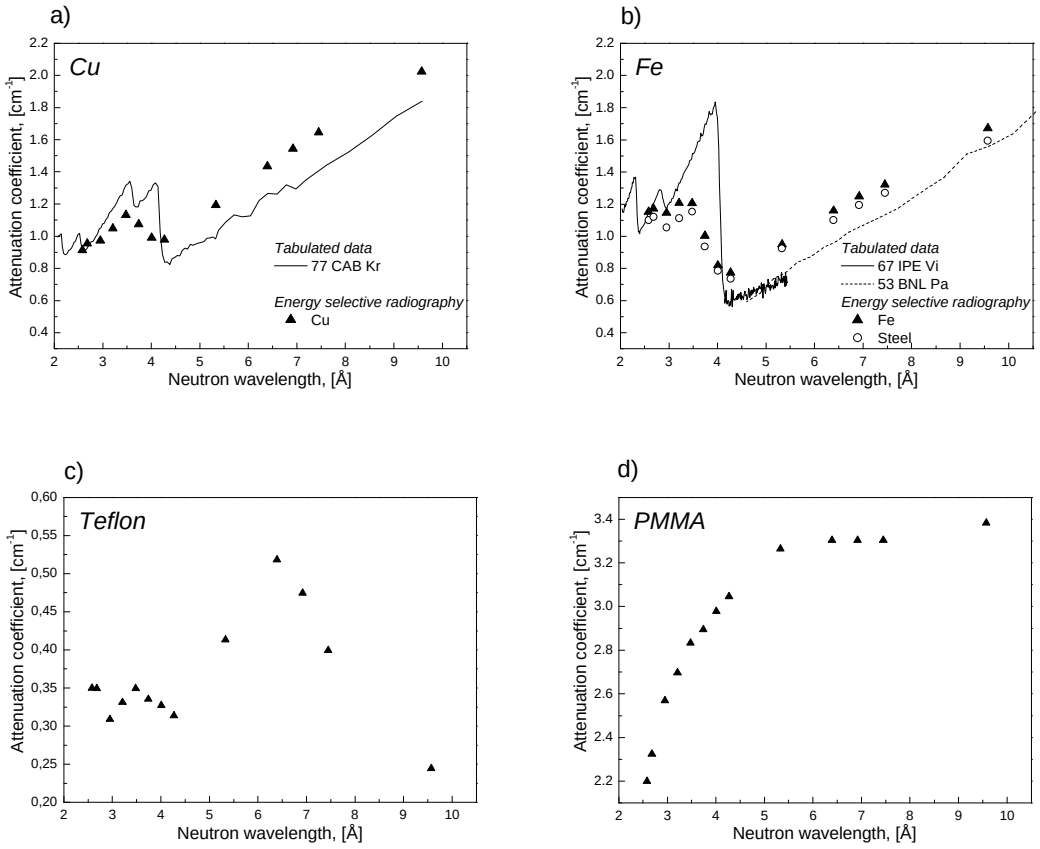

Figure 3.14: Comparison between measured and tabulated energy dependent attenuation coefficient values for a) Cu, b) Fe and steel, c) Teflon (measured only) and d) PMMA (measured only)

Three materials (PMMA, Teflon and steel) with a complicated chemical composition were also investigated in this experiment. The obtained diagrams for them are shown in Fig. 3.14 b, c and d. As it can be expected the steel attenuation values were very close to those of iron due to their common compound material – Fe. The PMMA ($C_5H_8O_2$) diagram is also logical taking into account that it is preferentially a hydrogenous material and it should follow the attenuation behaviour of hydrogen – monotonic increase of the attenuation with increase of the neutron wavelength. The saturation behaviour of the attenuation coefficient seen in Fig. 3.14 d can be explained with the fact that the absorption probability increases with the increase of the neutron wavelength, so that beyond some defined wavelength the signal of transmitted through the sample neutrons becomes negligible in comparison with the existed constant background. In this case the detected signal stays a constant with the further increase of the wavelength which leads to the observed wavelength independence of the attenuation

coefficient. In the Teflon diagram a nonuniform energy dependence of the attenuation in comparison with the other elements can be seen.

This method can be used further for raw energy-dependent estimations of the attenuation properties for various materials.

The influence of the selected neutron wavelength on the divergence angle was investigated by measuring a "knife-edge" at 5 cm distance from the scintillator plate. Then, the spatial resolution was determined conventionally by measuring the 10% to 90% response on the ESF (Edge-Spread Function) (Fig. 3.15). At short wavelength, the resolution was considerably improved compared to the measurement performed without the velocity selector. The resolution at 5 cm distance from the converter reached 0.45 mm with the 2.7 Å monochromatic beam, instead of 0.85 mm using the white beam. In this case, the selector worked as a collimator, thus enhancing the L/D ratio. Although increasing the wavelength gradually degraded the image sharpness, a plateau was reached above 6.5 Å. Indeed, the divergence was restricted by the maximum acceptance of the velocity selector and became constant for the low energy component of the neutron spectrum.

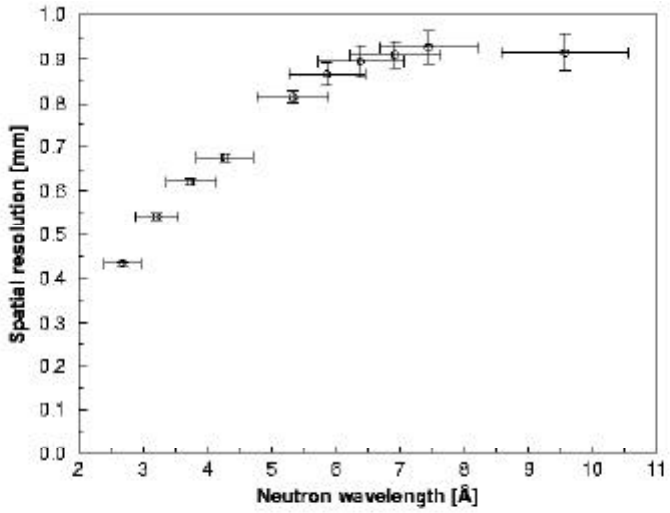

Figure 3.15*: Neutron wavelength dependence of the beam divergence on the spatial resolution measured at 5cm distance from the scintillator plate.

For instance, a dried hornet was imaged using a neutron beam at two different wavelengths, 2.7 and 5.3 Å (Fig. 3.16). The specimen was fixed on a needle located at 2.5 cm from the converter plane. Both radiographs distinctly showed the three parts of the insect: the head with strong mandibles, the thorax to which three pairs of legs are attached and the abdomen tipped with the stinger. The wings were nearly transparent to neutrons and thus hardly visible on the radiographs. As expected, the monochromatic beam at 2.7 Å (short wavelength) yielded sharper edges and reproduced finer details in

* The data represented in Fig. 3.15 were processed by Dr. S. Baechler, University of Fribourg, Switzerland.

the image. On the other hand, the contrast was improved at 5.3 Å due to the increment of attenuation coefficient in organic material at higher wavelengths.

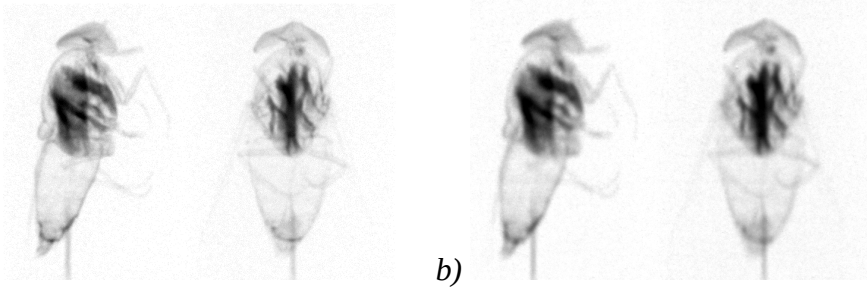

a) *b)*

Figure 3.16[*]: Profile and face radiographs of a 20mm long dried hornet a) at 2.7 Å and b) 5.3 Å.

Energy-selective neutron radiography

Radiography experiments were performed at different angular speeds of the selector turbine corresponding to defined neutron energy intervals. As it can be seen in Fig. 3.4, the obtained transmitted spectra have unequal integral areas, which meant that the neutron flux varied also with the neutron wavelength. To achieve the right normalisation conditions, an open beam picture (without sample in the beam) was taken before each measurement at the same energy range and exposure time. In this way all the pictures were normalised by division to the corresponding open beam image. Furthermore the normalised pictures were free from beam inhomogeneities usually arising from the structure (joints) of the neutron guide. Because of the small illuminated area (WxH) of 20x50 mm^2, scanning in horizontal and in vertical direction was used for larger objects. Some interesting applications of the energy-selective radiography were found by investigation of different objects.

- ***Variation of the radiographic contrast***

Essentially, the radiographic contrast is the degree of intensity difference between adjacent areas on a radiography image. It is possible to radiograph a particular object and, by varying the neutron spectra through the velocity selector, produce two radiographs possessing different contrast levels. If we take two areas from the radiography image corresponding to different sample materials, the contrast between them will depend on their attenuation factors: $Sd = -\ln(I/I_0)$, where S and d are correspondingly the attenuation coefficient and the material thickness, I_0 denotes the primary intensity and I the intensity attenuated by the sample. In case of equal attenuation factors $S_1d_1=S_2d_2$ these two materials will be indistinguishable on the radiographic image. The only chance to achieve some contrast for the desired material in respect to others is to find such a neutron energy range where its attenuation factor

[*] The data represented in Fig. 3.16 were measured and processed by Dr. S. Baechler, University of Fribourg, Switzerland.

will differ considerably. An example for this is the radiography inspection of an ancient roman brooch with thermal neutrons (NEUTRA, PSI) [Leh99] and with a cold neutron spectrum at 6 Å modified by the selector (Fig. 3.17).

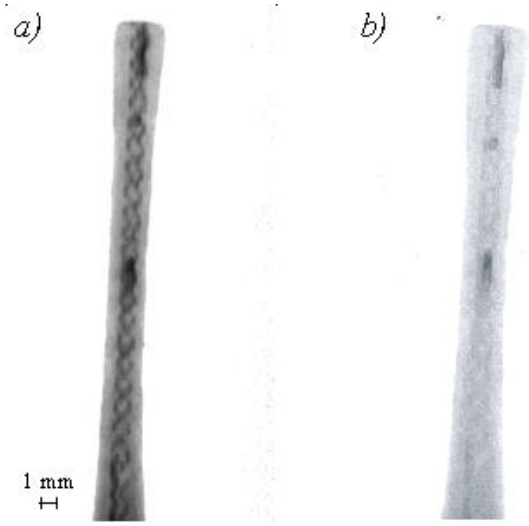

Figure 3.17[*]: Radiographs of an ancient roman brooch taken with a) energy selective neutron radiography – 6 Å and b) standard thermal neutron radiography technique – NEUTRA (Courtesy of the Museum Aventicum, Switzerland).

A fine silver chain incrusted on the surface of the brass body can be clearly seen with cold neutrons but not with thermal neutrons. The reason for the improved contrast in the first case is the larger increase of the attenuation coefficient for silver than for copper with increase of the neutron wavelength (Fig. 3.18) so that the attenuation factor Sd for the thin silver ornament becomes higher.

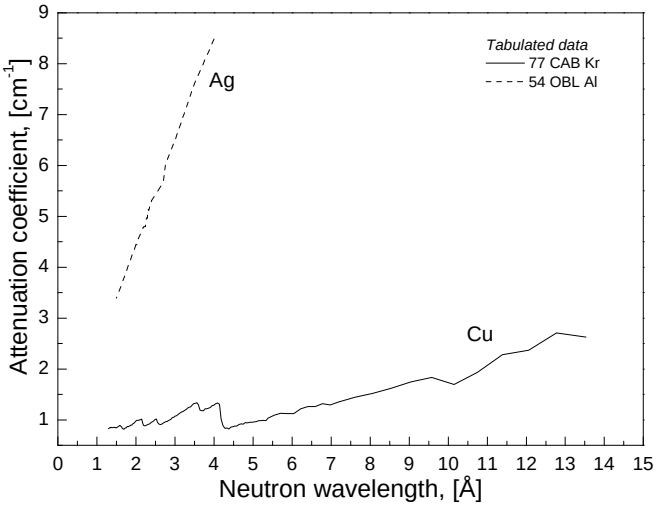

Figure 3.18: Comparison between tabulated neutron attenuation diagrams for Cu and Ag.

[*] The image shown in Fig. 3.17 b was placed at our disposal with the kind permission of Dr. E. Lehmann, PSI, Switzerland.

Using energy-selective radiography, optimal conditions for better visualisation of fine details could be prepared.

- ***Radiography of thick samples***

The energy-selective radiography can be helpful for the examination of thick samples. Varying the neutron spectrum by the selector, an appropriate neutron energy range can be found where the corresponding material posses a smaller attenuation coefficient. In Fig. 3.19, normalized transmission profiles of a steel step wedge taken at different neutron wavelength ranges are shown. It can be seen that around the Bragg cut off of iron of ~4Å (see Fig. 3.16 b) the obtained neutron transmission is much better than at the other energy intervals. The energy-selective data were compared also with a standard transmission measurement performed with thermal neutrons (NEUTRA [Leh99]).

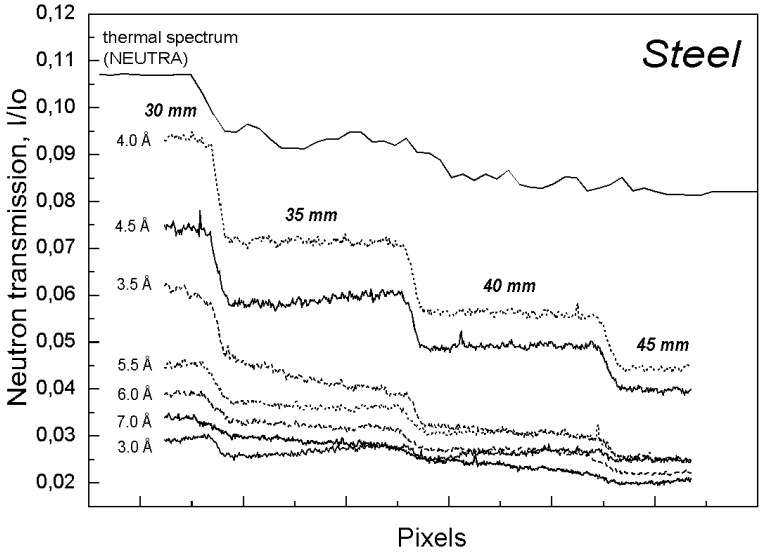

Figure 3.19: Normalised transmission profiles of a steel step wedge taken at different neutron wavelength ranges. The thickness of each step is marked above it.

At these thicknesses the signal from transmitted neutrons is very low and it can be easily overlapped by the existing background. For example, Figure 3.19 shows that in the intensity profiles at the neutron wavelengths 3.0 Å , 6.0 Å, 7.0 Å and at the thermal spectrum, the step wedge profiles are strongly blurred.

- ***Material transparency***

Looking at the attenuation diagrams shown above in Fig. 3.14, one can see that due to the Bragg cut off at some neutron wavelengths we have the same attenuation coefficients $\Sigma(\lambda_i)=\Sigma(\lambda_j)$. Then the division of the pictures obtained at such neutron wavelengths will make the defined material “transparent” in the resulting picture. If we

assume an exponential attenuation of the neutron beam for one defined point of the sample then after the division of two normalized images obtained at two different neutron wavelengths λ_1 and λ_2 we will have:

$$\frac{I_1/I_{01}}{I_2/I_{02}} = \frac{e^{-\Sigma(l_1)d}}{e^{-\Sigma(l_2)d}} = e^{[\Sigma(l_2)-\Sigma(l_1)]d}, \qquad (3.6)$$

where the used indices 1 and 2 correspond to the two respective neutron wavelengths. The expression (3.6) is in the order of one when the values for $\Sigma(\lambda_1)$ and $\Sigma(\lambda_2)$ are equal or when d=0 (no sample in the beam). Therefore the contrast for the corresponding material with equal $S(\lambda_1)$ and $S(\lambda_2)$ in the resulting image will be the same as the field outside the sample, i.e. it becomes “transparent”.

In Table 3.3 such attenuation coefficients which are equal for two different wavelengths $\Sigma(\lambda_1)=\Sigma(\lambda_2)$ are presented for various materials. The data were experimentally determined using the velocity selector.

Table 3.3:

Material	λ_1, [Å]	λ_2, [Å]	$S(\lambda_1)=S(\lambda_2)$, [cm^{-1}]
Fe	2.68	6.39	1.16
	3.21	6.92	1.23
	3.78	5.38	0.96
Cu	2.95	4.27	0.97
	3.48	5.12	1.13
Pb	2.68	3.74	0.18
	6.39	7.45	0.07
Al	2.58	3.48	0.14
	4.01	5.33	0.10
	6.39	7.45	0.11
Plexiglas	6.39	7.45	3.30
Teflon	2.95	4.27	0.31
	5.28	7.42	0.40

The procedure was tried on the test object used for the calibration measurements described above, (Fig. 3.14). The obtained pictures are shown in Fig. 3.20. It can be easily seen that the contrast for Cu and Teflon in Fig. 3.20 b, Fe and steel in Fig. 3.20 c, and Al, Pb and Plexiglas in Fig. 3.20 d is completely suppressed. The observed contours in the resulting pictures were related to the different image sharpness determined by the energy dependent beam divergence.

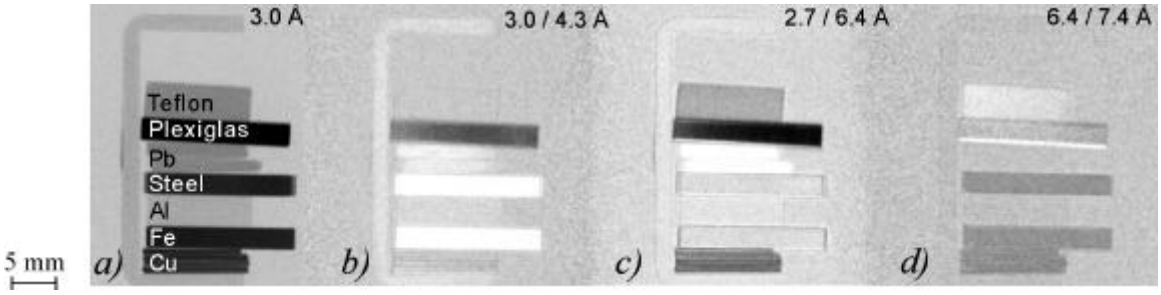

Figure 3.20: Radiographic image of a test sample obtained at a neutron wavelength of a) 3.0Å and resulting images after division of radiographs taken respectively at b) 3.0 Å and 4.3 Å, c) 2.7 Å and 6.4 Å and d) 6.4 Å and 7.4 Å.

The method was also applied to a radiography inspection of a standard spark plug. Two radiographs were taken on both sides of the Bragg cut off of steel, where the attenuation coefficients were approximately equal (see Table 3.3). Then, it was possible to make the steel components invisible by dividing both images. In Fig. 3.21, both radiographs taken at 6.9 Å, Fig. 3.21 a, and 3.2 Å, Fig. 3.21 b, show apparently the same contrast. However, after the division, the steel cladding became transparent and the dark structure (the electrode) inside the device was completely resolved (Fig. 3.21 c). Neither X-ray nor the known standard neutron radiography methods were able to obtain such information.

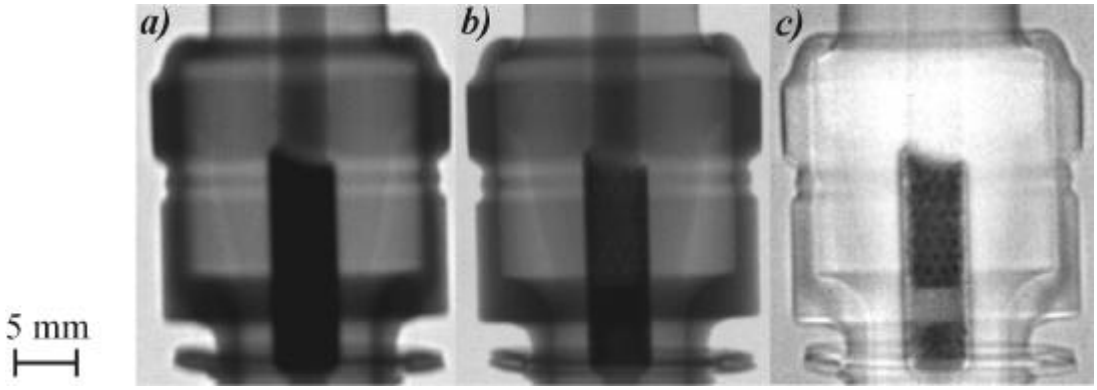

Figure 3.21: Radiographs of a spark plug at 6.9Å (a) and 3.2Å (b). The division of both images (c).

- ***Material discrimination in radiography images***

On the normalized radiographs we usually have information about the attenuation of the initial beam depending on the sample material and its thickness.

If we want to eliminate the contribution of the sample thickness on the radiography image a simple post-processing procedure can be performed. For radiographs taken at two different neutron spectra the following ratio can be calculated from (3.6) for every image pixel:

$$\frac{\ln(I_1/I_{01})}{\ln(I_2/I_{02})} = \frac{\Sigma(l_1)}{\Sigma(l_2)}, \tag{3.7}$$

where I_{01} and I_1 are the pixel responses before and after positioning of the sample in the beam at the first neutron wavelength and I_{02} and I_2 are the corresponding pixel responses at the second neutron wavelength. $\Sigma(\lambda_1)$ and $\Sigma(\lambda_2)$ are the attenuation coefficients for the investigated material at the two used neutron spectra. In this way in the resulting image the thickness of the material will be irrelevant and the obtained contrast will be only due to the different material composition. This effect can be observed in Fig. 3.22 b where in the resulting picture different parts of a pyrotechnic cutter [Bay99] corresponding to different materials can be clearly located. For example in the middle of the sample a cylindrical part can be clearly recognized (Fig. 3.22 b). Such an information cannot be extracted directly from the radiography pictures shown in Fig. 3.22 a.

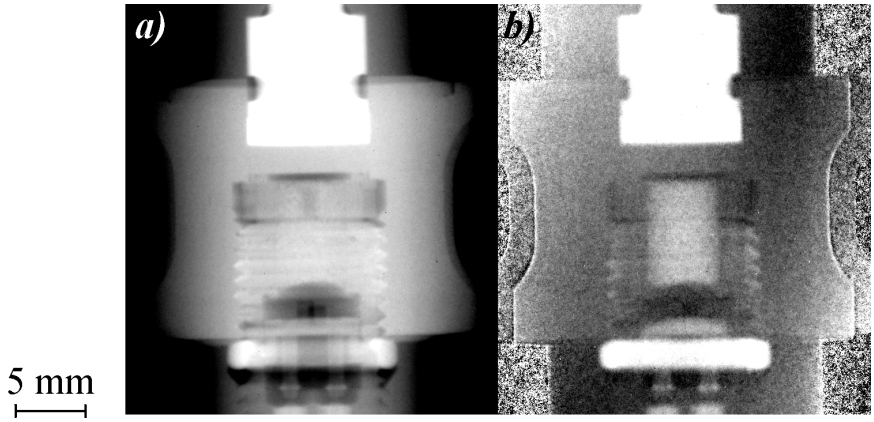

Figure 3.22: A radiograph of a pyrotechnic cutter (Dassault-Aviation) taken at 3.0 Å (a) and a resulting picture after the division of the normalized and natural logarithmic processed images at 2.9 Å and at 3.2 Å (b).

A tomography investigation of the same pyrotechnic cutter is shown in Fig. 3.23. The comparison of the material discrimination by an energy-selective radiography and a 3D tomography reconstruction gives a good agreement. So the proposed method can be used as a preliminary fast inspection tool to determine the distribution of a defined material in the corresponding sample and to fix the more interesting positions for a consequent detailed tomography examination.

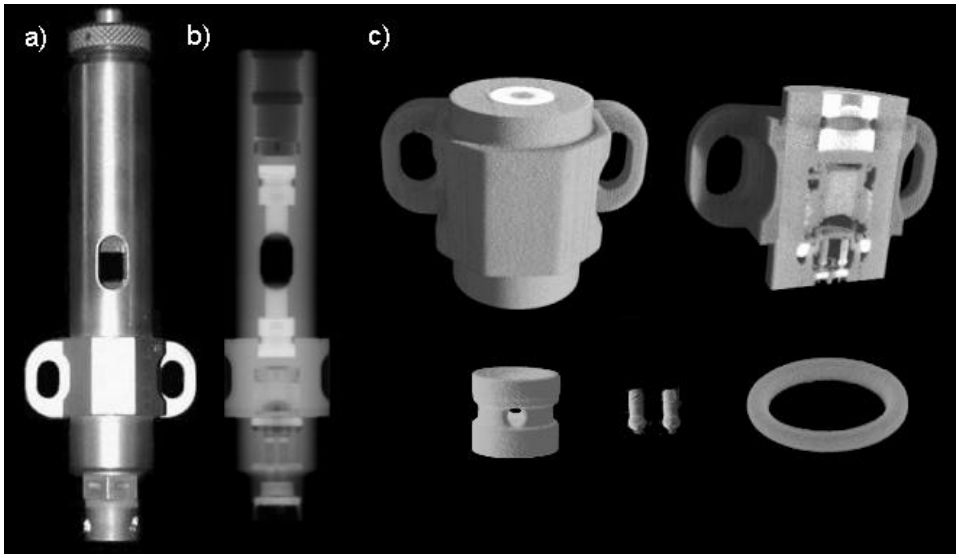

Figure 3.23*: Quality control of a 12 cm height pyrotechnic cutter a) picture b) neutron radiograph, c) partial reconstructed volume and segmented components.

Energy-selective neutron tomography

The tomography experiments were performed with the same experimental setup where the sample was fixed on a precise rotation table. Because of the restricted neutron flux from the velocity selector the measuring time per one tomography projection was increased. Typical measuring times for one tomographic projection were between 10 and 50 s which determine the duration of one tomography experiment from 200 projections in a time range between 30 and 90 min respectively.

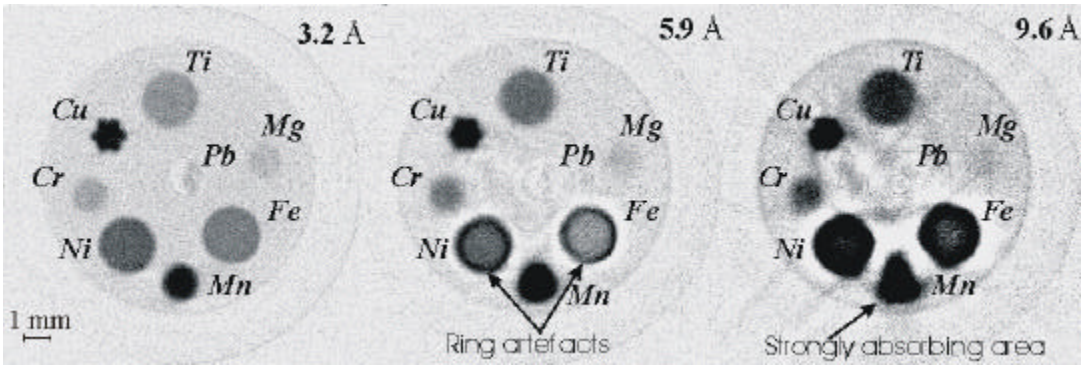

Figure 3.24: Horizontal reconstructed slice of a test sample for tomography experiments performed at three different neutron wavelengths.

First the energy selective technique was used to study the spectral dependence of the quality of reconstructed tomography slices. For this purpose a simple test sample was

* The data represented in Fig. 3.23 were measured and processed by Dr. S. Baechler, University of Fribourg, Switzerland.

prepared. In an aluminum cylinder (1.5 cm diameter), holes with different sizes were drilled parallel to the cylinder vertical axis and filled with different metal powders (the only exceptions were Cu and Pb where copper wires and lead pieces were used instead of powder). The reconstructed horizontal slices for tomography experiments performed at three different neutron wavelengths are shown in Fig 3.24. From the presented reconstructions, one can see that at larger neutron wavelengths (smaller energies) the quality of the reconstructed slices becomes worse. This result was related to the increase of the beam divergence for neutrons with larger wavelength in case of using a neutron guide. On the other side we observed ring artifacts at larger wavelengths only for the channels filled with Ni and Fe powder. One explanation of this observation can be given in terms of total neutron reflection (the same as in a Ni-coated neutron guide) from materials possessing a big neutron scattering length which corresponds to a big critical reflection angle q_c. If we look at Table 3.4 where the scattering lengths and the related critical angles for the materials used in the experiment are presented, one can see that the values for Ni and Fe are the highest. For the materials with smaller or even negative scattering lengths the ring artifacts were not observed in the reconstructed slices, Fig. 3.24. The effect was irrelevant also in case of materials with relatively high scattering length but with inhomogeneous distribution as Pb and Cu. To test this first hypothesis further experiments will be performed at HMI under the supervision of Prof. W. Treimer.

Table 3.4:

Element	Mn	Fe	Mg	Ti	Cu	Cr	Ni	Pb
Scatt. Length, fm	-3.73	9.45	5.37	-3.44	7.72	3.63	10.3	9.40
q_c,deg/Å	-	0.092	0.049	-	0.083	0.056	0.099	0.057

The distortions in the reconstruction due to the presence of strongly absorbing areas in the sample become of great importance at longer neutron wavelengths. It is visible that at wavelength of 9.6 Å the shapes of the highly absorbing materials as Mn, Cu, Ni and Fe are strongly blurred.

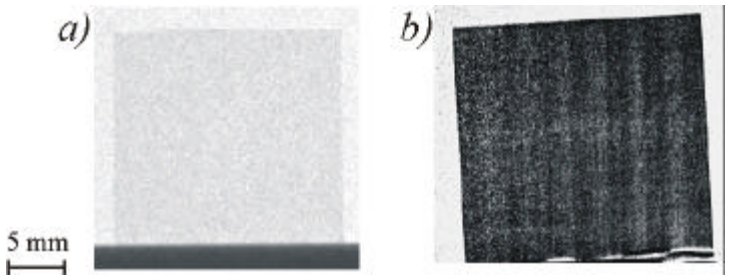

Figure 3.25: Neutron radiography investigation of a 3 mm thick SiC-SiC_f plate using a) thermal neutrons (NEUTRA) and b) ESNR 9.5 Å (PGA).

The energy-selective radiography technique was applied to the investigation of low contrast materials such as SiC-SiC_f - consisting of vertical and horizontal interweaved

SiC fibers. The radiography image taken with thermal neutrons (Fig. 3.25 a) does not provide detailed information about the internal structure of the sample while the picture obtained with the energy-selective neutron radiography (ESNR) at 9.5 Å (Fig. 3.25 b) shows some periodical inhomogenities (vertical and horizontal stripes) in the sample. The improved contrast is due to the increased neutron absorption in Si and C at longer wavelengths.

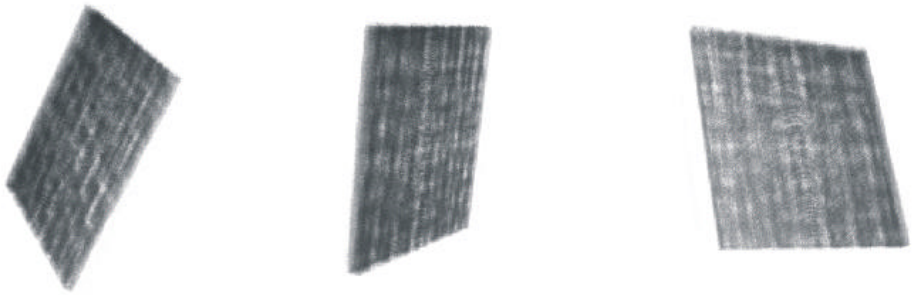

Figure 3.26: Neutron tomography investigation of a SiC-SiC_f plate using a selected neutron wavelength of 7.0 Å.

The tomography investigation performed at neutron wavelength 7.0 Å gives more detailed information about the inner structure of the sample where vertical and horizontal interweaved fibers can be resolved, (Fig. 3.26).

As a consequence of the attractive results provided by the energy-selective cold neutron radiography and tomography technique, projects of developing permanent facilities for such investigations at PSI and FRM II are under study.

The results reported in this chapter are very promising taking into account the perspectives of the energy-selective methods which will be opened with the building of the new generation spallation sources – such as the already planned ESS. In this case neutron pulses with high flux and well defined time-of-flight spectrum in a combination with fast time-gated intensified camera detectors will be available for radiography and tomography purposes. Then all the experiments presented here could be performed with better accuracy and resolution.

Chapter 4: Neutron Topography

4.1 Principle

The topography technique allows the imaging of crystalline materials using the whole beam diffracted by the individual crystallites. That technique was developed first for X-rays and in the middle of 70's the first topography experiments with neutrons were reported [Schl75], [Boe75], [Schl78], [Bar78], [Bar80]. After a long interruption of several decades the neutron topography is again actual. Using the achievements of the neutron imaging technique new topography experiments were performed recently [Wro99], [Wro00]. The possibility of a digital processing of the obtained topography images allows new features in the diffraction experiments as a real time observation of local changes in the crystal state of the sample with the temperature or the pressure, a direct relation between the radiography and topography images, the 3D reconstruction of the diffraction volume with the topo-tomography technique etc. The high penetration capability makes the neutrons especially suited for investigation of bulk samples while X-rays mainly probe regions near the surface. In comparison with the conventional micro beam techniques where only small region of the sample is irradiated, in the topography experiments a large beam in the order of square centimeters is used. To prevent overlapping of the rays diffracted from different areas of the sample, which will cause a loss of spatial information, soller collimators in vertical and horizontal directions can be placed between the sample and the detector [Wro99]. In that case each of the rectangular cells defined by the collimators lamellae will provide a diffracted radiation only from a well-defined sample region onto the corresponding detector element.

The advantage of the topography technique is the exploitation of the scattering information as complete as possible in reasonable time. The main difference from the radiography detection technique is that in case of neutron topography imaging no high brilliance is required but only flux. Therefore the detector system should be optimized for detecting low signals with a resolution no higher than the determined by the soller collimators and the sample to detector distance.

Our aim was to develop a simple topography imaging system based on a position-sensitive digital detector and by simple tests to show that it can be used as an additional feature to every standard two axis neutron diffractometer. The topography method was applied for structure tests of single crystals dedicated for neutron monochromators and a sample preparation where a single crystal was separated from a polycrystalline object.

4.2 Experimental equipment

Two axis neutron diffractometer TOPSI

The collimator/detector arrangement was aligned on the 2θ arm of the two axis diffractometer TOPSI at PSI (SINQ), Switzerland, (Fig. 4.1) [SINQ]. The goniometer head allows to mount the sample for a ω-rotation between 0 and 360^{o} with a step of 0.002^{o} and a tilt movement in interval of (-20 .. 20 deg). The 2θ arm is positioned with the help of air cushions to the defined Bragg-reflection position for the corresponding sample material.

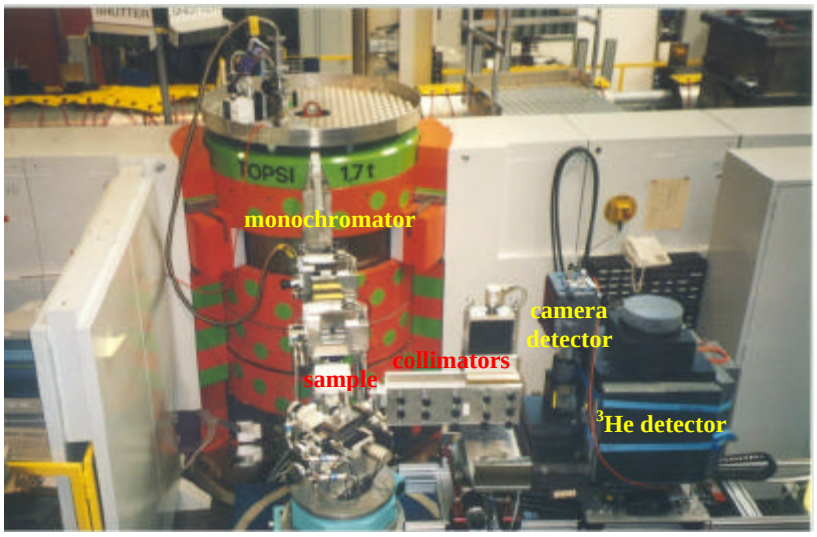

Figure 4.1: A view on the two axis neutron diffractometer TOPSI, PSI, Switzerland, arranged for topography measurements.

For a monochromatization of the primary cold neutron beam a flat (i.e. non-focusing) pyrolytic graphite monochromator was at our disposal. It covered a neutron wavelength interval between 2 Å and 5 Å and provided an almost homogenous beam with an approximate size of 4.0 x 4.0 cm^{2} (Width x Height), (Fig. 4.2).

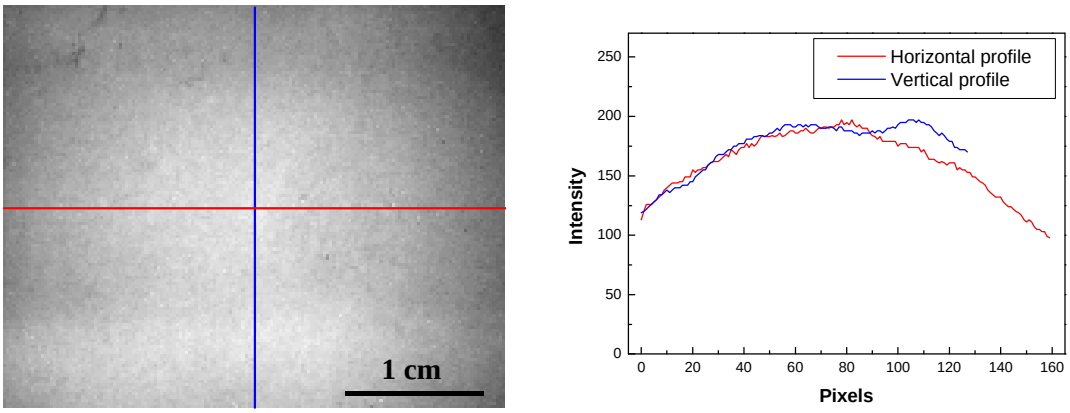

Figure 4.2: The direct beam taken without the collimator arrangement.

A system of three slit diaphragms (two in front and one behind the sample) was used to set the desired beam size. For all topography measurements an opening of the diaphragms of 2.5 x 3.0 cm^2 was applied. The diffractometer is equipped with a ^3He counting tube as a detector. This detector was used in our measurements to set the sample at a reflection position. The 2D camera detector was placed very close in front of the counting detector and the rocking curve measurements were performed through the camera.

Collimator system

The used collimator system in front of the detector consisted of two one-dimensional soller collimators placed one behind the other and rotated under 90^o in such a manner that one of them collimated the diffracted beam in horizontal and the other in vertical direction, (Fig. 4.3).

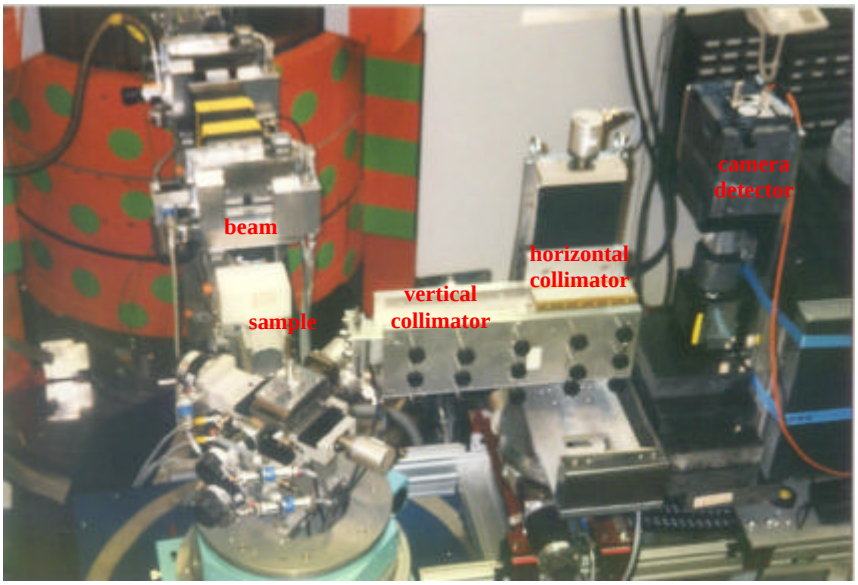

Figure 4.3 A closer view on the collimator system

The collimation parameters and the distance between the sample and the detector determined the spatial resolution of the topography images. For the horizontal resolution a value of 3.1 mm was calculated for a collimator with an angular acceptance of 20' and a length of 20 cm. The vertical spatial resolution was found to be 2.3 mm for a collimator with an angular acceptance of 15' and a length of 33 cm. The distances between the sample, collimators and the detector are shown in Fig. 4.4.

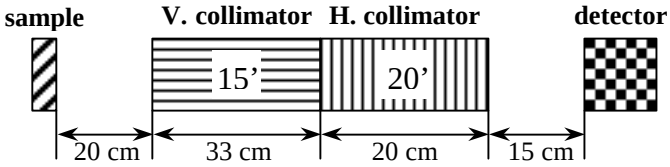

Figure 4.4: Geometrical parameters of the collimator system

The collimation system also determines the detection resolution of the crystal disorientation in the sample (the crystal mosaic). If two of the crystallites in the sample are disorientated at a small angle α with respect each to other, (see Fig 4.5), then the diffracted beam will have a divergence defined by the same angle α. Taking into account the angular acceptance β of the collimators in front of the detector one can see that only neutrons with a divergence angle smaller than β will be transmitted through the collimator. Therefore the angular resolution of the crystalline orientation was 20' in horizontal and 15' in vertical direction.

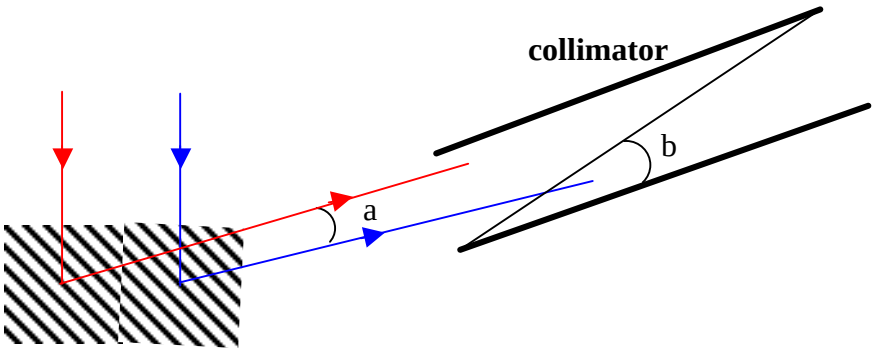

Figure 4.5: Bragg-reflection from two crystallites disorientated on a small angle α.

Detector setup

Of course the beam collimation decreases the diffracted neutron intensity a lot. For this reason the acquisition system was especially designed and optimized for weak signal measurements. The used position sensitive detector was based on a conventional CCD radiography system. The visible light emitted from the ^{6}LiF/ZnS(Ag) scintillator was imaged with an optical lens onto a Peltier-cooled CCD camera through a mirror at a 45

degree angle. The CCD-sensor had 1280x1024 pixels (6.7 μm square pixels) with a dynamic range of 12 bits (4096 gray levels per pixel). The optical configuration resulted in a field of view of 3.6 x 2.9 cm^2 (W x H), which gives a projection ratio of 35 pixels/1 mm. The data stream was transferred via a fiber optic cable connecting camera and PCI-Interface-Board. Software for controlling the camera settings, displaying and storing the images was developed on Labview©. The detection system has been described in more detail elsewhere [Bae02].

As it can be seen in Fig. 4.6 the camera box was placed under the direct influence of the external light in the experimental hall. To prevent the contributions of the surrounding light special precautions were taken for light tightness of the whole detection setup.

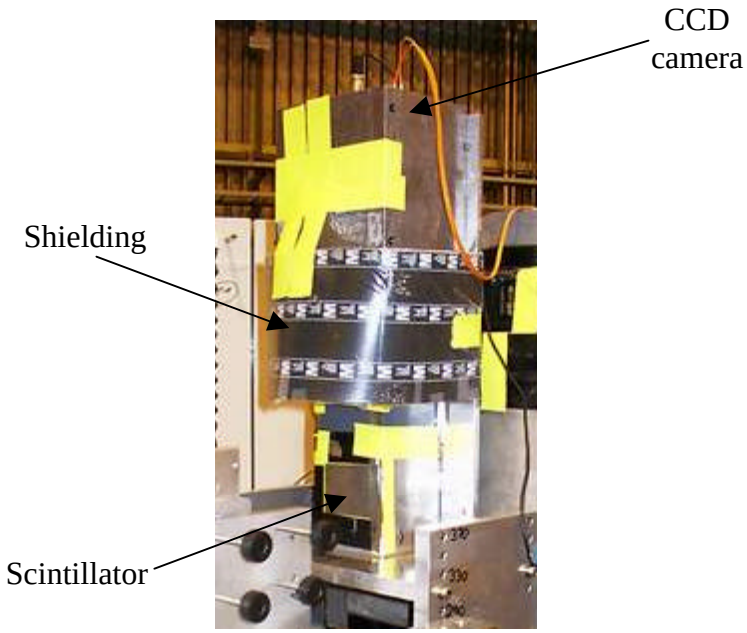

Figure 4.6: The used position-sensitive detector, based on a conventional CCD neutron radiography system.

The detector was also shielded with borated plates against the scattered thermal neutrons and with lead bricks against the produced secondary gammas. In spite of that a lot of white spots in the topography images were observed due to the large exposure time of some minutes. To prevent this the measuring time was subdivided into short intervals as for each of them an image (called projection) was taken. The other reason for using many images was that because of the camera controller it was not possible to stop the acquisition without losing the image. Therefore we divided the acquisition in smaller parts, and when we had to stop, we only lost the last image. The obtained set of images was post-processed in a way that every image was corrected with a median filter against white spots and the corresponding dark current was subtracted. The so corrected projection images were summed up in one final topography image, Fig. 4.7 which was used later for further analysis.

To reduce the measuring time and to improve the image statistics different binning ratios were tried. The binning option was implemented in the acquisition software and it was used very intensively. As it was calculated above the determined spatial resolution with the help of the soller collimators is in the order of 2 mm while the camera projection ratio is 35 pixels/1 mm at binning one. Therefore even 8x8 binning with a projection ratio of 4 pixels/1 mm was used without any loss of a spatial resolution.

Another disadvantage of the large exposure times especially at neutron spallation sources are the fluctuations of the beam intensity with time. Since the topography images can not be normalized with a flat-field image as in the conventional radiography, the total initial neutron flux was kept constant for each topography measurement.

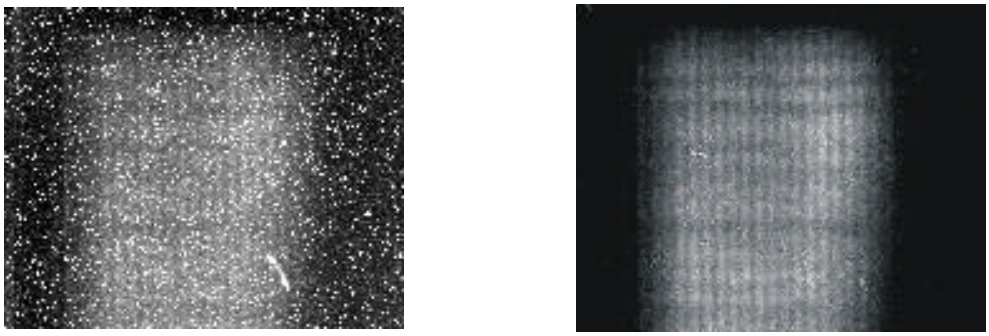

Figure 4.7 At a defined reflection position a number of projection images were taken (left). The final topography image (right) was obtained as a summation of the corresponding projection images after their correction for white spots and dark current.

This was realized with a control neutron monitor placed in front of the sample, between the first and the second diaphragm. The signal from the monitor was proportional to the transmitted neutron flux so its output was connected as a feedback to the acquisition system. The projection images were collected in short time intervals at the same reflection conditions until a defined value of the control monitor was reached. The time intervals were set in the way that for each reflection position of the sample more than 5 images were collected. In this way for each reflection position a constant primary neutron flux was used, while the diffracted intensity was distributed among a number of projection images. The projection images were used later for a post-procession procedure as described above. This allowed us to compare images taken under different reflection conditions and from various samples.

4.3 Experiment

The topography measurements were performed in the following sequence.

- First the 2θ angle was calculated for a Bragg reflection hkl with interplanar spacing d_{hkl} using the Bragg relation:

$$2d_{hkl}\sin\theta = \lambda,$$

  where θ is the reflection angle and λ is the neutron wavelength.

- The 2θ arm of the diffractometer was set at the calculated value for 2θ and a diffraction spectrum was measured with the ^{3}He detector rotating the sample in angular interval $\omega = 0 .. 180^o$ at maximally opened diaphragms (beam size 2.5 x 3.0 cm^2) without to put the collimators into the diffracted beam.
- The angle positions at which intensive peaks in the diffraction spectra were observed were recorded. After that the sample was positioned at one of the most intensive reflection positions.
- If no intensive reflections were found the sample was tilted at various angles and new rocking curves ($\omega = 0 .. 180^o$) were measured until some reflection was detected.
- At the chosen reflection position a precision adjustment of the 2θ and ω angles was performed in order to increase the signal in the ^{3}He detector. After that the collimators were lifted with the help of a lifting system and a refinement of their alignment with respect to the diffracted beam was performed by rotating them with a fine step width around the zero position.
- At the so adjusted setup topography images were collected using acquisition software developed on LabView©.

The results from a topography investigation of Heusler crystals Cu_2MnAl with d_{111}=3.53 Å intended for neutron monochromators are shown in Fig. 4.8. For the 2θ angle a value of 84.35^o was calculated at the used neutron wavelength of 4.74 Å. The measuring time for one topography image at a constant neutron flux and 8x8 binning was approximately 360 s as every 60 s a single image was collected. So every topography image was obtained after processing of 6 projection images under the same reflection conditions. The observed stripe structure in the topography images is related to the presence of the soller collimators in the beam. The measured diffraction spectra are shown together with the topography images.

Obviously the topography investigation gives an additional spatial information about the crystalline orientation in the sample. An example of a well-orientated single crystal is presented in Fig. 4.8 a. In a small angular interval of $\Delta\omega = \pm 0.2^o$ around the maximum intensity of $\omega = 42.7^o$ the whole sample volume gives a contribution to the

Bragg reflection intensity. The shown integral diffraction spectrum over the whole sample agrees in an excellent way with the topography imaging.

Opposite to that case a topography investigation of a crystal with a mosaic structure is presented in Fig. 4.8 b. To obtain a maximal intensity of the diffracted beam the crystal was tilted at $\varphi = -1.8^{o}$. Clearly two complimentary reflecting regions can be recognized on the images at $\omega = 43.0^{o}$ and $\omega = 43.5^{o}$. The transition between them is smooth as it can also be seen from the diffraction spectrum. An example of an abrupt transition between two crystallites (domains) disorientated by $\Delta\omega \sim 1^{o}$ is shown in Fig. 4.8 c. The areas corresponding to the two domains can be located easily on the topography images taken at $\omega = 42.8^{o}$ and $\omega = 43.7^{o}$. The agreement with the diffraction spectrum is again excellent.

Figure 4.8 a:
TOPSI Diffractometer, PSI
λ = 4.74 Å
Sample: Cu_2MnAl Single Crystal
Date: 27.06.2001

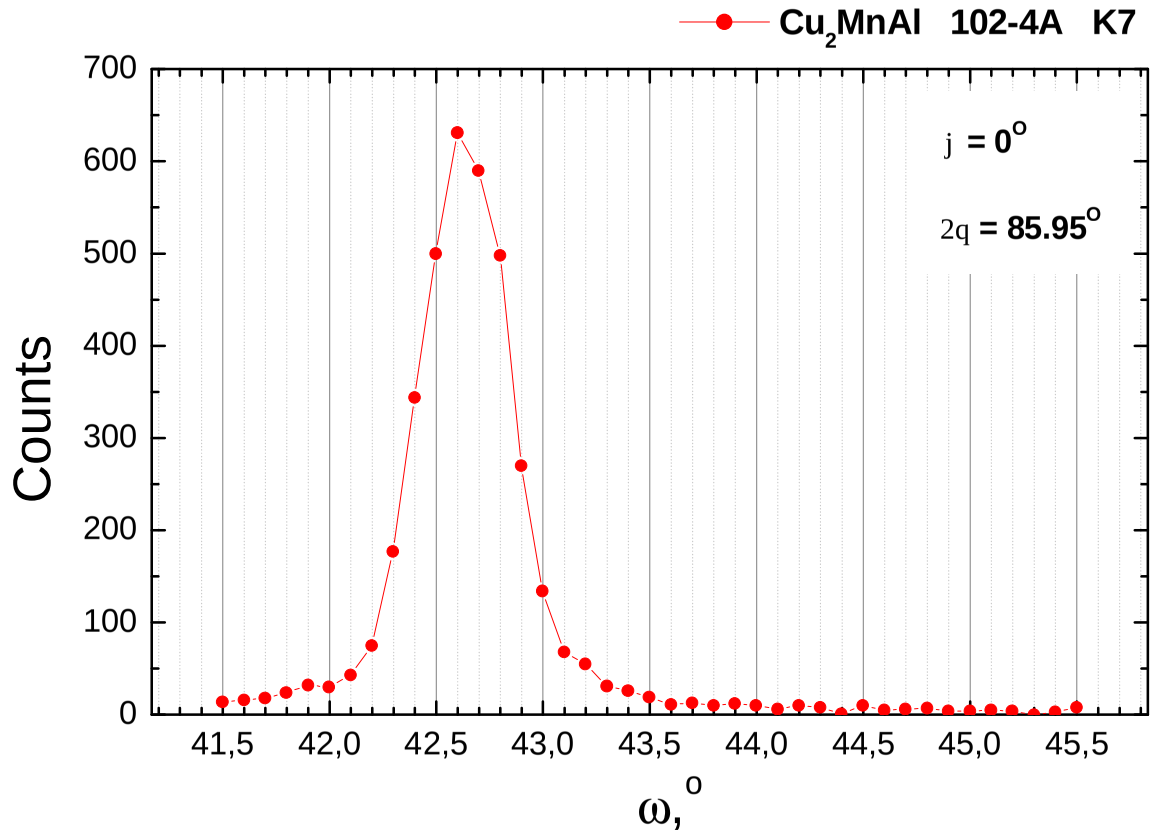

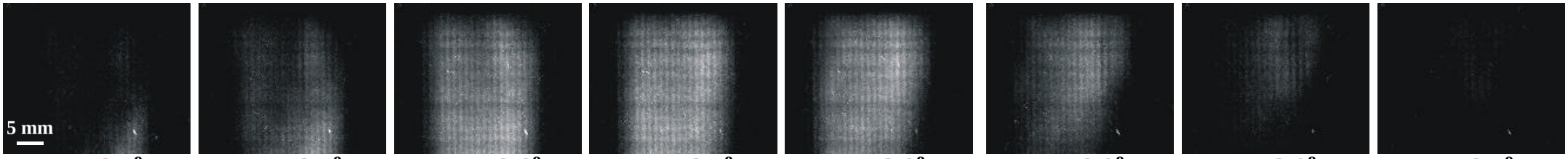

Figure 4.8 b:
TOPSI Diffractometer, PSI
λ = 4.74 Å
Sample: Cu_2MnAl Crystal with mosaicity
Date: 27.06.2001

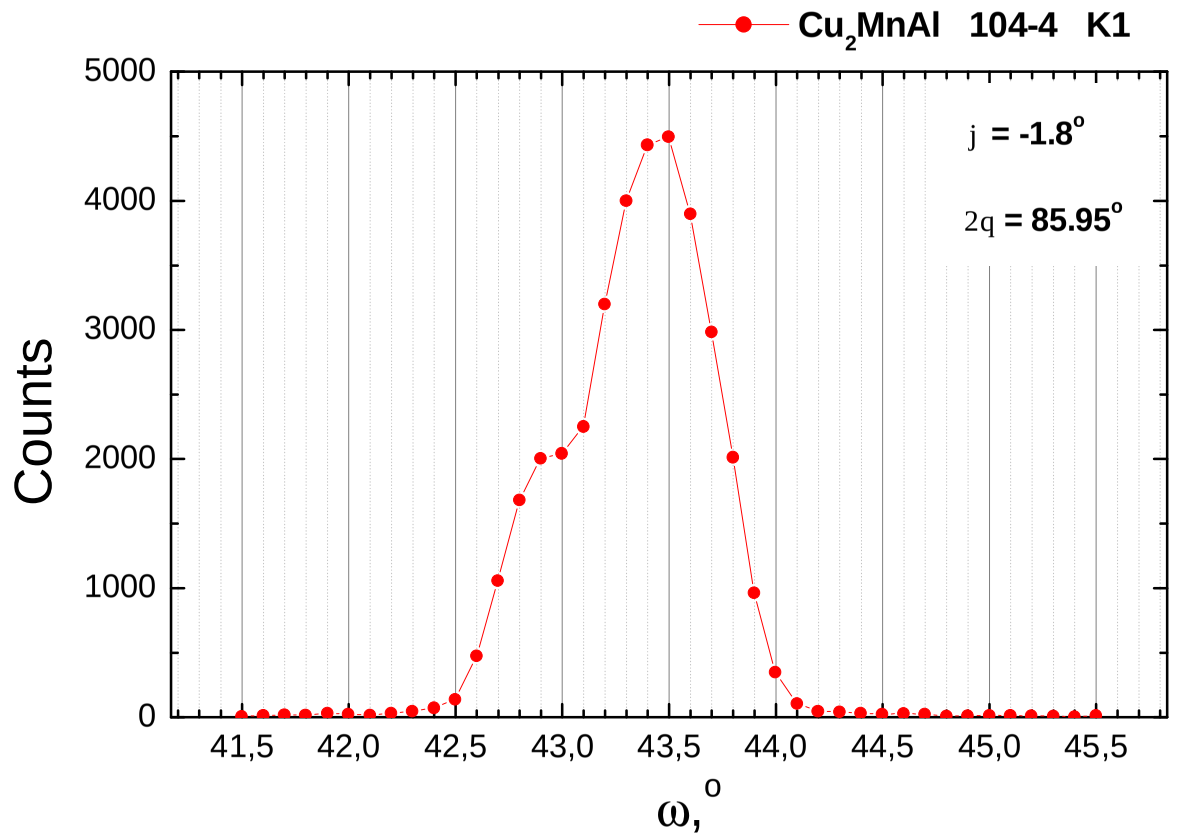

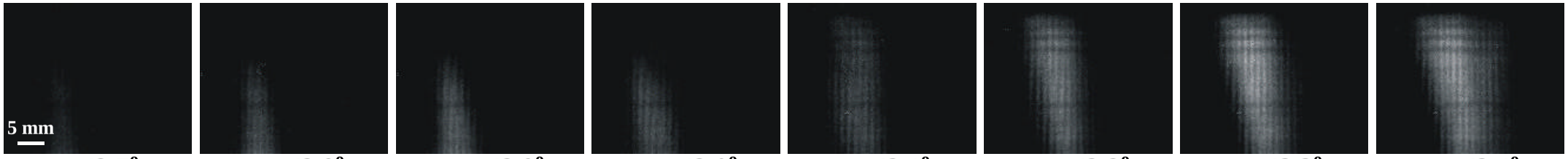

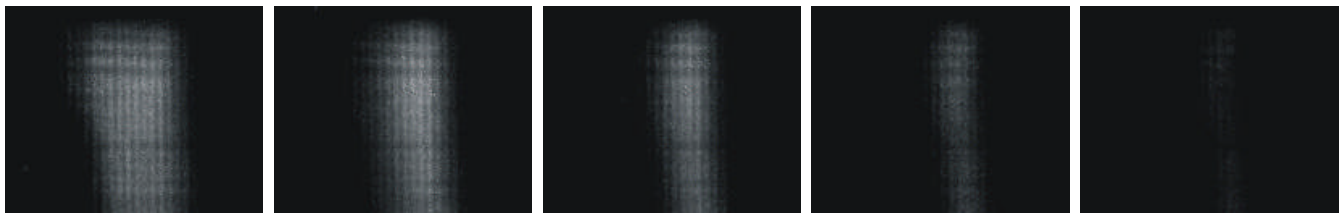

Figure 4.8 c:
TOPSI Diffractometer, PSI
λ = 4.74 Å
Sample: Cu_2MnAl Crystal with two domains
Date: 26.06.2001

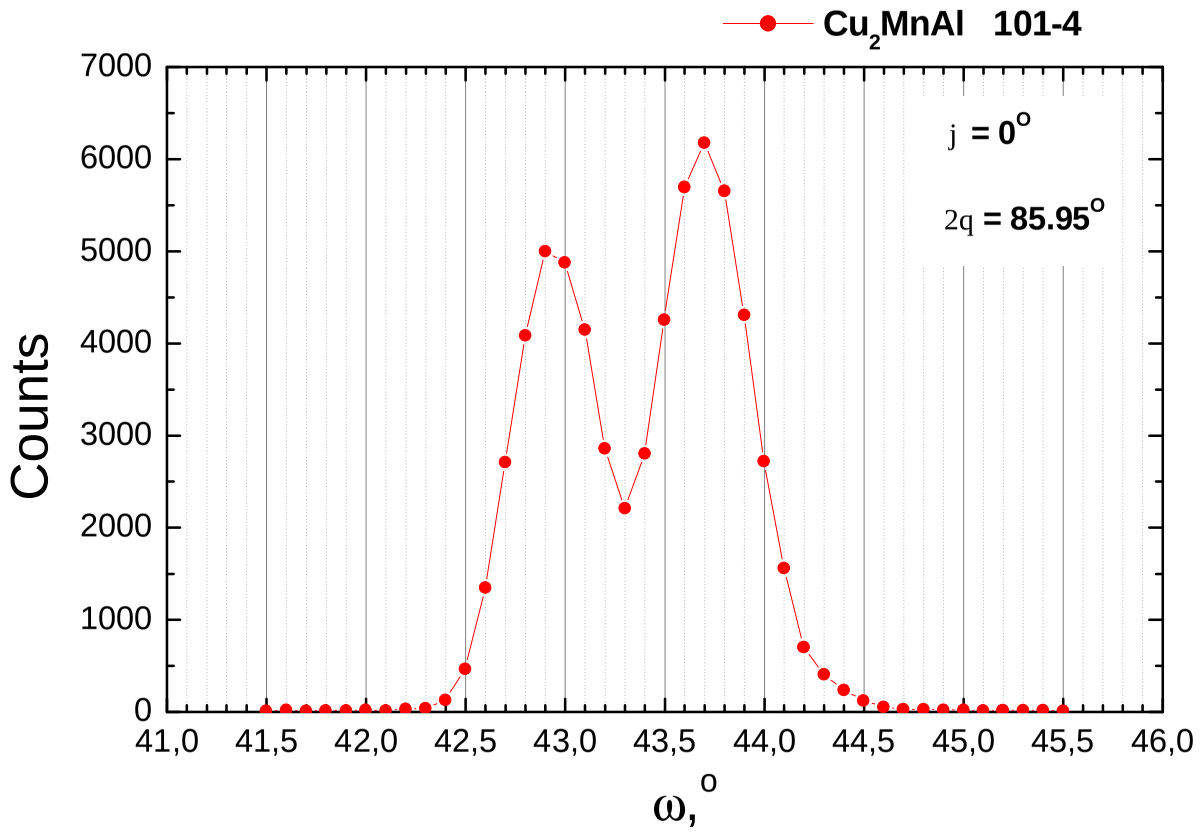

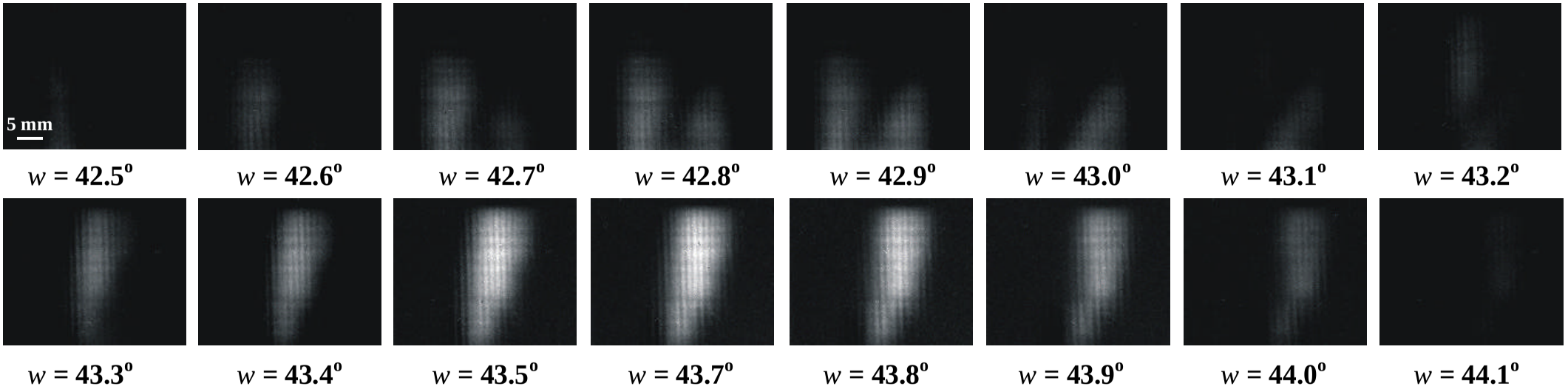

To test the contribution of the collimating system to the quality of the topography images, experiments with and without the soller collimators in the diffracted beam were performed. The results from such a topography investigation of a single crystal are presented in Fig. 4.9. The data represent the crystalline homogeneity of a 220-oriented Cu single crystal plate (3 x 5 cm^2). The measuring time was 1 h per topography image as every 5 minutes a projection image was recorded.

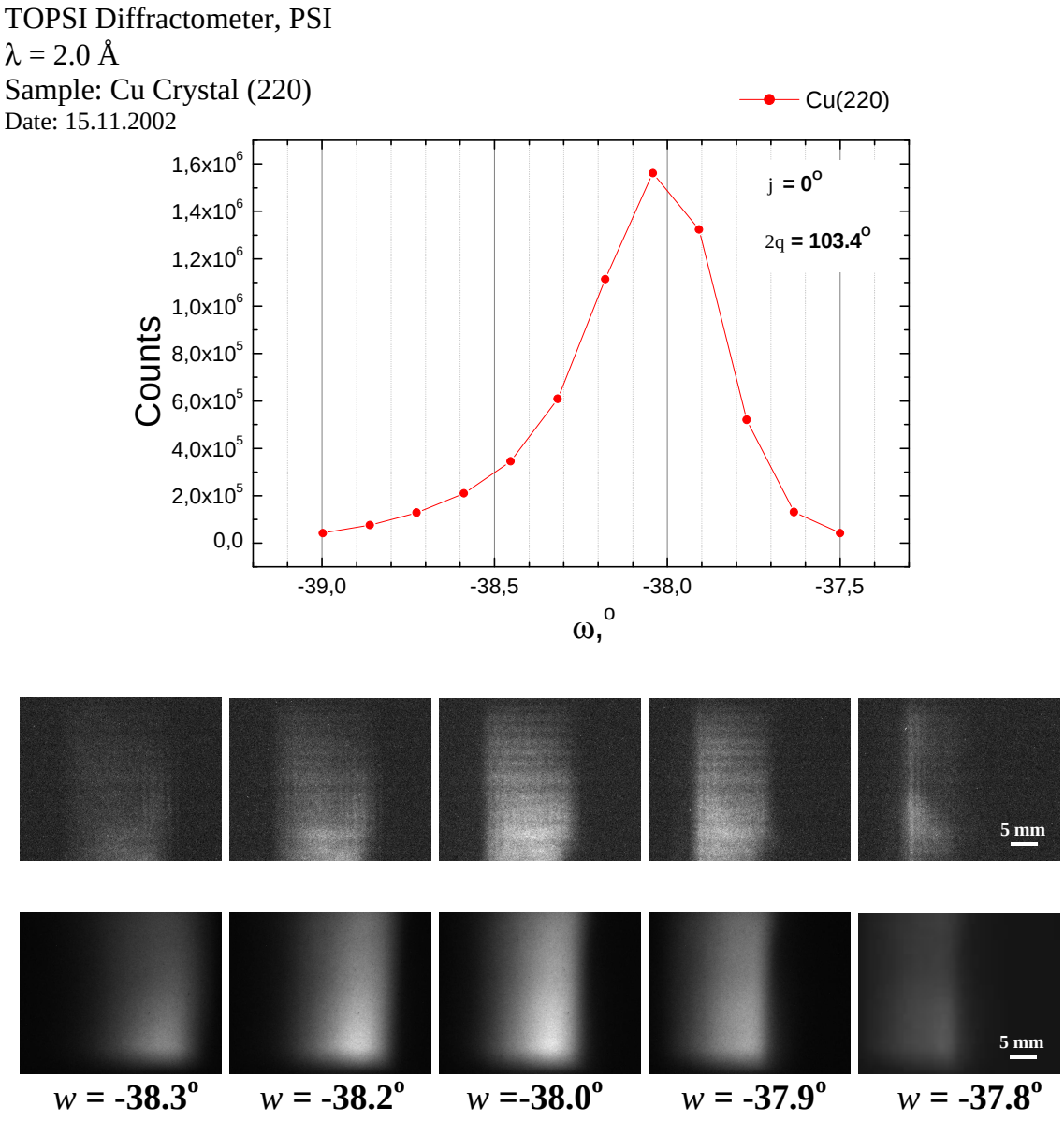

Figure 4.9: A topography investigation of a Cu (220) monocrystal plate with (above) and without (below) the use of the soller collimators.

The obtained topography images show a good agreement with the shown diffraction spectrum. Obviously the collimating system considerably improves the angular resolution eliminating the overlapping of rays diffracted from different regions. The

images taken without any collimation are blurred and they could provide only qualitative information about the crystalline orientation in the sample. The information which can be extracted from them is the size and the integral intensity of the reflecting area at defined reflection conditions. Unfortunately the intensity distribution differs strongly in the cases with and without collimators. Therefore some detailed analysis considering the exact visualization of the crystalline disorientation as shown in Fig. 4.8 is not possible. So the "divergent" topography imaging can be used for a qualitative estimation of the presence of different crystalline orientations in the sample and for a raw localization of these areas.

This technique was used in the case of topography imaging of polycrystalline samples where the diffracted intensity is strongly reduced because of the used soller collimators. Therefore for polycrystalline measurements the collimators were removed from the beam to increase the intensity and the camera detector was moved as close to the sample as possible in order to reduce the spatial blurring due to the overlapping reflections from different sample areas. The only information which can be obtained, as shown above, is what part of the sample reflects at defined conditions and what is the predominant orientation of the crystallites.

The investigated sample was a MnSi polycrystal (Fig. 4.10) and the task was to locate the sample regions possessing 111 orientation (d_{111} = 2.63 Å). For that purpose the arm of the diffractometer was positioned at a 2θ angle of 55.2°, calculated for a neutron wavelength of λ = 2.44 Å and rocking curve measurements were performed. The obtained diffraction spectra show a sharp peak at ω = 70.05°, which can also be observed after tilting the sample at φ = -5° (Fig. 4.11).

Figure 4.10: The used MnSi polycrystal in the topography experiment. The investigated area is marked in the photo.

In spite of the almost equal diffraction spectra, shown in Fig. 4.11, the performed topography investigation provides completely different images for the two reflection positions of the sample. Two reflecting sample regions can be recognized in the shown

images. The reflection contribution in the picture taken at $\varphi = 0^o$ is from a homogeneous area while in the other one obtained at $\varphi = -5^o$ an inhomogeneous spatial distribution in the reflecting region can be observed.

At the end an attempt to align the real photo of the sample with the obtained topography images is shown in Fig. 4.12. The position of the investigated sample area was located by placing an absorber marker at a direct observation of the crystal with the camera detector at $2\theta = 0^o$.

TOPSI Diffractometer, PSI, Date: 16.06.2002

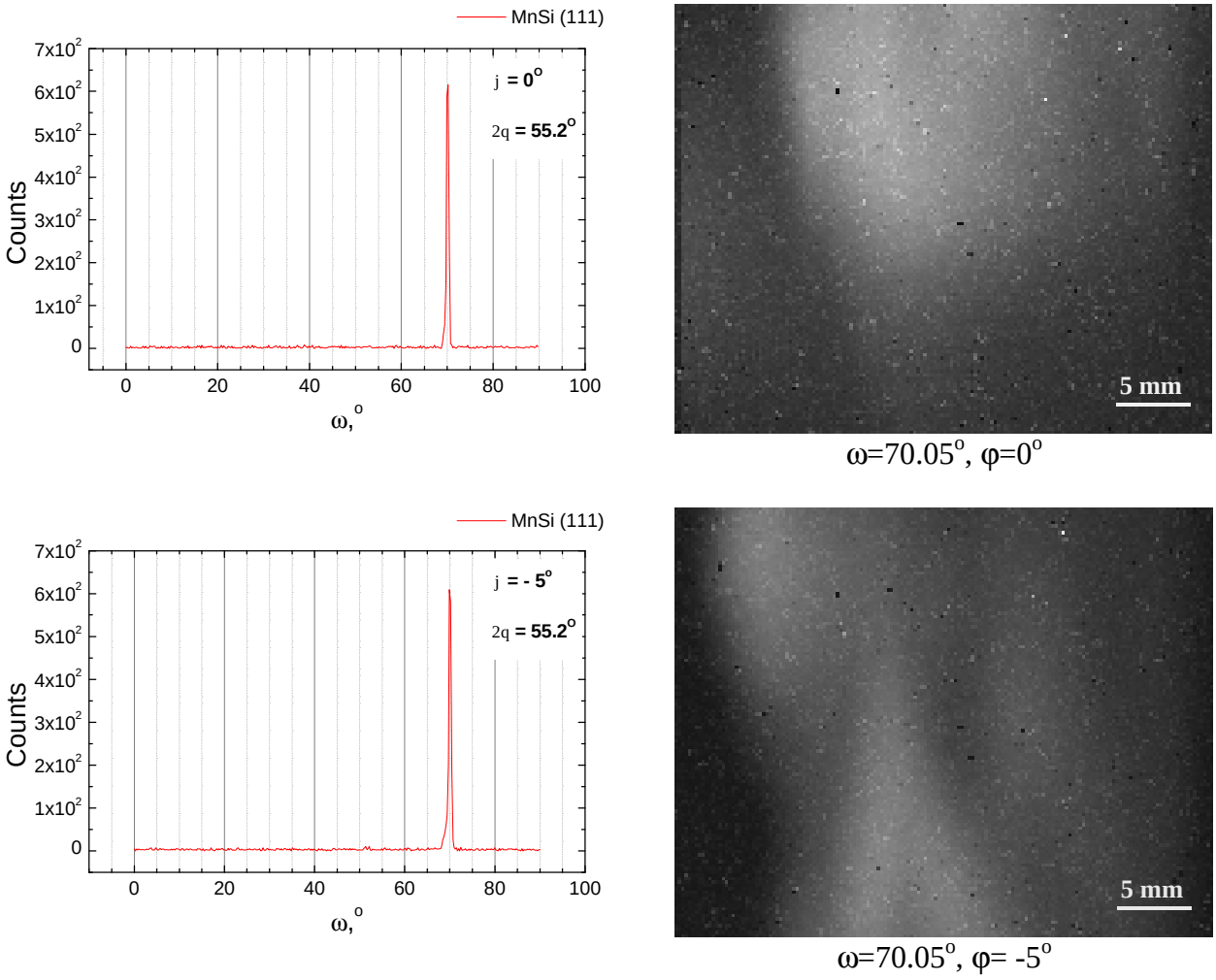

Figure 4.11: The obtained topography images from the MnSi polycrystal at a distance of ~ 20 cm between the sample and the detector and measuring time of 1 h at image 8x8 binning. The measured detailed diffraction spectra are shown on the left hand side.

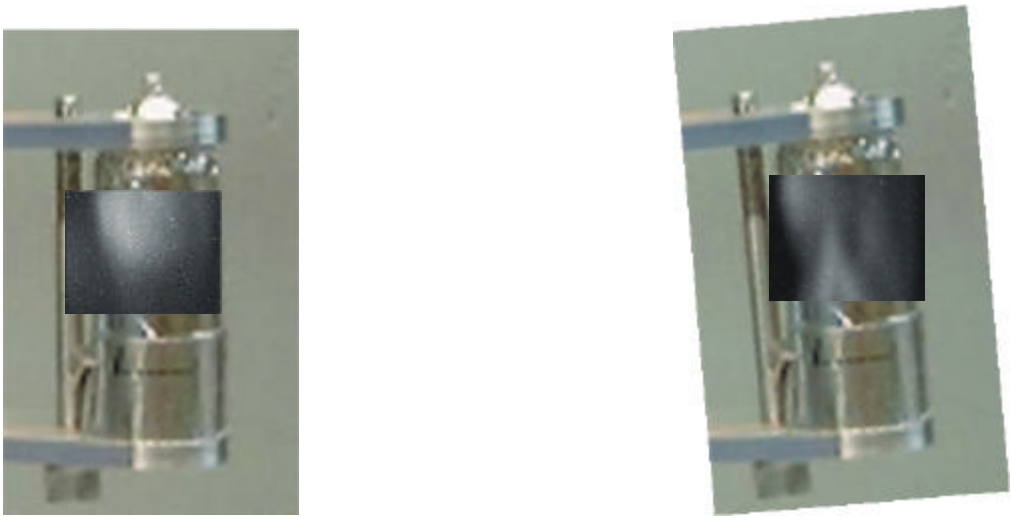

Figure 4.12: Representation of the alignment of a real photo of the sample with the obtained topography images at two reflection positions.

Chapter 5: Monte Carlo Simulations

5.1 Introduction

Monte Carlo (MC) methods are stochastic techniques based on the use of random numbers and probability statistics to investigate problems. These methods can be used for description of statistical processes (such as nuclear interactions) and for solving of complex problems that cannot be modelled by deterministic methods. Solving equations which describe the interactions between two atoms is fairly simple, but solving the same equations for hundreds of atoms is impossible. With MC methods, a large system can be sampled in a number of random configurations, and the data can be used to describe the system as a whole. The simulations are performed on a computer because the number of trials necessary to adequately describe the system is usually quite large. The separate probabilistic events that compose the process are simulated sequentially. The statistical sampling process is based on the selection of random numbers – analogous to throwing dice in a gambling casino – hence the name "Monte Carlo". Since the results achieved by MC in particle transport are realistic (a theoretical experiment), MC is well suited to solving complicated three-dimensional time-dependent problems. The theoretical experiment consists of actually following each of many particles from a source throughout its lifetime within the experiment until some interaction occurs. Probability distributions are randomly sampled using transport data to determine the outcome at each step of its life.

In Fig. 5.1 the random history of a neutron incident on a slab of a defined material can be seen. Numbers between 0 and 5 are selected to determine what and where interaction takes place. The choice what interaction to be taken into account is based on the physics and probabilities determined from the simulated processes and involved materials. In this particular example, a neutron collision occurs at event 1. The neutron is scattered in the direction shown, which is selected randomly from the physical scattering distribution. A photon is also produced and is temporarily stored, or banked, for later analysis. The neutron is retrieved and, by random sampling, undergoes second scattering without producing photons at event 2 and after that leaks out of the slab at

event 3. The remaining photon generated at event 1 is now followed with a scattering at event 4 and a capture at event 5.

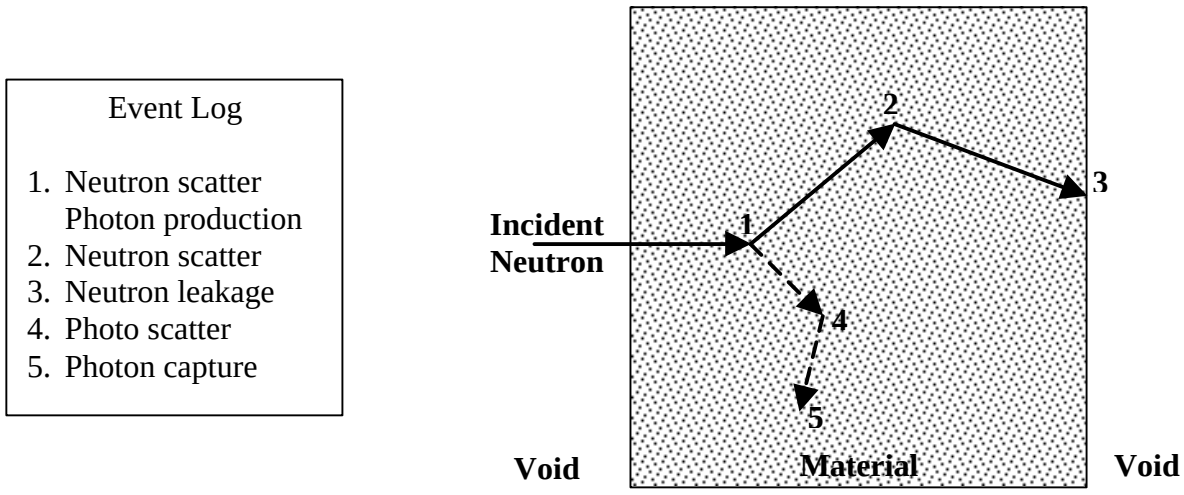

Figure 5.1: Schematic representation of the Monte Carlo method

Now the neutron history is complete. If more and more such histories are followed, the neutron and photon distributions will be obtained with a better precision. The quantities of interest requested by the user are tallied, together with estimates of the statistical uncertainty of the results.

5.2 MCNP Code

As described in the MCNP-4B manual [Bri96]:

"MCNP is a general-purpose, continuous-energy, generalized-geometry, time-dependent, coupled neutron/photon/electron Monte Carlo transport code. It can be used in several transport modes: neutron only, photon only, electron only, combined neutron/photon transport where the photons are produced by neutron interactions, neutron/photon/electron, photon/electron or electron/photon. The neutron energy regime is from 10^{-11} MeV to 20 MeV and the photon and electron energy regimes are from 1 keV to 1000 MeV."

The input information for the simulation is saved in an input file created by the user. This file has a fixed structure and it contains information about the problem as:

The geometry specification,
The description of materials and selection of cross-section evaluations,

The location and characteristics of the neutron, photon, or electron source,

The type of answers or tallies desired, and

Any variance reduction techniques used to improve efficiency.

MCNP uses continuous-energy nuclear and atomic data libraries. Over 500 interaction tables are available for approximately 100 different isotopes and elements. Multiple tables for a single isotope are provided because of different data evaluations, different temperature regimes and different processing tolerances. Neutron-induced photon production data are given as part of the neutron interaction tables when such data are included in the evaluations.

Cross sections for nearly 2000 dosimetry or activation reactions involving over 400 target nuclei in ground and excited states are also part of the MCNP data package.

5.3 MCNP simulation of radiography experiments

The possibility to use different transport modes and to simulate cascade processes as the neutron-induced electron and photon production make the MCNP code suitable for the optimisation and design of shielding barriers. The option to include fusible materials in the simulated system allows simulations of various critical assemblies. These and many other features make MCNP code very powerful tool for simulation and optimisation tasks in the nuclear science and engineering.

The application of the MCNP code for a simulation of neutron radiography experiments is trivial because all the required elements from the classical radiography alignment (source-object-detector) are build in the software as standard functions.

Let us fix our attention on the main parameters describing one MCNP radiography simulation.

Geometry specification.

The distance between the source and the sample can be as small as possible in order to reduce the calculation time, which is proportional to the simulated volume. Instead of describing the whole collimation system (flight tube, diaphragms, etc.), a source plane emitting neutrons with a divergence distribution defined in the reality by the collimator was placed in front of the sample.

The sample to detector distance was the same as in the real experiment due to the strong dependence of the scattering contribution and the image sharpness on this parameter.

The source.

The neutron source was characterized by its spectrum, neutron divergence and size. MCNP code allows to specify the energy distribution of the emitted particles by a discrete table (experimental data) or by analytical expression (Maxwell spectrum, etc.).

In our simulations a discrete definition of the neutron spectrum was applied. For this purpose experimental data from a time-of-flight measurement of the neutron spectrum at the radiography station NEUTRA at PSI, Switzerland were used. The energy interval was specified between 8 meV and 1eV.

The beam divergence was determined by the collimation ratio *L/D* of the corresponding radiography facility as $\mathrm{tg}\alpha_{\mathrm{div}}=1/(L/D)$. For example at a collimation ratio of *L/D* = 500 (NEUTRA) the calculated value for the divergence angle α_{div} is 0.1^{o}.

The size of the source plane was defined to be no more than two times larger than the sample in order to save calculation time.

Detector

The 2D sensitive detector surface was described with the help of the so-called lattice structure available in MCNP. For each cell of this structure a corresponding tally was connected. In this way the averaged neutron flux through each defined cell volume was recorded in an output file.

The pixel size was determined by the desired spatial resolution. There is no software restriction for the number of cells and the size of the lattice, but a compromise is necessary to be done due to the considerable increase of the calculation time with the increase of the number of the sampled volumes. The maximum used resolution in our simulations was 0.2 x 0.2 mm^2.

MCNP gives the possibility to set a detection reaction for the defined detector cells (pixels). Two reactions which are very important for the radiography detection systems are used in the simulations. These are the (n,γ) reaction in Gd_2O_3 which corresponds to a neutron detection with imaging plates and the (n,α) reaction in ^{6}Li related to the ZnSLiF scintillators used in radiography CCD camera setups. The corresponding thickness of the used in MCNP detector plates were in agreement with the real converter layers (200 μm in case of IP and 300 μm in case of ZnSLiF scintillator). For the comparison of the simulated with the experimental radiography images a normalisation of the neutron flux for each cell to the flux without sample in the beam was carried out.

Two examples of MCNP neutron radiography simulations are shown in Fig. 5.2. The investigated sample (an iron step wedge) is the same in both simulations, but the beam divergence is different. The first simulation is performed with a parallel beam and the second with a divergent beam possessing a divergence angle of 5^{o}. Obviously the image obtained with the parallel neutron beam is much sharper than the other at the divergent beam.

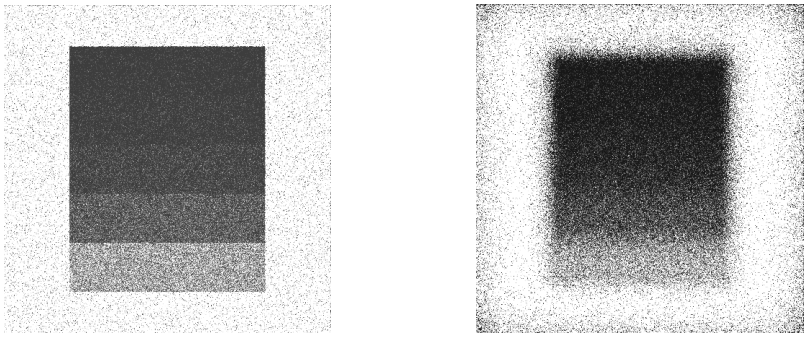

Figure 5.2: MCNP simulation of neutron radiography of an iron step wedge at a distance of 5 cm from the detector for two different beam divergences of $\alpha_{div} = 0^o$ (left) and of $\alpha_{div} = 5^o$ (right).

Quantitative investigations were also possible with MCNP simulations. The good agreement between simulated and experimental data is shown in Fig. 5.3. The aim of the performed simulation was to investigate the contribution of scattered neutrons in a radiography experiment with a highly scattering sample (water step wedge) at different distances to the detector. In the simulated detector pixels a separation of the neutrons being scattered in the sample from all the neutrons reached the corresponding pixel was used. Furthermore the effect of multiple scattering was also estimated separating the fraction of neutrons scattered more than 1 time in the sample. The calculated neutron scattering distributions at the two distances from the detector of 5 and 10 cm are shown together with the transmission profiles in Fig. 5.3.

The distribution of the scattered and particularly multiple scattered neutrons in the case of the shorter distance between the sample and the detector of 5 cm shows a maximum which corresponds to a water thickness of approximately 3.5 mm. This maximum can be explained with the mean-free-path for thermal neutrons in water provided as an additional information in the MCNP output file. For the used thermal spectrum of SINQ at PSI the corresponding mean-free-path in water was calculated to be 2.7 mm. Beyond this thickness the transmitted neutrons should underwent already one or more scattering events. The decrease of the signal from scattering and multiple scattering neutrons at larger thickness is a combination of the border effect (due to the lack of a scattering contribution outer the sample borders) and the neutron absorption which increases with the water thickness.

In the next chapters the following topics will be presented: an estimation and corrections of the scattering contribution in the neutron radiography imaging, an explanation for the thickness dependent attenuation coefficient in case of neutron transmission through strong absorbers (borated steels) and design and optimisation of a mobile neutron source.

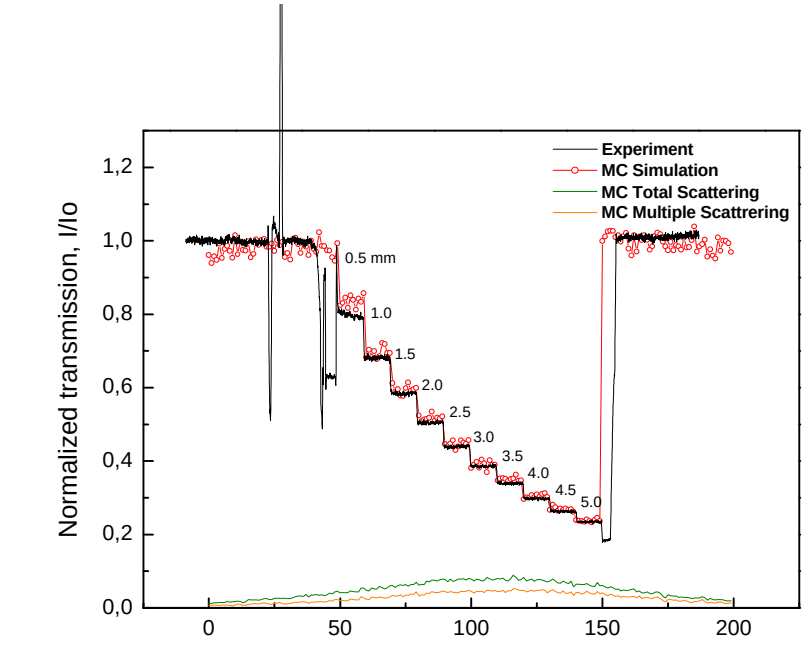

Water Step Wedge
at a distance 5 cm from the detector

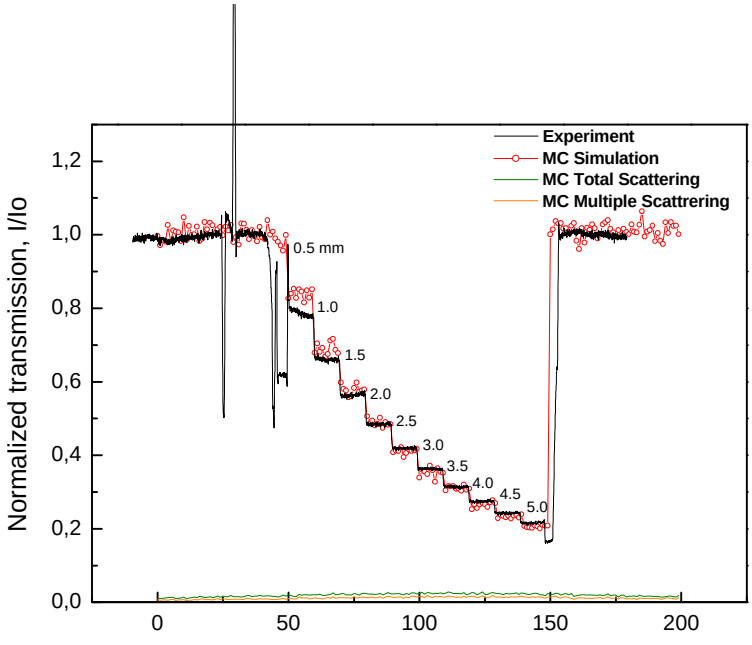

Water Step Wedge
at a distance 10 cm from the detector

Figure 5.3: Comparison between experimental and simulated data for neutron radiography of a water step wedge at two different distances between the sample and detector of 5 cm (above) and of 10 cm (below). Additionally the scattering and multiple scattering contributions were calculated for the two cases.

Chapter 6: Investigation and Correction of the Contribution of Scattered Neutrons

6.1 Introduction

The quantitative neutron radiography requires an exact relation between the measured neutron attenuation and the real macroscopic attenuation coefficient for every point of the sample. In this way quantitative information about the material composition or the sample thickness can be obtained. The assumption used in these cases that the attenuation of the neutron beam through the sample is exponential: $I/I_0=\exp(-Sd)$ is valid only when the contribution of some secondary effects as the neutron scattering, the beam hardening (for more details see § 7.3) or the background is negligible. Because of the high scattering cross-sections of hydrogen (σ_s=80.26 b) for thermal neutrons, the problem with the scattered neutrons at quantitative radiography investigations of hydrogenous materials (as PE, PMMA, Oil, H_2O, D_2O etc) is not trivial. For these strong scattering materials the neutron beam attenuation is no longer exponential and a dependence of the macroscopic attenuation coefficient on the material thickness and on the distance between the sample and the detector appears [Leh02]. In these cases some correction procedures are required to obtain a reliable quantitative analysis.

A lot of experimental methods for corrections of the scattering blur in radiography pictures have been developed [Une98], [Ike96], [Oda96]. All of them use the fact that a great part of the neutrons are scattered in the sample under different angles and their trajectories after that are not parallel to the beam axis. Because of that different honeycombs or absorbing stripes are used to reduce and to estimate the scattering beam component. The drawback of these methods is that the effects due to multiple scattering cannot be eliminated completely. Some theoretical considerations of the scattering problem give also good results in order to reduce the scattering contribution [Une98a]. The basic theory of the image formation in neutron radiography is well presented in [Har86] where the image blurring is described in terms of Point Spread Functions. Further development of the idea of a PSF superposition was done with the so-called

Signal Transfer Analysis reported by H. Pleinert et al [Ple99]. In this analysis Monte Carlo simulations were used to obtain the corresponding PSF and a consequent try to reconstruct the uncollided beam component by a recursive algorithm was performed. The reverse task – the determination of the PSF using a MCNP simulation of the radiography experiment was solved in [Mor92]. The PSF obtained in this way was used for further corrections by a deconvolution procedure for radiography images.

Our attempts were to extend these previous studies to a wider range of applications in radiography picture analysis where full simulation of real neutron radiography experiments can be achieved and consequently a procedure for image corrections due to scattered neutrons can be developed.

6.2 Dependence of the scattering distribution on the sample and the distance to detector

The signal obtained in the radiography measurement can be regarded as a result of superposition of two different mechanisms of interaction between the neutrons and the investigated sample. The neutron flux after the interaction can be divided into the following components: the *collided* flux – the component of neutrons that reach the detector after being scattered in the sample and the *uncollided* flux – the component of neutrons that penetrate the sample without interacting with it. A graphic representation of this model for a parallel neutron beam is shown in Fig.6.1.

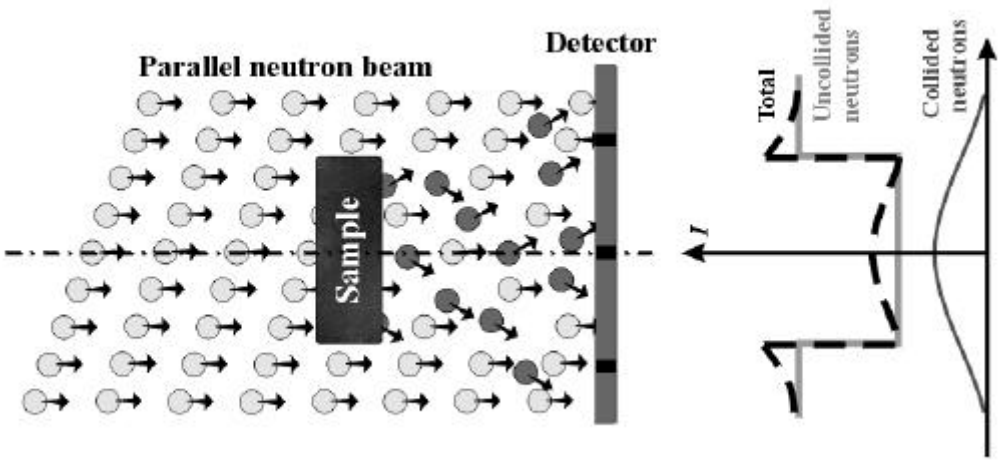

Figure 6.1: A schematic representation of the image formation process

It can be demonstrated that the scattering contribution depends on the distance between the sample and the detector. This dependence is clearly illustrated in Fig. 6.2 where a radiography investigation of PMMA slabs (1 x 5 cm) with different thicknesses was performed at two distances to the detector. The experiment was performed at the

thermal radiography setup NEUTRA at SINQ, PSI. The detector system was a standard CCD camera system described elsewhere [Leh99].

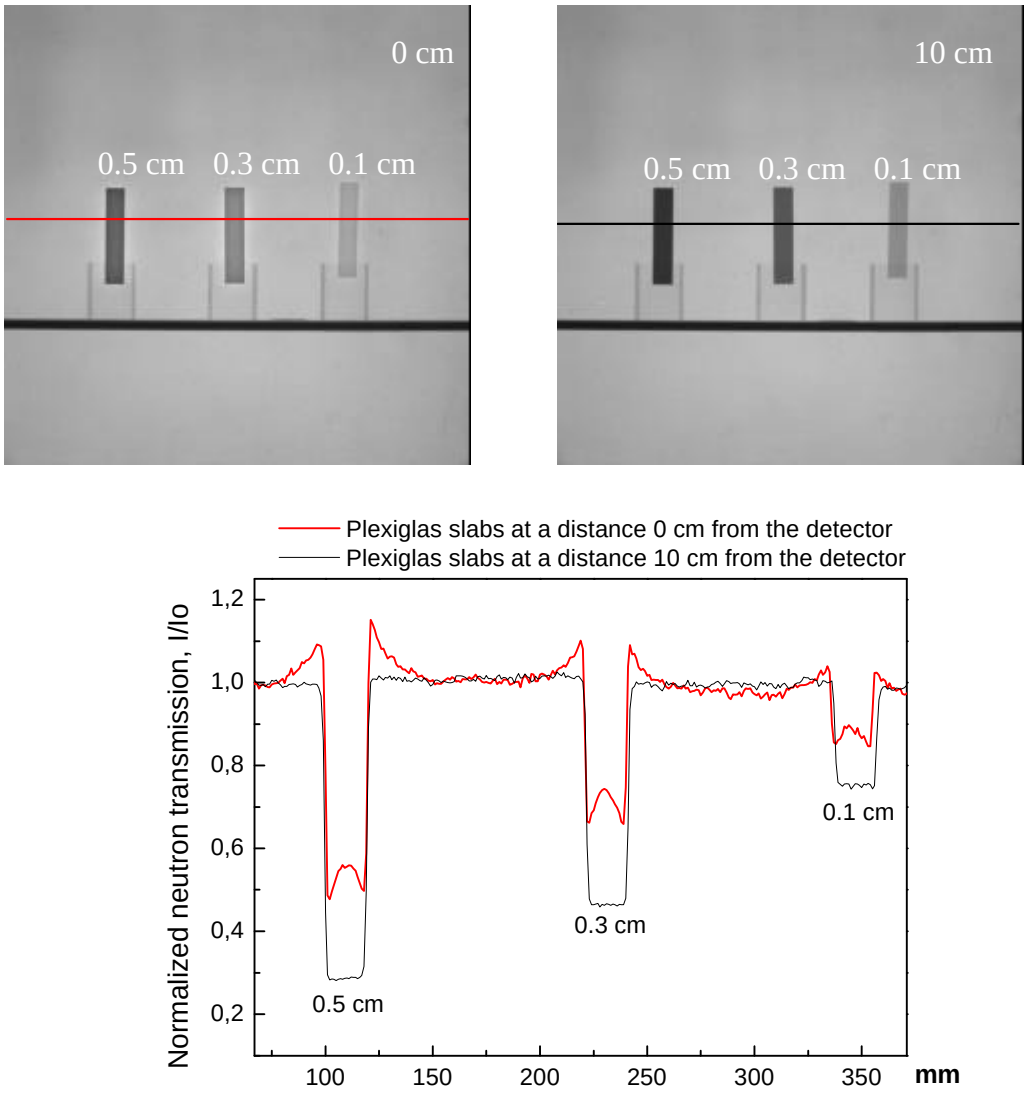

Figure 6.2: Radiographs of PMMA slabs (1x5 cm) with different thickness at 0 and 10 cm from the radiography detector. The intensity profile through the slabs is shown below.

The obtained distance-dependent transmission in Fig. 6.2 can be explained with the fact that the attenuation of the neutron beam in a hydrogenous material (such as PMMA - $C_5H_8O_2$) is determined mainly from the scattering properties of hydrogen. Hydrogen possesses a very high scattering cross-section for thermal neutrons (80.26 b). As it is known the scattering cross-section has two components, which concern the coherent and incoherent interaction between the neutrons and the matter. The coherent part is angular dependent while the incoherent part is not angular dependent and its contribution goes into the whole space – 4π. Since hydrogen scatters dominantly incoherently we can expect that behind the illuminated sample the scattered neutrons

will be distributed uniform in space and the projection of the scattered neutron component on some plane behind the sample will depend on the distance between the scattering medium (the object) and the plane (the detector). In case of a preferentially coherent scatterer as iron for example, the scattering contribution will be not homogeneous in 4π but for a polycrystal sample a 2π symmetry can be considered behind it in a plane transversal to the direction of neutron propagation. Consequently the cross-sections of the so defined scattering cloud with the detector plane will form different neutron distributions, which will be more smoothed at larger distances between the sample and the detector. Such examples are shown in Fig. 6.3 where two MCNP simulations are presented.

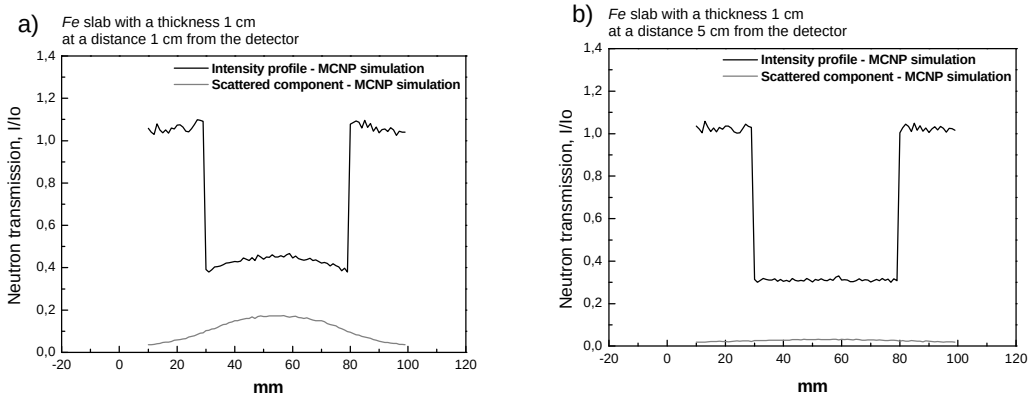

Figure 6.3: Monte Carlo simulations of a neutron radiography of a iron slab (1 x 5 cm) with a constant thickness of 1 cm at two distances to detector of a) 1cm and b) 5 cm. The contribution of scattered neutrons was calculated separately.

For the shown simulations parameters close to these at NEUTRA radiography station (neutron spectrum, beam divergence et.) were used. It can be seen that simulated profile in Fig. 6.3 a follows very well the image formation model presented in Fig. 6.1.

6.3 Representation of the image formation in terms of a PSF superposition

The process of a neutron radiography image formation can be described in terms of a Point Spread Function (PSF) superposition for a given space discretization. If one uses the same discretization for the detector as well as for the neutron source then the PSF can be represented as a sum of two parts - the collided and uncollided neutrons for one volume element. The neutron distribution corresponding only to the collided part of the PSF can be defined as Point Scattered Function (PScF). In these terms the superposition of PSF with a step equal to the discretization step will give the full picture of the investigated object while the superposition of PScF will describe only the scattered neutron part in the radiography experiment. The scattering effect is position dependent since the scattering events are possible only in the sample area. The neutron scattering

contribution depends of course on the sample material and its thickness as well on the distance between the sample and the detector. Taking into account these factors an image correction algorithm can be developed using a subtraction of the corresponding PScF for each pixel belonging to the sample area. In this way the scattering contribution to the radiography image will be eliminated.

Our attempts to measure the PScF for different water layers using the combination of a small pinhole in a 1 mm thick Cd plate and an absorber disk with the same diameter positioned directly on the scintillator opposite the pinhole showed that the signal from scattered neutrons was below the noise level of the detector system. Because of that a Monte Carlo model was used for a calculation of the PScF for homogenous materials. The geometry of the used model is shown in Fig. 6.4. MCNP-4B code [Bri96] was used for the calculations. The source and the detector surfaces were composed of small square areas (pixel discretization). The PScF was calculated as a spatial distribution of scattered neutrons over the detector surface for one emitting source element. For simplification of the model a parallel neutron beam was used. Examples for such a calculated PScF for different thicknesses PMMA ($C_5H_8O_2$) and Iron (Fe) and for different sample-detector distances are shown in Fig. 6.5.

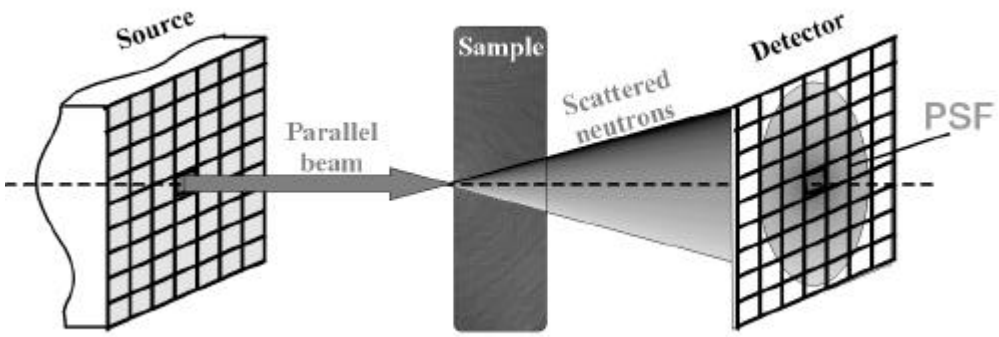

Figure 6.4: The used Monte Carlo model for a calculation of the PSF for defined material, material thickness and distance between the sample and detector

The scattering behaviour for these two materials is very different as it can be seen from the plots. The PMMA PScF posses a drop in the central part while the Fe PScF have no such local minimum in their centre. The reason for this difference can be explained with the different neutron scattering properties of these two materials considered in the Monte Carlo simulation. Since MCNP code uses the imperfect description of the materials as a gas of free atoms then for a hydrogenous material like PMMA the interaction between the neutron and the hydrogen atom (which can be represented as a single proton) can be regarded as an inelastic collision of two balls with equal masses. In this case the energy transfer at a head-on collision will be maximal and the neutron will lose almost all its energy. Taking into account the model shown in Fig. 6.4

obviously the contribution in the central pixel for this case will be only from multiple scattered neutrons. In all other positions excepting the central pixel there will be an additional contribution also from the single scattering.

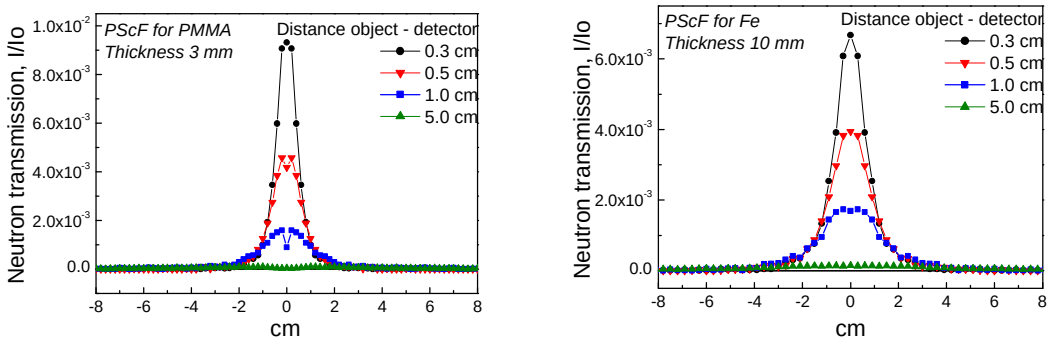

Figure 6.5: Calculated PScF for defined thicknesses PMMA (3 mm) and Iron (10 mm) at various distances to the detector

The superposition procedure with previously calculated PSF and PScF was tested with real radiography experiments performed at the radiography facility NEUTRA at PSI, Switzerland. For this purpose PMMA and Fe slabs with different thicknesses were investigated at various sample-detector distances. As a detector an imaging plate detection system in combination with BAS-2000 IP scanner was used. The results for PMMA samples at different distances from the detector are shown in Fig. 6.6.

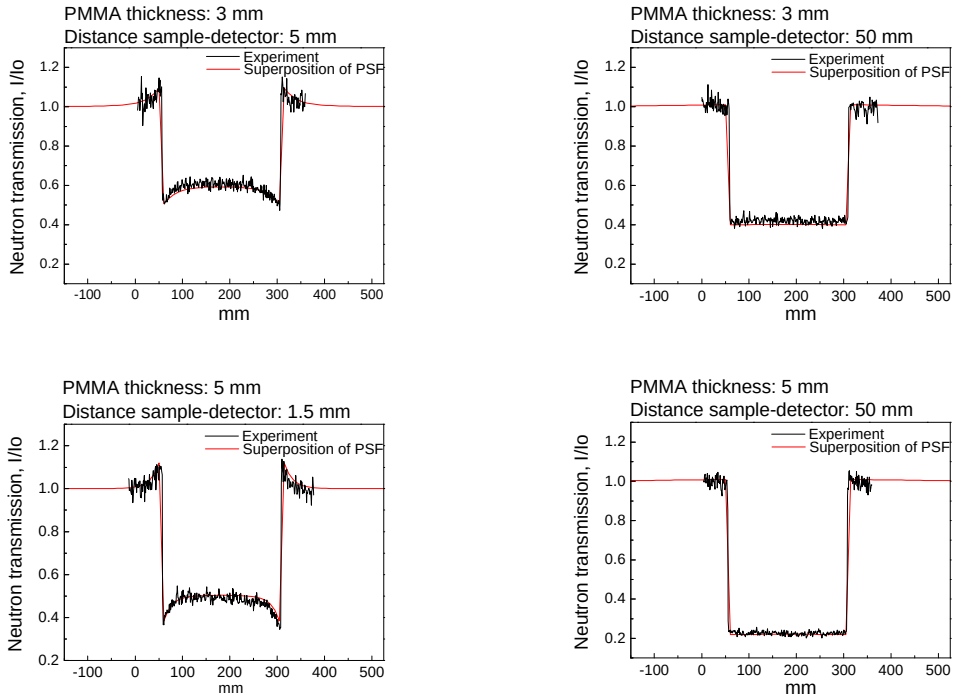

Figure 6.6: Comparison between the profiles calculated as a superposition of PSF and experimental data for different thicknesses of PMMA at different distances between the object and detector

For the simulations real time-of-flight data measured at the NEUTRA beam line were used as a description of the neutron energy distribution in the MCNP input file. The good agreement between the simulated and the measured data was a necessary requirement to make the next step in direction to real image corrections with the calculated PScF.

6.4 Corrections due to scattered neutrons in radiography experiments

The correction algorithm was based on the subtraction of the calculated corresponding PScF from every sample pixel and its surrounding. To perform the correction procedure in the appropriate way the simulated PScF for the corresponding neutron spectrum was rescaled and renormalized in the same way as in the experimental image. Software written in IDL® was used to perform the image processing. The first corrections were performed on objects with a simple geometry – slabs with a constant thickness. In this case both parameters thickness and object-detector distance are fixed and the PScF can be calculated in a simple way.

The example for such a correction is presented in Fig. 6.7 where a radiography picture of a PMMA test sample (slab) with a thickness of 3 mm placed at a distance of 5 mm from the detector was processed with the PScF calculated previously for these experimental conditions.

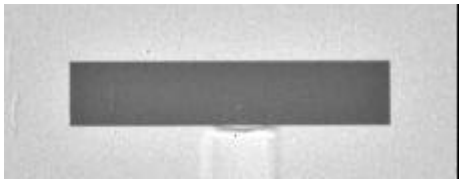

a) Before the correction

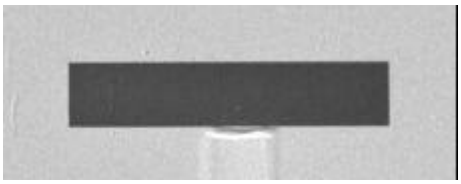

b) After the correction

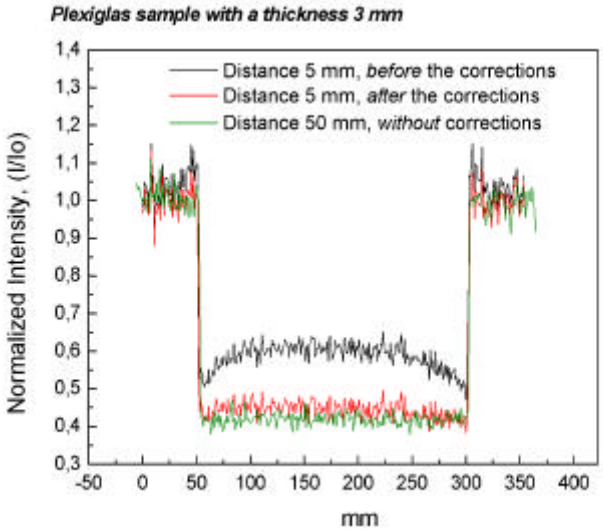

Figure 6.7: Correction of the build-up effect due to scattered neutrons in the radiography image of a PMMA slab with a thickness of 3 mm at a distance of 5 mm to the detector

From the horizontal intensity profiles taken in Fig. 6.7 before and after the correction procedure presented in the plot, it is evident that the effect due to the scattered neutrons (Fig. 6.1) is corrected and an intensity profile with a flat plateau is obtained. To check

the reliability of the corrected data a comparison was performed with the case where the sample was investigated at a big object-detector distance of 5 cm. Under such circumstances the contribution of scattered neutrons is very small (see Fig. 6.5). The good agreement between the corrected and the experimental data at a bigger object-detector distance presented in Fig. 6.8 was a criterion that the performed corrections were done in the right way.

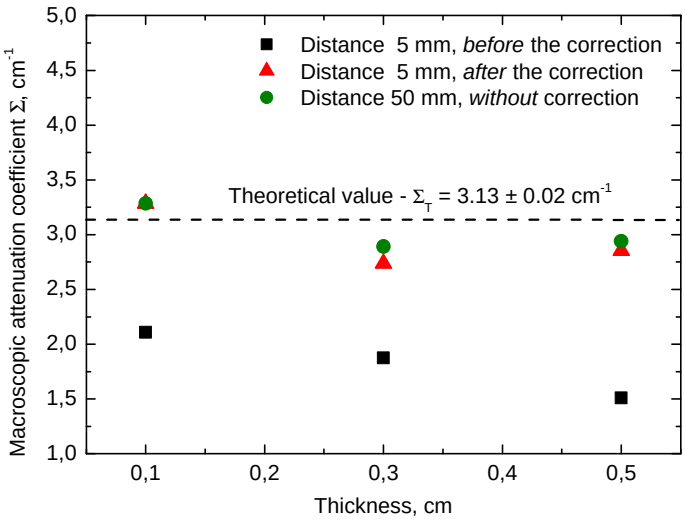

Figure 6.8: Calculated thickness dependence of the attenuation coefficients for PMMA for two distances between the object and detector and compared with the data after the correction

The main goal of the presented correction method is its application for quantitative radiography investigations where the correct determination of the attenuation coefficient value for the corresponding material is important. For example, in Fig. 6.8 the value of the PMMA attenuation coefficient for neutrons is calculated using the obtained intensity profiles for three sample thicknesses at two different distances to the detector. The values calculated from the corrected profiles at the closer distance to the detector are also presented. It can be seen that after the correction procedure the values for the attenuation coefficient agree very well with the case where the sample was investigated far away from the detector. The corrected values are also in agreement with the given theoretical value for PMMA (the dashed line in the graph). The observed fluctuations around the theoretical value were related to the statistical errors from the experiment.

The next step was a correction of a more complicated sample with an inhomogeneous thickness. The example is presented in Fig. 6.9, where a PMMA step wedge was used as a test sample. For each thickness the corresponding PScF was calculated previously. In the correction procedure for different steps, different PScF were subtracted. The intensity profile through the corrected wedge was compared with the profile of the same step wedge investigated at a larger distance (5 cm) between the sample and the detector. The good agreement between the corrected and the experimental data is obvious.

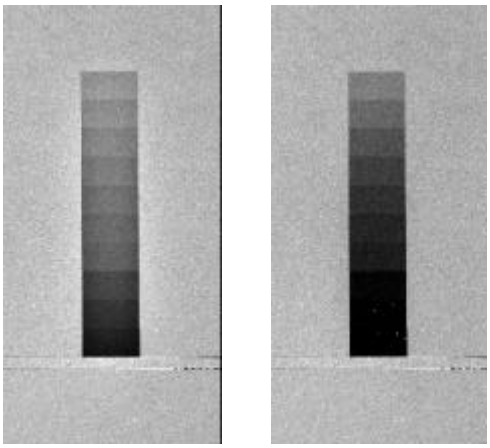

Before the correction After the correction

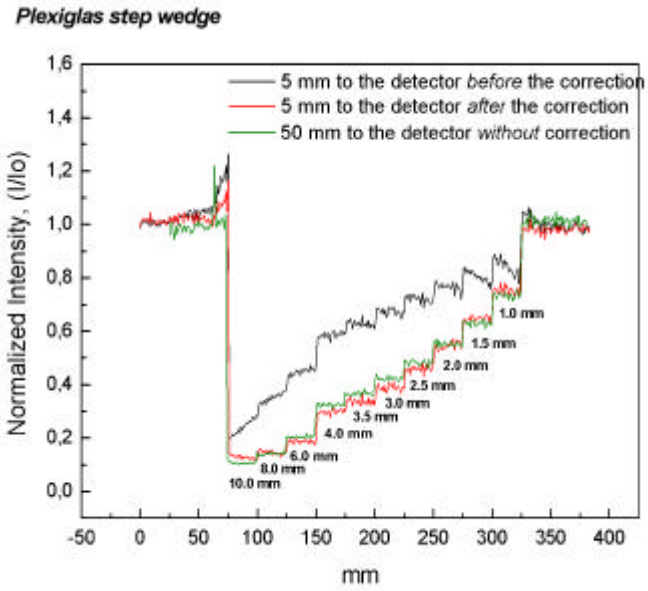

Figure 6.9: An example for a build-up correction of a more complicated PMMA sample (step wedge) at a distance of 5 mm between the sample and the detector

A systematic study of the scattering contribution to the neutron radiography image formation at different distances between the sample and the detector was carried out for a liquid test sample of D2O layers. The experiments were performed at the thermal neutron radiography station at the South African research reactor SAFARI–1, Fig.6.10*.

Figure 6.10: A view on the thermal radiography station at SAFARI-1. The location of the setup in respect to the reactor (left). A look at the experimental bunker (right)

The main parameters of the radiography facility are its L/D ratio of 153 and the available neutron flux at the sample position of 1.08×10^7 n/cm^{2}s.

* The experiments were performed at SAFARI-1 with the kind contribution of Dipl. Ing. F. deBeer

As a detection system a standard CCD radiography configuration was used. The image obtained on the NE426 (^{6}LiFZnS:Ag) scintillator was projected via a mirror and an optical lens system to a Sony XC-77CE type CCD chip (Analog video) with a 756(H) x 581(V) pixel array and 11µm x 11µm pixel size. The dynamic range of the camera was 16 bit and the projection ratio was set to 220 µm /pixel.

The liquid was filled into an aluminium container with subsections corresponding to different thicknesses, as shown in Fig. 6.11. The subsections were separated with 1.5 mm Al plates. The possible thicknesses of the liquid were from 1 to 15 mm (1mm step).

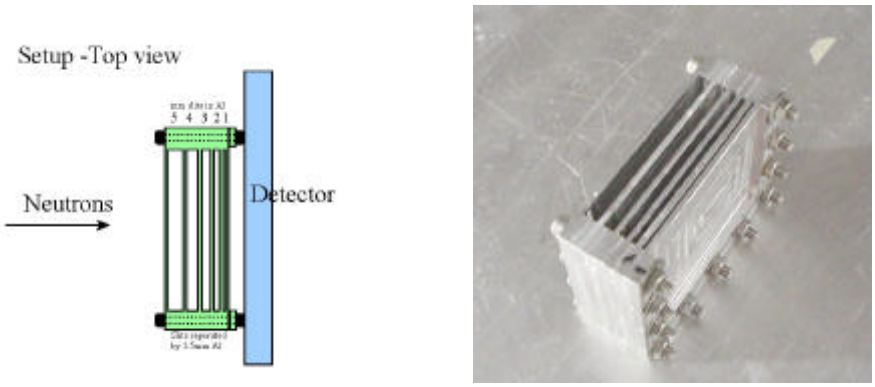

Figure 6.11: The aluminium container used in the radiography experiments. A layout (on the left) and a photo (on the right)

The normalization of the radiography images was performed through division by the image of the empty container. By that an information about the beam attenuation only due to the liquid layer was obtained assuming that the container itself has a negligible influence on the neutron scattering from the liquid. Every layer with a defined thickness was imaged at different distances from the detector. The quantification of the radiographs at different experimental parameters (liquid thickness, distance object-detector) was conducted by taking horizontal intensity profiles through the liquid area on the normalized radiography image as it shown in Fig. 6.12.

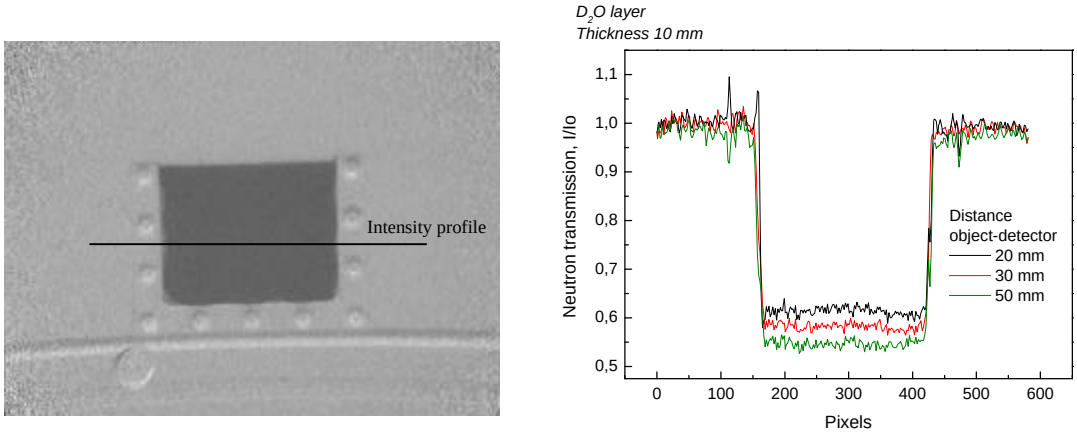

Figure 6.12: The normalized radiography image of a 10 mm thick layer of D_2O at a distance of 30 mm from the detector plane (left) and the intensity profiles for the same layer at different distances from the detector (right).

In this way the neutron transmission I/I_0 was determined for the whole set of liquid thickness and three object-detector distances: 20 mm, 30 mm and 50 mm. For each liquid thickness d the macroscopic attenuation coefficient was calculated as: $\Sigma = d^{-1}\ln(I_0/I)$. The presented errors were defined by the statistical fluctuations in the measured transmission. For the calculated PScF a real neutron spectrum measured by a time-of-flight technique at the SAFARY-1 reactor was used. The corrections were performed following the correction procedure described above. The obtained data are summarised in Fig. 6.13.

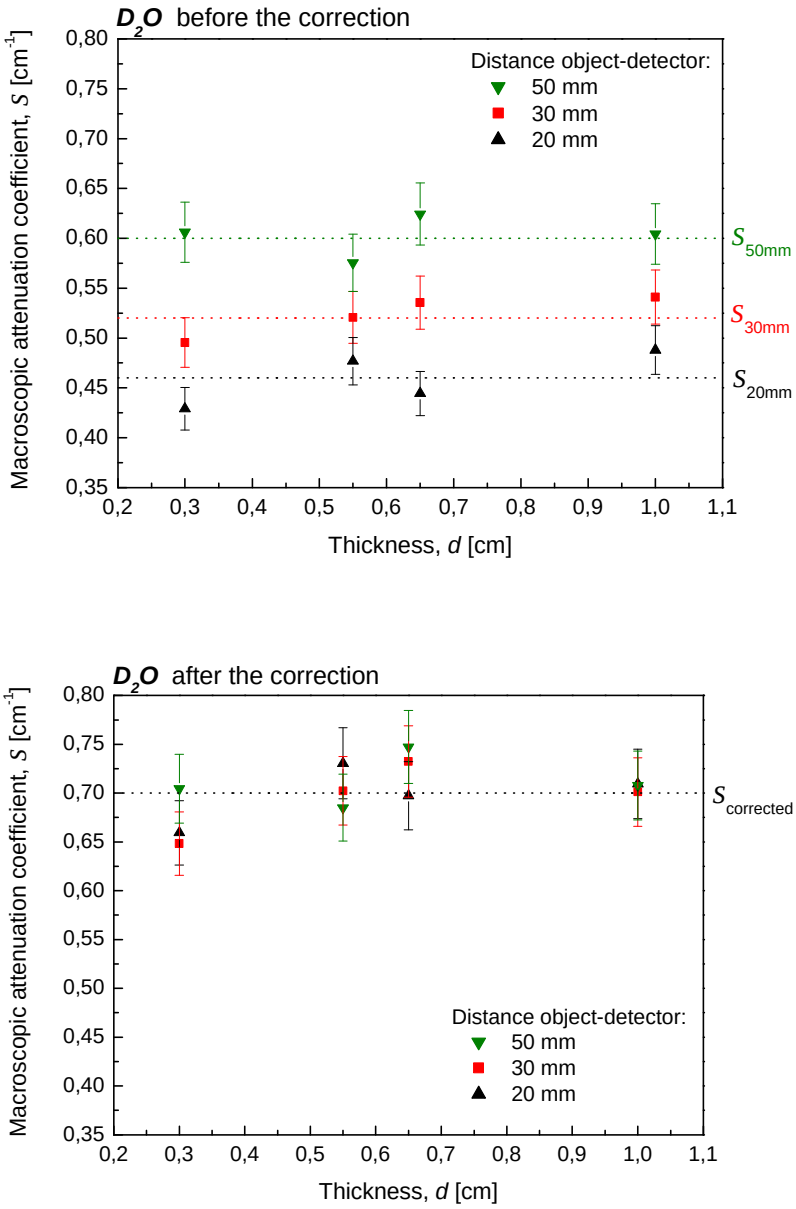

Figure 6.13: Calculated macroscopic attenuation coefficients from experimental data (above) and from corrected data (below) for different thickness heavy water at various distances to the detector.

The presented diagrams in Fig. 6.13 show an increase of the neutron beam attenuation after the application of the correction procedure as expected. It can be seen that the dependence of the attenuation coefficient on the sample to detector distance after the correction is very small and it is within the error range.

For a further development of the correction procedure a replacement of the now used PScF with analytical functions depending on the sample thickness and on the object-detector distance for a defined source spectrum can be tested. In this way the radiography images of objects with more complicated geometry could be corrected.

Chapter 7: Monte Carlo Simulation of Neutron Attenuation Properties of Borated Steels

7.1 Introduction

Boron alloyed steel is an important shielding material at a long-term storage of spent nuclear fuel or at nuclear waste disposals. Therefore it is important to define quantitatively its neutron attenuation characteristics in dependence on the thickness using experimental methods. Due to the high neutron absorption cross-section of boron compared to metals the neutron radiography is a powerful tool for an investigation of the boron distribution homogeneity in borated metals. Because of the observed differences between experimental results and theoretical predictions concerning the attenuation properties of borated steel [Bur58], [Bry78], [Wel87], [Gao97]. Monte Carlo simulations (MCNP-4B code [Bri96]) were performed for better understanding and interpretation of the transmission process taking into account secondary effects as the beam hardening, the level of material heterogeneity and the background. Different analytical models can be used as an input for the simulations to approach the actual structure and to determine the heterogeneity levels of boron alloyed steels. The Monte Carlo simulations can be used to estimate as well the quantitative contribution of the beam hardening and the background effects to the radiography image.

7.2 Exponential attenuation

The neutron transmission through borated steels can be calculated as a simple exponential attenuation $I/I_0=\exp(-\Sigma_{B+Steel}d)$, where the attenuation coefficient $\Sigma_{B+Steel}$ is considered for a homogeneous mixture of defined parts of B and Fe atoms at a neutron energy of 25 meV (1.8 Å) – thermal neutrons. The calculated attenuation coefficient at these conditions $\Sigma_{B+Steel}=7.32$ cm^{-1} (1.88 wt.% B) is compared in Fig. 7.1 with

transmission experimental data, obtained at the thermal neutron radiography facility NEUTRA at SINQ, PSI.

The radiography images were taken with the help of a CCD based radiography system, described in details elsewhere [Leh99]. Different numbers of plates of borated steel (1.88 wt.% B) with a constant thickness of 2 mm were used to compose the desired material thickness. For the measurement half of the detector scintillator was covered with N plates stacked together and having a common thickness $d = 2N$ mm. The neutron transmission through the plates I/I_0 was calculated as the ratio between the image intensities in the sample area I and in the open beam area I_0. The attenuation coefficient at the corresponding material thickness d was obtained by the following expression: $\Sigma_{B+Steel} = -(\ln I/I_0)/d$.

The disagreement between calculated and measured values, observed in Fig. 7.1, leads to the conclusion that the simple exponential attenuation model is not applicable in this case. The deviation was related mainly to the contribution of the secondary effects as beam-hardening, material heterogeneity and some background. Since the mentioned effects depend mainly on the material thickness and the boron concentration in steel, plates with different thickness and boron concentrations were used as test samples in the performed experiments and simulations. For an estimation of the contribution of the secondary effects Monte Carlo simulations were performed, where analytical models for each of the effects were used.

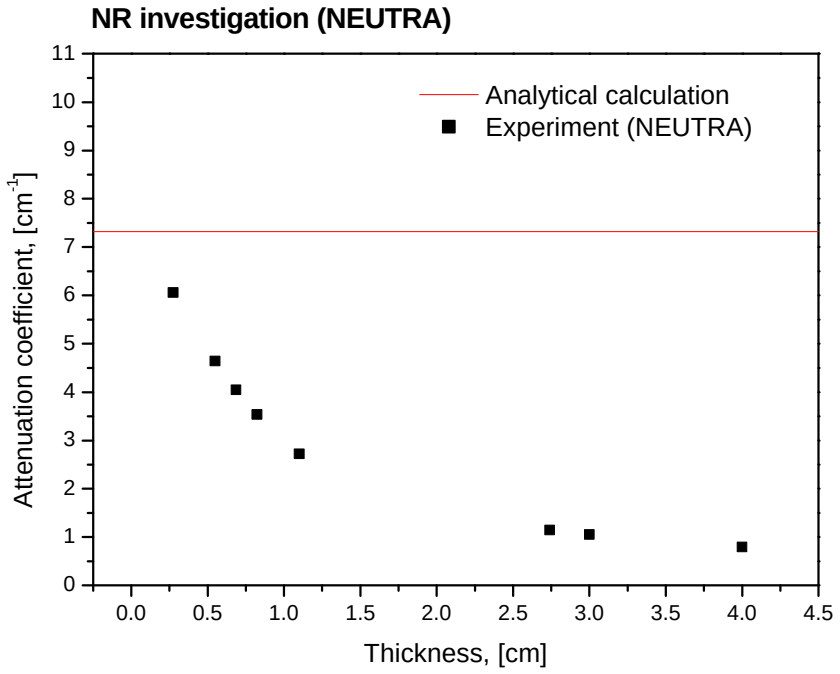

Figure 7.1: A comparison between calculated and experimentally obtained attenuation coefficient for borated steel (1.88 wt.% B)

7.3 Secondary effects

Beam hardening

This effect takes place in strongly absorbing materials such as Boron (s_a/s_s~200 for thermal neutrons), where the probability for absorption of slow neutrons increases with 1/v (v – neutron velocity) (Fig. 7.2). Consequently, the mean energy of transmitted neutrons through such a material will be higher than before the penetration. Because the probability for a neutron absorption and consequently for a detection in a radiography scintillator is energy dependent, the beam hardening causes a deviation of the quantitatively estimated neutron attenuation in borated steels. The thickness dependent effect was investigated by a simple Monte Carlo model, where the neutron transmission through different thicknesses of borated steel was simulated. For a material specification in the simulation a homogeneous mixture of boron and steel was used. The shift of the transmitted spectra and the thickness dependence of the calculated attenuation coefficient are shown in Fig. 7.3 and Fig. 7.4.

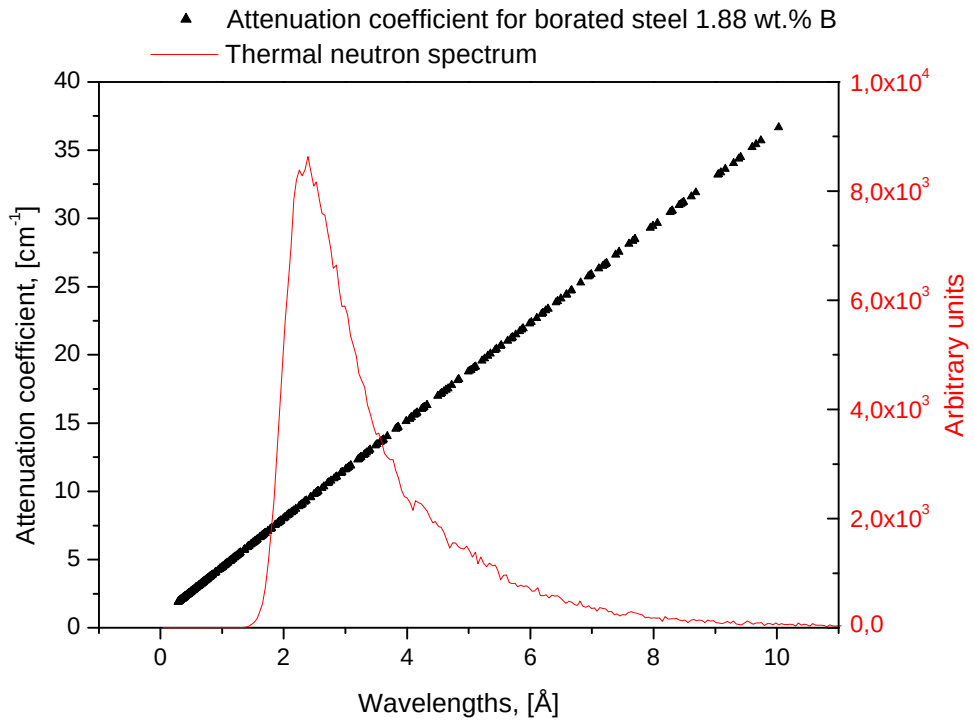

Figure 7.2: Typical thermal neutron spectrum measured at FRM I, QR Meßhaus and the energy dependence of the borated steel (1.88 wt.%) attenuation coefficient.

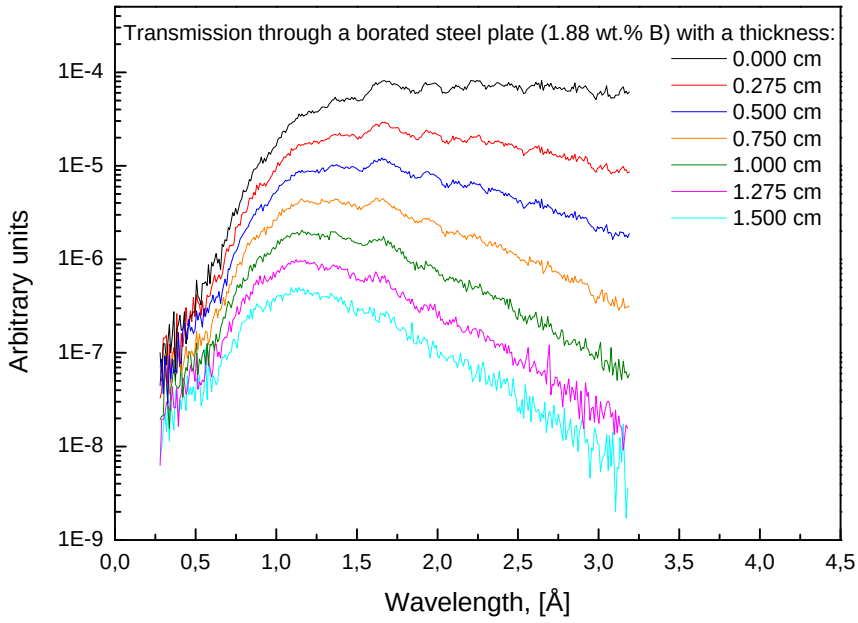

Figure 7.3: Thermal neutron beam spectra (NEUTRA at SINQ) before and after the transmission through different thickness of borated steel.

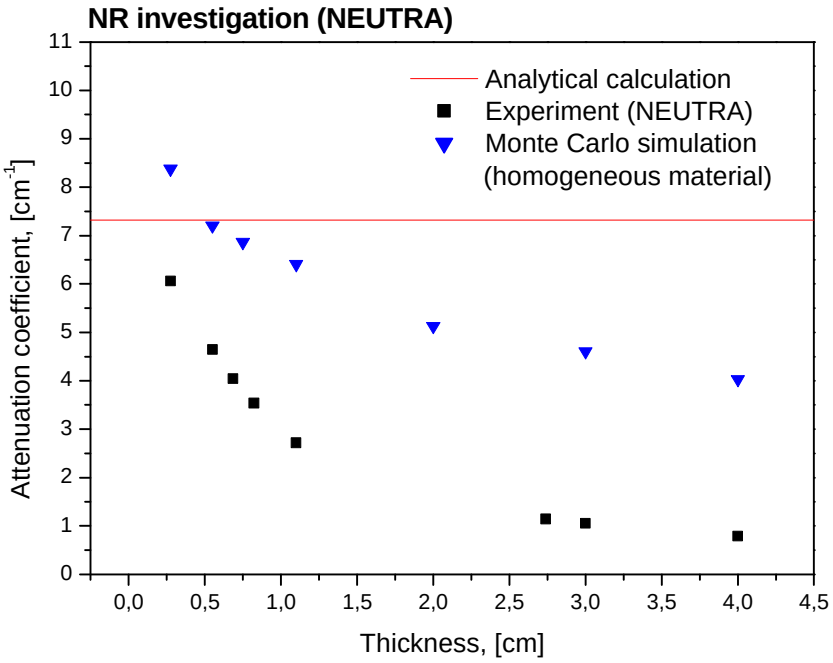

Figure 7.4: Comparison between attenuation coefficients obtained from experimental and simulated data.

Inhomogeneity of the boron distribution in the steel matrix

SEM (Scanning Electron Microscope) investigations of the surface of boron alloyed steel samples show an inhomogeneous distribution of the boron powder in the metal matrix (Fig. 7.5). Because of that, a simple MC model was considered, the so called channel approximation, where different levels of material heterogeneity were simulated. Here the borated steel was represented as a combination of "conducting" (pure steel) and "blocking" (borated steel) channels through its thickness *d* (Fig. 7.6). The volume ratio of the pure steel channel, presented in Fig. 7.6, to the whole cell was used as a parameter describing the material inhomogeneity. For instance at a subdivision of the sample volume into cells having a volume of 1 x 1 x *d* mm^3 the "conducting" steel channel with a volume of 0.1 x 0.1 x *d* mm^3 will determine a heterogeneous ratio of $0.01d$ mm^3 / $1d$ mm^3 = 1%. By testing different heterogeneous ratios for a 1.88 wt % borated steel, the best agreement between experimental data and MCNP simulations was found at a heterogeneous ratio of 3.2 % (Fig. 7.7).

Figure 7.5: A slice image of a boron alloyed steel sample taken by SEM in a 3.75 mm line.

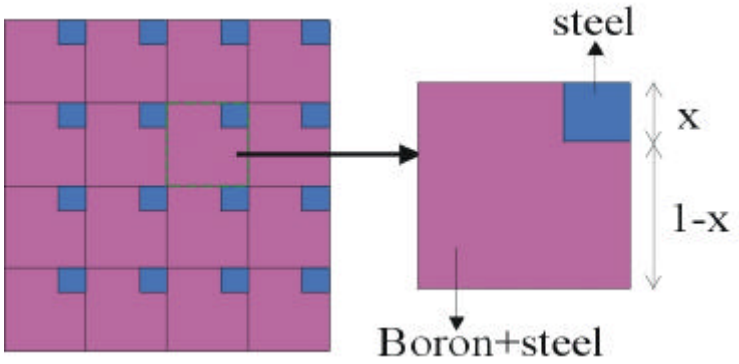

Figure 7.6: A channel model representation of a heterogeneous borated steel sample used in the MC simulations.

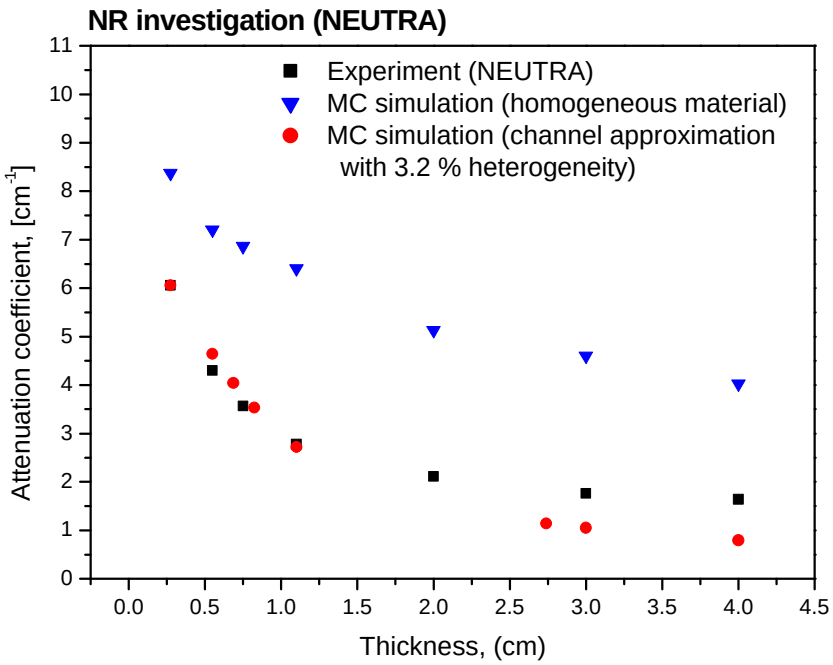

Figure 7.7: Comparison between attenuation coefficients obtained from experimental and simulated data (3.2 % heterogeneous ratio) for different material thickness.

Background corrections

In spite of the complete MCNP simulation the result presented in Fig. 7.7 shows that the attenuation process cannot be described completely taking into account only the beam hardening and material heterogeneity secondary effects. The difference between simulated and measured data can be related to the existence of some level of a homogeneously distributed neutron background in the radiography experiments. The sources for such a background are mainly scattered neutrons from the radiography set-up equipment itself and from the bunker walls. One can see that the large deviation in Fig. 7.7 is at large thicknesses, where the signal from transmitted neutrons is negligible. In that case the constant background dominates and the measured signal levels cannot be explained with a MCNP model, where the background is not assumed. To estimate the level of the background, the following model was considered: If the investigated sample does not influence the spatial distribution of the background, then it could be considered to be proportional to the initial beam intensity:

$$I_{BG} = k\, I_0$$

where k is a proportional coefficient. Consequently using this assumption, the following expression for the experimental transmission can be obtained:

$$\frac{I_{\exp}}{I_{0,\exp}} = \frac{I + I_{BG}}{I_0 + I_{BG}} = \frac{I + kI_0}{I_0 + kI_0}$$

where I and I_0 are the transmitted and the initial neutron flux and I_{exp}, $I_{o,exp}$ are their experimentally measured values. At thicker absorbers the number of the transmitted neutrons will be very small ($I << kI_o$), which gives directly the boundary condition:

$$\frac{I_{\exp}}{I_{0,\exp}} = \frac{k}{1+k} \text{ , (at } I << kI_o)$$

Therefore, for a thick material, an artificial attenuation coefficient S_{BG} will be calculated:

$$\Sigma_{BG}(d) = -\frac{1}{d}\ln(\frac{k}{1+k}),$$

The obtained expression was used as a fit function through the experimental points varying the proportional coefficient k. The best agreement was found at k = 0.05, where the obtained curve fits very well to the points corresponding to material thicknesses bigger than 1.0 cm (see Fig. 7.8). In that case a detection limit of the radiography system can be defined where the measured signal is still higher than the background level.

The comparison between the experimental and simulated data in the relevant thickness interval shows very good agreement.

The main conclusion from this short investigation was that at neutron transmission through strong absorbing materials the contribution from secondary effects as beam hardening, material heterogeneity or background are very important and they have to be taken into account by theoretical considerations and simulations. This is very important at shielding calculations for a long-term storage of spent nuclear fuel or at nuclear waste disposals in containers made up of borated steel. Borated steel is used also for the design and construction of a nuclear reactor equipment which is placed in the active zone of the reactor. In this case the theoretical calculations for the criticality of the facility will be uncertain if the attenuation coefficient for one of the constructed materials is wrong. Therefore such kind of Monte Carlo simulations are obligatory for experimental projects with a high level of reliability.

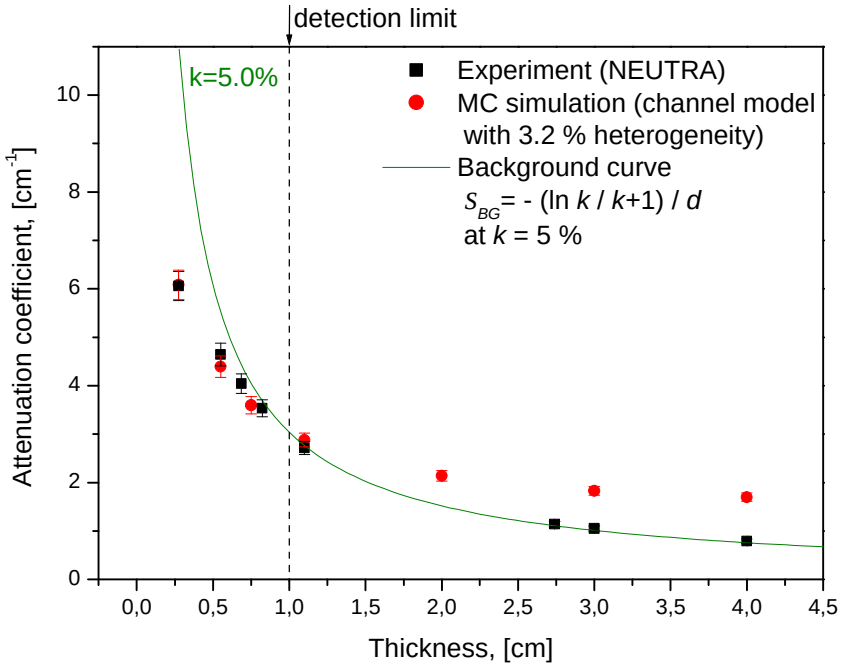

Figure 7.8: The background contribution sets a detection limit of the radiography system at d < 1.0 cm.

Chapter 8: Optimisation of a Mobile Neutron Source Based on the Sb-Be Reaction

8.1 Requirements

The main requirements necessary for an optimised layout of a mobile neutron source for radiographic and tomographic measurements can be summarised as follows:

- high neutron yield on a large area at the sample position
- homogeneous beam distribution at the sample position
- small angular distribution at the sample position
- optimised spectral distribution, preferably a thermal neutron spectrum
- good shielding of gamma-radiation and neutrons (radiation safety)
- simple to use and handle
- minimised dimensions and weight
- low cost in set-up and maintenance
- on/off switching of the neutron source

Accelerator driven neutron sources are quite expensive and, due to their high initial neutron energies of 2 MeV to 14 MeV, an optimised spectral distribution within minimised dimensions is hard to achieve. The latter also holds for most of the remaining radioisotopic sources or they are not on/off switchable without special shutter systems (e.g. ^{252}Cf source).

Among the remaining radioisotopic neutron sources the Sb-Be reaction seemed to be the most promising one. Here the production of neutrons is based on the (γ,n)-photo-neutron reaction (threshold energy: 1.666 MeV) producing neutrons with a mean energy of about 24 keV. The reaction is mainly initiated by the 1.69 MeV gamma-line of ^{124}Sb with a transition probability of 47.1 %.

The thermalisation of the emitted neutrons requires a small layer of polyethylene only. By mechanical separation of the ^{124}Sb from the surrounding beryllium target the neutron generation can be stopped immediately. As ^{124}Sb can be produced in our research reactor (FRM II) by neutron activation, the costs for maintenance are minimal. The main disadvantage of a Sb-Be source with a high thermal neutron flux is the required high gamma activity of ^{124}Sb. This can be overcome by an optimised design and the use of a detection system which is less sensitive to gamma radiation.

In the past, Sb-Be sources of different design have been developed and applied for many purposes, e.g. for CT (Computer tomography) on iron products [Fuj90], for radiography in hot cells and for in-pool inspection of irradiated fuel and control rods [Dom92] as well as for active neutron investigation of radioactive waste packages [Cas98], though none of these designs seemed to be suitable for in-field application. To satisfy all requirements in an optimum way a new design for the source layout was developed using extensive MCNP and shielding calculations*.

8.2 Design

Antimony source

For the Sb-Be source an antimony rod of 10 cm length, 1.27 cm diameter and a purity of 99.8 % (metal basis) is used as gamma emitter. It was cut into four pieces each 2.5 cm in length which should be homogeneously activated by neutrons up to a gamma activity of about 1 GBq in total at a research reactor (e.g. FRM II). The cutting procedure was performed using a saw-blade with very low cobalt content to avoid a contamination of the antimony pieces by this material which can cause a high activation. The antimony pieces are sealed in small aluminium containers and capsuled in a large aluminium cylinder, giving an antimony source of an outer length of 14 cm.

*Neutron yield**

The target material for the production of photo-neutrons is beryllium. It has cylindrical or rectangular geometry and contains the antimony source in its centre. The thickness of the beryllium target for maximum neutron yield was calculated by Monte Carlo simulations using equation [Gry00]

$$w(E) = \frac{s_{gn}(E)}{s_{tot}(E)}(1-\exp(s_{tot}(E)\,r\,d)), \qquad (8.1)$$

where $w(E)$ is the neutron yield per gamma quanta emitted in the antimony source, s_{gn} the photoneutron-production cross section, s_{tot} the total photon scattering and

* The shielding and the neutron yield calculations were performed at the Institut für Radiochemie, Technische Universität München.

absorption cross section, *r* the target density and *d* the target thickness. The target height was 16 cm, the diameter of the central drilling for putting the ^{124}Sb was 2.6 cm.

The calculated neutron yield per emitted gamma quanta for beryllium cylinders of different wall thicknesses and for a rectangular target geometry (8.6 cm x 6 cm x 16 cm) are shown in Fig. 8.1.

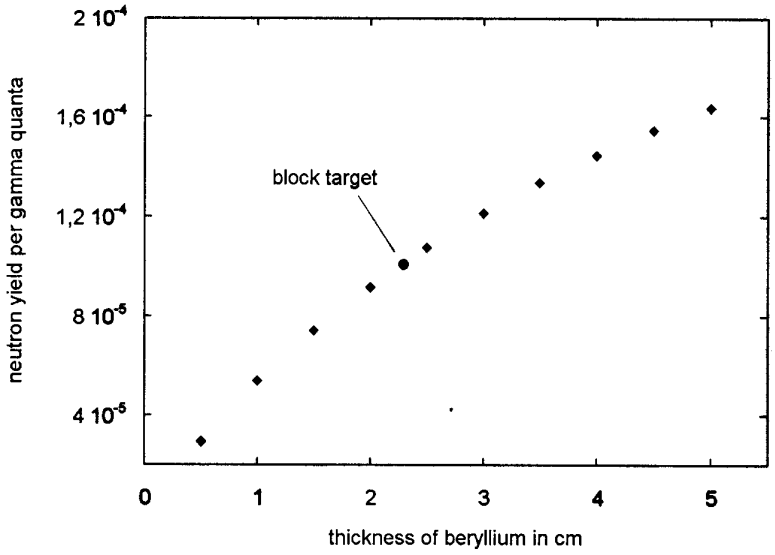

Figure 8.1: Calculated neutrons per gamma quanta for different wall thicknesses of cylindrical beryllium targets and a block target (8.6 cm x 6 cm x 16 cm).

The results suggest to use a beryllium target being as thick as possible but this strongly influences the dimensions and mass of the gamma shielding required. Additionally as the selected target geometry must be cut out of a large beryllium block, also the tooling of beryllium must be considered since beryllium is a toxic and hard material. Balancing these points the block target was finally selected providing a yield of about 10^{-4} neutrons per emitted gamma quantum.

The beryllium was cut by EDM (Electrical Discharge Machining) as described below in more details.

Shielding[*]

A high neutron yield at the sample position requires a gamma activity of the ^{124}Sb of several 10^{10} Bq requiring a strong lead shielding especially for in-field measurements. As an internal limit the gama dose rate at a distance of 30 cm from the surface of the neutron source should not exceed 300 µSv/h. Shielding calculations using MicroShield [Neg92] result in a minimum thickness of 14 cm. Figure 8.2 shows the resulting dose

[*] The shielding calculations were performed at the Institut für Radiochemie, Technische Universität München.

rates at the surface of the neutron source, at a distance of 30 cm and 100 cm, respectively, for different thicknesses of the lead shielding surrounding the beryllium block target.

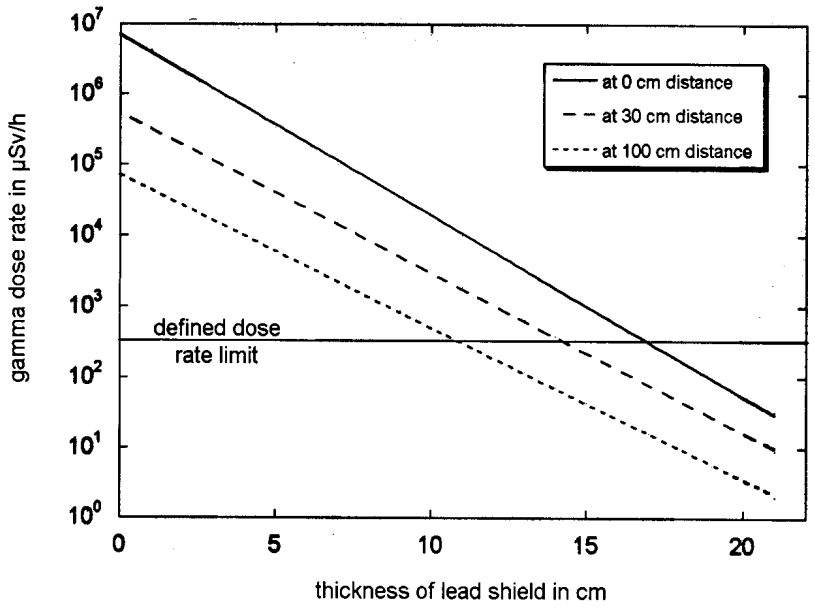

Figure 8.2: Calculated gamma dose rates for different distances from the surface of the source as a function of the thickness of lead.

Optimisation

Based on the neutron yield for the selected beryllium block target, its dimensions and the lead shielding of 14 cm thickness, Monte Carlo simulations using the MCNP 4B code were performed to determine an optimised layout. The geometry used for the simulations is shown in Fig. 8.3. In the centre of the arrangement the ^{124}Sb gamma source is located in order to initiate the neutron emission in the surrounding beryllium target, which itself is embedded in polyethylene acting as reflector and moderator. The lead layer is mainly used for gamma shielding but also to some extent as neutron reflector. The last layer is composed of borated polyethylene (PE) for neutron absorption. Through an outlet window of 10 cm x 20 cm the neutrons are guided to the sample. The materials in the outlet window (PE, Pb) can be removed.

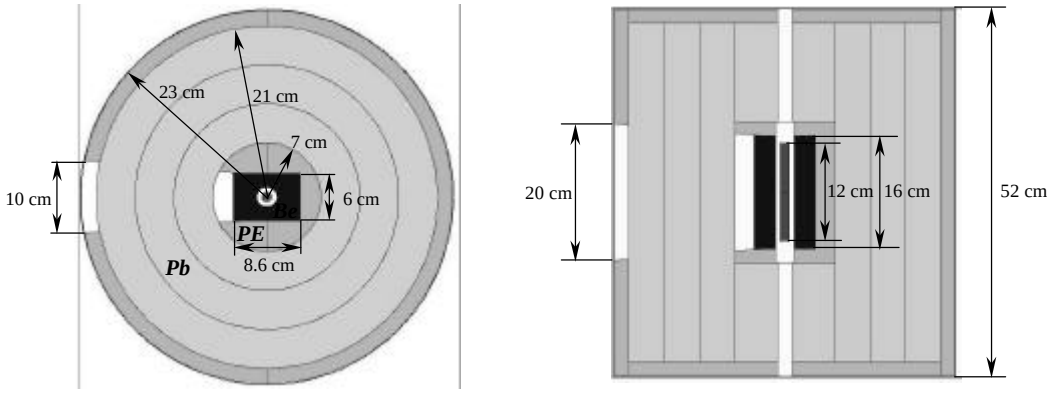

Figure 8.3: Top and side view of the final geometrical layout for simulation.

The spatial distribution of the simulated neutron intensity at the outlet window is shown in Fig. 8.4. A relatively homogenous distribution of the neutron intensity is achieved, with a neutron yield of about $3x10^{-4}$ $1/cm^2s^{-1}$ per emitted neutron. The FWHM area at the outlet window is about 7 cm x 16 cm.

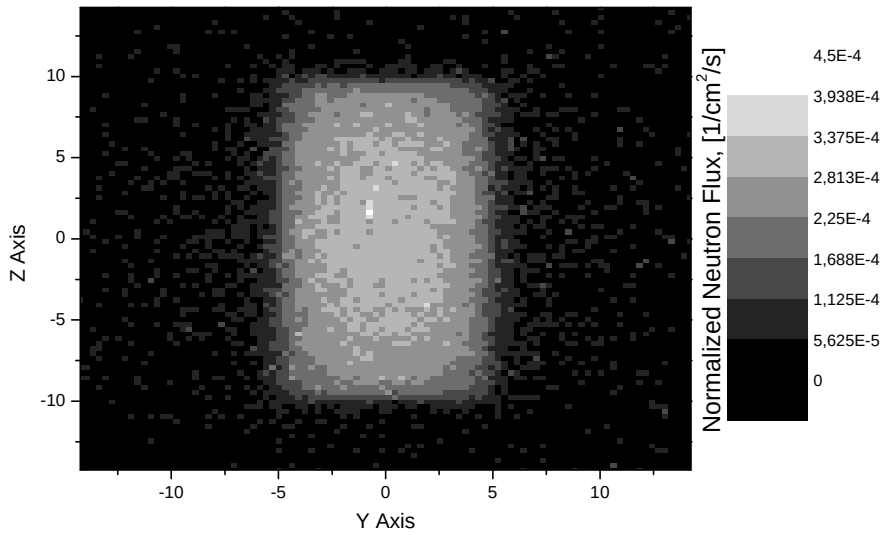

Figure 8.4: Spatial distribution of neutrons at the outlet window.

Further calculations showed that the neutrons emitted with an initial energy of about 24 keV are moderated down to thermal energies proving an approximated thermal neutron spectrum at the sample position. The angular distribution at the centre of the outlet window has a maximum at about 30 degree for the considered layout.

Final layout

The resulting design is shown in Figures 8.5 and 8.6.

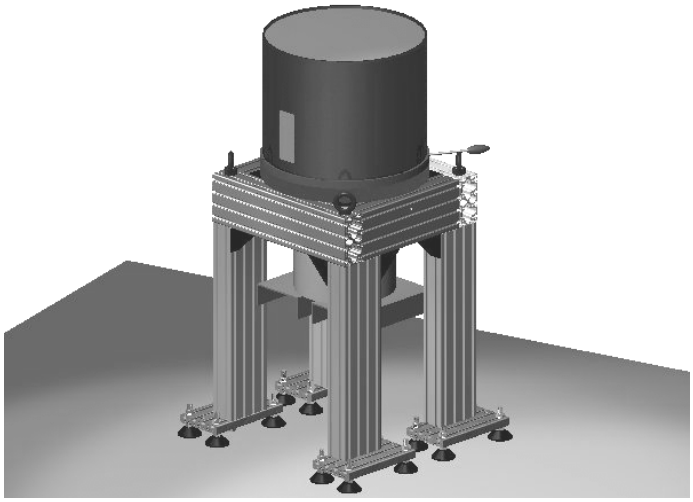

Figure 8.5: Technical drawing: Total view of the SbBe source with flange-mounted storage and transport container.

The SbBe source consists of two parts: the neutron source and the transport and storage container. The latter is made out of lead and contains the cylindrical antimony source if the neutron production is shutdown. For operation the container is flange-mounted from the bottom to the neutron source and the antimony is lifted to the beryllium block, thus starting neutron production. The beryllium block is completely surrounded by layers of polyethylene and lead, except for an outlet window of 10 cm x 20 cm. The layout allows a maximum Sb activity of 3.7×10^{11} Bq resulting in a calculated maximum neutron yield of 10^4 cm^{-2} s^{-1} at a distance of 10 cm from the outlet window.

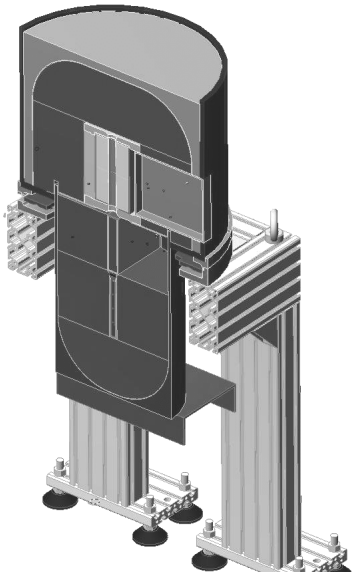

Figure 8.6. Technical drawing: Sectional view of the SbBe source with flange-storage and transport container.

8.3 Realization

The mechanical set-up was performed by the workshop of the Institut für Radiochemie, Technische Universität München, including the casting of lead. One main problem arising during realization was the cutting of the beryllium. As basis material a cylinder of 20 cm diameter and 9 cm height was given. From this, two rectangular blocks of the size 8.4 cm x 5.7 cm x 9 cm (w x l x h) with cylindrical holes of 2 cm diameter had to be cut. Since beryllium is a very hard and brittle material, neither conventional sawing nor water jet cutting was successful. Therefore wire EDM (Electrical Discharge Machining) had to be applied. The two blocks were placed one on the top of the other being the heart of the SbBe source.

The activation of the metallic antimony rods (4 pieces of 2.5 cm length and 1.25 cm diameter) was performed at the research center GKSS, Geesthacht, resulting in an overall activity for ^{124}Sb of 3.7x10^{11} Bq. After some days the activity of the also present ^{122}Sb and some minor impurities were decayed leaving ^{124}Sb as the remaining source of activity. The four activated antimony pieces were transported to Garching where they were sealed in an aluminum container in the hot cells, then placed in the transport and storage container ready for operation.

For lifting the antimony into the beryllium block an electromagnet is used, thus enabling a fast shut down of the neutron emission by simply interrupting the current. Then the antimony source falls back in the transport and storage container by gravity and is well shielded.

8.4 Testing*

The results of all tests reported were performed with a ^{124}Sb activity of 3.4x10^{10} Bq, i.e. with about 10 % of the maximum admissible activity.

Dose rate measurements

The measured gamma dose rates in 10 cm distance from both the transport and storage container containing the antimony source as well as from the source container with retracted antimony source were below 150 μSv/h. In front of the outlet window the dose rate is about 10 mSv/h. The corresponding neutron dose rates are below 1 μSv/h, in front of the outlet window about 36 μSv/h.

* The tests were performed by Dr. Th. Bücherl at the Institut für Radiochemie, Technische Universität München.

Neutron yield

The neutron yield was measured by activation analyses of a thin wire made of aluminum alloy containing 0.2 % (weight) gold which was placed in front of the outlet window and irradiated for 262 hours. The resulting neutron yield is $(2.5\pm0.5)10^3 cm^{-2}s^{-1}$. This value is in excellent agreement with the result of the simulation study ($10^4 cm^{-2}\ s^{-1}$), when corrected for the position and the (maximum) ^{124}Sb activity used for the MCNP calculation yielding $1.4x10^4\ cm^{-2}\ s^{-1}$. This value has to be corrected for the position and the maximum ^{124}Sb activity used in the MCNP calculation, yielding $1.4x10^4\ cm^{-2}\ s^{-1}$, which is in excellent agreement with the result of the simulation study of $10^4 cm^{-2}\ s^{-1}$.

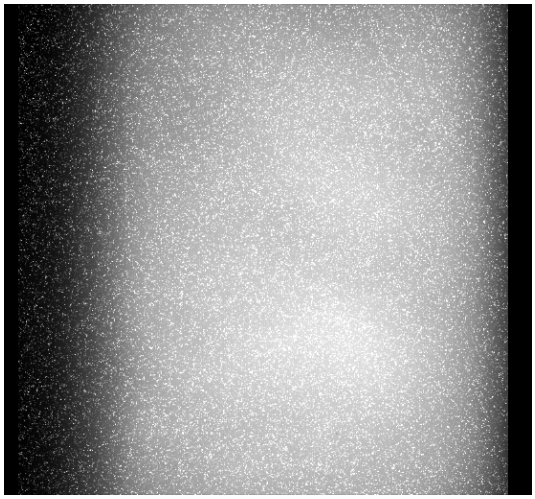

Figure 8.7: Intensity distribution of the primary neutron beam in 47 cm distance from the outlet window. Its size is 27 cm x 27 cm divided into 552 x 512 pixels.

Spatial distribution

The spatial distribution was determined using a CCD camera system in combination with a scintillator of 30 cm x 30 cm [Buc01]. The distance between source (outlet window) and scintillator was 47 cm, the integration time 3600 s. The resulting raw-image (Fig. 8.7) shows a relatively homogeneous distribution within an area of 27 cm height and 12 cm width. The white spots are caused by gamma-rays directly hitting the CCD, essentially originating from the surrounding. Improved shielding of the (unshielded) detector system and taking a series of short time images which are then image processed (e.g. median filtering) drastically improve the image quality (Fig. 8.8).

First radiographs

The data of the figures showed next are white spot corrected by means of median filtering, but not normalized yet.

Figure 8.8 shows the primary spatial neutron distribution in a distance of 47 cm from the outlet window. It is derived from 10 radiographs, each measured with an integration time of 1000 s (The integration time may be reduced by a factor of 10 for routine

application without considerable loss of information, i.e. typically 100 s). A comparison with Fig. 8.7 demonstrates the need of image processing for filtering out white spots, but also the good homogeneity of the spatial neutron distribution.

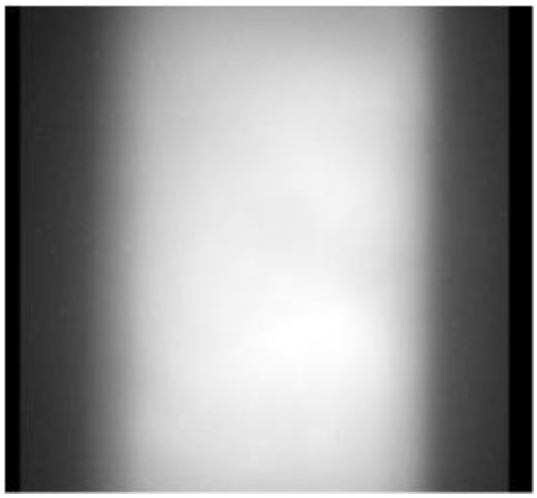

Figure 8.8: Intensity distribution of the primary neutron beam in 47 cm distance from the outlet window.

To demonstrate the basic characteristics of applying the SbBe source together with the CCD detector system Figure 8.9 shows the radiography of a step wedge, set up from polyethylene, aluminum, iron and lead, each material being 2.5 cm in width. The step size is 1 cm in height and 0.5 cm in depth with 10 steps in total. The image (Fig. 8.9) is based on 10 single radiographs each measured with an integration time of 1800 s. The distance between source (outlet window) and detector was 30 cm. Although a number of steps can be identified the influence of beam divergence (basically in vertical direction) becomes obvious and has to be considered in further interpretations.

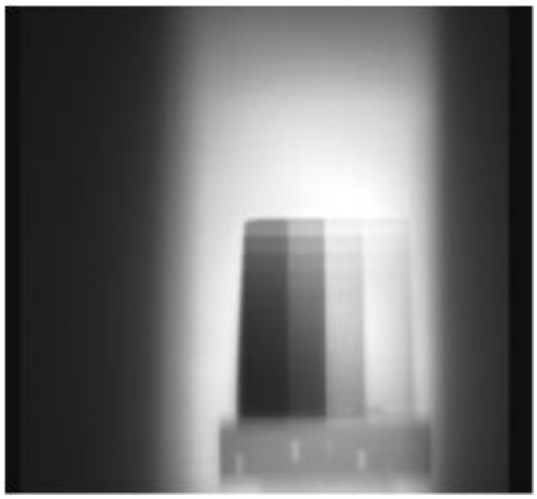

Figure 8.9: Radiography of a step wedge made out of polyethylene, aluminum, iron and lead (from left to right).

The main operational area of the Sb-Be source will be the characterization of objects consisting of shielding containers (e.g. lead container) with inner structures (e.g. containers of radioactive sources). As a first test, a lead cylinder (8 cm height, 4 cm diameter, 0.7 cm wall thickness) was radiographed. The inner structure was simulated by an europium source sealed in a steel cylinder (7 cm height, 1 cm diameter, 0.13 cm wall thickness). The lid of the shielding container was slightly open. The result combining 10 radiographs by median filtering is shown in Fig. 8.10. The integration time for each radiograph was 3600 s, the distance between source and detector 30 cm. From Fig.8.10, one can get valuable information necessary for judging the composition and hazardousness of the object.

Fig. 8.10: Shielding container (lead) with slightly opened lid containing a cylindrical europium source.

A shielding container with increased wall thickness (2 cm) was investigated in the next step. It is 9 cm in height and 7 cm in diameter. To simulate an inner structure a ball-point pen was partially placed inside. Only 4 radiographs (integration time 1000 s) have been processed by median filtering resulting in Fig. 8.11. The distance between source and detector was 30 cm. From Figure 8.11 the dimensions of the lead container can be clearly determined. The simulated inner structure, the ball-point pen, can be seen outside the shielding container as well as inside, although the contrast for the latter is not very high.

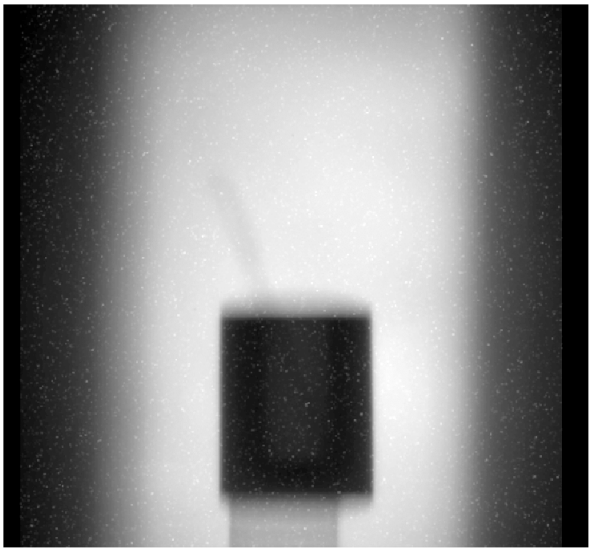

Figure 8.11: Lead container (wall thickness 2 cm) with ball-point pen.

8.5 Conclusion

In all measurements the outlet window was empty, i.e. no collimation of the neutrons takes place within this short distance. This leaves future possibilities for further optimisation of the neutron beam parameters. Especially the reduction of the gamma ray background using some lead filter, although these are already discriminated by the scintillator screen of the detector system used, and an improved collimation, thus reducing the divergence, may be optimized.

The prototype Sb-Be source in its actual status already proofed to fulfill the requirements of the authorities for the inspection of heavy element shielded objects.

Chapter 9: Conclusions

In the current study various new experimental methods and computation procedures in the field of neutron radiography and tomography are presented. Some of the obtained results are reported world-wide for the first time. The most significant contributions of the current thesis to the further development of the neutron radiography and tomography can be named as following:

1. The performance of phase contrast radiography for the first time with a polychromatic thermal neutron beam.
2. The first world-wide utilization of a neutron velocity selector for the purpose of energy-selective neutron radiography and tomography.
3. The first neutron topography measurements at the spallation source SINQ at Paul Scherrer Institute, Switzerland.
4. The development of a computation procedure based on the powerful Monte Carlo code for particle transport – MCNP for a correction of the neutron scattering contribution to radiography images.

At the phase contrast imaging the phase shifts induced by the neutron propagation through the sample are transferred to intensity variations detected by a position sensitive detector – an imaging plate. For this purpose a thermal neutron beam with a high transversal spatial coherence was used. The higher beam intensity due to the polychromatic beam allows shorter exposure times. The presented examples in Chapter 2 show that for some defined cases the neutron phase contrast radiography appears as the only possible experimental technique for a sample visualisation. The resulting edge-enhancement makes the technique attractive for investigations of objects with finer structure and low absorption properties. The obtained promising results will accelerate the further development of this method.

The energy selective cold neutron radiography and tomography were performed with a partial monochromatisation of the primary neutron beam using a neutron velocity selector. This allows to gain more intensity in comparison with the crystal monochromator technique. So the radiography exposure time reaches reasonable values.

The presented experiments in Chapter 3 show that the image contrast can be changed applying beams with different energy spectra exploiting the energy dependent neutron attenuation properties of the materials. The performance of radiography experiments below and above the Bragg cut off of a defined crystalline material makes it possible to extract additional non-trivial information about the investigated sample. The tomography investigations with different neutron spectra modified by the velocity selector show for the first time how the neutron beam spectrum influences the quality of the reconstructed images. The future of this method is connected with the development of the neutron radiography technique at the next generation pulsed neutron sources as ESS where better energy resolution and higher intensity can be achieved by an utilization of a time of flight technique for the beam monochromatization.

In the current study the challenges of neutron topography are also presented where the development of a topography visualisation system is shown in Chapter 4. The system was used for the solution of some practical tasks as testing of single crystals intended for neutron monochromators for the new instruments at FRM II and for a sample preparation where a single crystal area was separated from a polycrystalline object. The current state of the art in the so developed topography setup opens the possibility for further experiments as the so-called topo-tomography where a tomography reconstruction from the collected topography images is available. So the three-dimensional visualisation of crystal and magnetic domains will be possible.

The included calculation procedures in this study for simulations of real radiography experiments are based on the powerful MCNP Monte Carlo code for the simulation of a particle transport. Examples of complete simulated experiments are shown in Chapter 5. The simulation of the scattered neutron contribution to the radiography imaging for different materials and geometric parameters was used as a base for a correction procedure of real images. The comparison between simulated and experimental data allows to understand in detail the neutron transmission process in case of strongly absorbing materials (borated steel). The contribution of such secondary effects as beam hardening, material heterogeneity and background are estimated.

The MCNP simulations were used for the solution of a current problem of nowadays radiography – the development of a mobile neutron radiography setup. The presented investigation concerns a mobile neutron source based on the Sb-Be (γ,n) reaction. All the processes from the design through the optimisation and the setup construction until the final test images are presented in details in Chapter 8.

Some of the innovations described in the current study will be used at the forthcoming radiography facilities of the new research reactor FRM II in Munich, Germany.

Appendix A: Characterization of the Beam Divergence in Neutron Radiography

The beam divergence is a very important parameter for every radiography facility. It defines the maximal spatial resolution which can be achieved with an ideal detector possessing an infinite resolution. The divergence angle α at the sample position is determined by the radiographic experimental geometry as shown in Fig. A1.1.

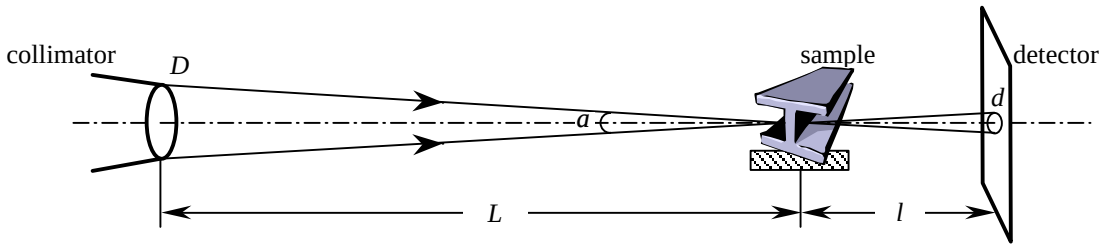

Figure A1.1: Schematic representation of a radiographic experimental geometry

In this case one can say that the divergence is defined by the angle under which the opening of the collimator is seen from the sample position. Then the divergence angle can be written as:

$$\tan\alpha = \frac{D}{L} = \frac{1}{L/D},$$

where D is the diameter of the collimator diaphragm in the beam path and L is the diaphragm to sample distance. Since L and D are geometrical parameters which can be measured simple for every classical radiography facility, the ratio L/D is chosen for the convenience to be a measure of the beam divergence. In these terms the projection of an infinitesimal volume element of the sample on the detector plane will define the image blurring as:

$$d = \frac{l}{L/D},$$

where l is the sample to detector distance and d is the circle spot on the detector plane which corresponds to a infinitesimal volume element. So the larger the *L/D* ratio, the sharper will be the radiography image. At a fixed sample position this can be realised either with a small collimator diaphragm or with a closer sample to detector distance. Both solutions have their disadvantages as for the first case a lot of intensity will be lost while in the second case a lot of scattering radiation will fall in the detector range which will additionally blur the radiography image.

In the case of neutron radiography where neutron optics equipment like a neutron guide or neutron lenses is used the beam divergence is no more defined by the corresponding *L/D* ratio. The reason is that these devices produce energy dependant divergence because of the neutron reflection from special prepared "mirror" surfaces where the reflection angle depends on the neutron energy. So at the end of a neutron guide the beam divergence is given by the critical reflection angle g_c of the "mirror" walls. The divergence stays constant in the guide cross section as shown in Fig. A1.2.

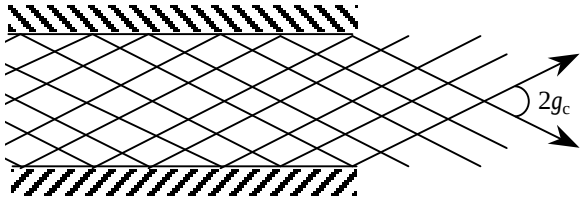

Fig. A1.2 Schematic representation of a beam geometry at a neutron guide

The critical angle g_c is proportional to the neutron wavelength [Lei63]. For a neutron guide coated with natural nickel it is $g_c = 0.1^o/Å$. In this case if the neutron beam spectrum is known the critical angle can be approximately taken for the arithmetic mean value of all presented wavelengths. So an effective *L/D* ratio can be calculated as $L/D = 1/\tan(2g_c)$.

Further information can be found in [Sch01a] and in Chapter 3 of the current study.

References

[All00] B. E. Allman, P. J. McMahon, K. A. Nugent, D. Paganin, D. L. Jacobson, M. Arif, S. A. Werner, Nature, vol. 408, 9 November 2000, 158-159.

[Bae02] S. Baechler, B. Masschaele, P. Cauwels, M. Dierick, J. Jolie, T. Materna, W. Mondelaers, Nucl. Instr. and Meth. A 481 (2002) 38.

[Bae02a] S. Baechler, N. Kardjilov, M. Dierick, J. Jolie, G. Kühne, E. Lehmann, T. Materna, New features in cold neutron radiography and tomography, Part I: Thinner scintillators and a neutron velocity selector to improve the spatial resolution, (in print) Nuclear Instruments and Methods 2002.

[Baj00] S. Bajt, A. Barty, K. A. Nugent, M. McCrtney, M. Wall, D. Paganin, Ultramicroscopy 83 (2000), 67-63.

[Bar78] J. Baruchel, M. Schlenker, A. Zarka, J. F. Petroff, Neutron diffraction topographic investigation of grouth defects in natural lead carbonate single crystals, Journal of Crystal Growth 44 (1978), pp. 356-362

[Bar80] J. Baruchel, M. Schlenker and B. Barbara, Antiferromagnitic domains in MnF_2 by neutron topography, Journal of Magnetism and Magnetic Materials 15-18 (1980), pp. 1510-1512.

[Bar98] A. Barty, K. A. Nugent, D. Paganin, A. Roberts, Optics Letters, Vol. 23, No. 11, June 1, 1998, 817 – 819.

[Bau98] G.S. Bauer, Nucl. Instr. and Meth. B **139** (1998) 65.

[Bay99] G. Bayon, Nucl. Instr. and Meth. A 424 (1999) 92.

[Boe75] A. Boeuf, S. Lagomarsino, F. Rustichelli, J. Baruchel and M. Schlenker, White beam neutron topography, Phys. Stat. Sol. A 31, 1975, pp. K91.

[Bor59] M. Born, E. Wolf, Principles of optics, Pergamon press, 1959, p. 423

[Bri96] J. Briesmeister (Ed.), MCNP – A General Monte Carlo N-Particle Transport Code, Version 4B, Los Alamos National Lab.,Los Alamos, 1996.

[Bro23] L. de Broglie, Comptes rendus de l'Académie des Sciences, vol. 177, pp. 507-510 (1923)

[Bry78] J. W. Bryson, J. C. Lee, and R. R. Burn, Calculation of Neutron Transmission Through Boral Shielding Material, Transaction of American Nuclear Society, Vol. 30, pp. 596-597, 1978.

[Buc95] T. Bücherl, E. Steichele, Computerized tomography with thermal neutrons, International Symposium on Computerized Tomography for Industrial Applications, June 8-10, 1994 Berlin, 1995, pp. 49-56.

[Buc01] T. Bücherl, Ch. Lierse von Gostomski, E. Calzada, The NECTAR Facility at FRM-II: Status of the Set-Up of the Radiography and Tomography Facility using fast Neutrons, Proc. 7th World Conference on Neutron Radiography, Rome, Italy, 15.-20. September 2002.

[Bur58] W.R. Burrus, How Channeling Between Chunks Raises Neutron Transmission Through Boral, Nucleonics, 16, 1, 91, 1958.

[Cas98] Bestimmung von spaltbaren Stoffen in Abfallproben durch Neutroneninterrogation, Jül-3498, January 1998, ISSN 0944-2952.

[Clo96] P. Cloetens, R. Barret, J. Baruchel, J. Guigay, M. Schlenker, J. Phys D: Appl. Phys. 29 (1996) 133-146.

[Clo99] P. Cloetens, W. Ludwig, J. Baruchel, J. Guigay, P. Pernot-Rejmankova, M. Salome-Pateyron, M. Sclenker, J. Bufferie, E. Maire, G. Peix, J. Phys D: Appl. Phys. 32 (1999) A 145-151.

[Cow75] J. M. Cowley, Diffraction physics, Amsterdam: North-Holland, 1975.

[Dom92] Domanus, J. C. (Ed), 1992. Practical neutron radiography. Kluwer Academic Publishers, Dordrecht, ISBN 0-7923-1890-9.

[EXFOR] For further information see, Experimental Nuclear Reaction Data File (EXFOR [CSISRS]), http://www-nds.iaea.or.at/exfor/

[Fri89] H. Friedrich, V. Wagner and P. Wille, A high-performance neutron velocity selector, Physica B 156&157 (1989), pp. 547-549.

[Fuj89] Fujishiro, M., et al., 1989. Application of 124Sb-Be neutrons to CT for iron products. Neutron radiography: Proceedings to Third Word Conference, Osaka, Japan, May 14-18, Kluwer Academic Press (1990), ISBN 0-7923-0832-8.

[Gao97] Jun Gao, "Modeling of Neutron Attenuation Properties of Boron-aluminum Shielding Materials," M.S. thesis, University of Virginia, August 1997.

[Gry00] Gryaznykh, D. A., Lykov, V. A., Plokhoi, V. V., 2000. Estimation of neytron yield from beryllium target irradiated by Spring-8 hard synchrotron radiation, NIM A 448 (2000).

[Gue95] T. Gureyev, A. Roberts, K. Nugent, Partially coherent fields, the transport-of-intensity equation, and phase uniqueness, J. Opt. Soc. Am. A, vol. 12, No. 9, 1942-1946.

[Har86] A.A. Harms, D.R. Wyman, Mathematics and Physics of Neutron Radiography, Reidel, Dortrecht, 1986.

[Ike96] Y. Ikeda, M. Yokoi, M. Oda, et al., Nucl. Instr. and Meth. A 377 (1996) 85.

[Kar01] N. Kardjilov, B. Schillinger, E. Steichele, Energy-selective neutron radiography and tomography at FRM, submitted to J. Apll. Rad. Isotopes (2001).

[Leh99] E. Lehmann, P. Vontobel, L. Wienzel, Properties of the Radiography Facility NEUTRA at SINQ and its Potential Use as European Reference Facility, 6th Word Conf. on Neutron Radiography, Osaka, 1999.

[Leh02] E. Lehmann, P. Vontobel, N. Kardjilov, Applied Radiation and Isotopes 2002, acc. p. (in print).

[Lei63] Maier-Leibnitz, H., Springer, T., 1963. The use of neutron optical devices on beam-hole experiments, Nuclear Science and Technology (Journal of Nuclear Energy Parts A/B), vol. 17, pp. 217-225.

[McD99] T.E. McDonald Jr., T.O. Brun, T.N. Claytor, E.H. Farnum, G.L. Greene, C. Morris, Nucl. Instr. and Meth. A 424 (1999) 235.

[Mor92] C.A. Mora, J.S. Brenizer, Jr., in: Proc. Of the 4th World Conf. On Neutron Radiography, May 1992, San Francisco, USA, pp. 791-800.

[Neg92] Negin, C. A., Werku, G., 1992. MicroShield User Manual. Grove Engineering Inc., Rockville, Maryland, USA

[Oda96] M. Oda, M.Tamaki, K. Takahashi, K. Tasaka, Nucl. Instr. and Meth. A 379 (1996) 323.

[Ped62] F. L. Pedrotti, L. S. Pedrotti, Introduction to optics, Prentice-Hall, Inc., 1962

[Ple99] H. Pleinert, S. Koerner, E. Lehmann, Nucl. Instr. and Meth. A 424 (1999) 177.

[SANS] For further information see http://sans.web.psi.ch/SANSDoc/node35.html#nvs

[Sch96] Schillinger, B., 1996. 3D Computer tomography with thermal neutrons at FRM Garching, J. Neutron Research, vol. 4, pp. 57-63.

[Sch01] Schillinger, B., 2001. Improved radiography and 3D tomography due to better beam geometry, Nondestr. Test. Eval., vol. 16, pp. 277-285, Gardon & Breach.

[Sch01a] Schillinger, B., 2001. Estimation and measurement of L/D on a cold and thermal neutron guide, Nondestr. Test. Eval., vol. 16, pp. 141-150, Gardon & Breach.

[Schl75] M. Schlenker, J. Baruchel and R. Perrier de la Bathie, Neutron-diffraction section topography: Observing crystal slices before cutting them, J. Appl. Phys., Vol. 46, No. 7, July 1975, pp. 2845-2848.

[Schl78] M. Schlenker, J. Baruchel, Neutron techniques for the observation of ferro- and antiferromagnetic domains, J. Appl. Phys 49 (3), March 1978, pp.1996-2001

[SINQ] For further information see: http://sinq.web.psi.ch/sinq/instr/topsi.html

[Tea83] M. R. Teague, J. Opt. Soc. Am., vol. 73, No. 11, November 1983, 1434-1441

[Une98] H. Unesaki, T. Hibiki, K. Mishima, Nucl. Instr. and Meth. A 413 (1998) 143.

[Une98a] H. Unesaki, T. Hibiki, K. Mishima, Nucl. Instr. and Meth. A 405 (1998) 98.

[Wag92] V. Wagner, H. Friedrich and P., Performance of a high-tech neutron velocity selector, Physica B 180&181 (1992), pp. 938-940.

[Wag98] W. Wagner, G.S. Bauer, J. Duppich, S. Janssen, E. Lehmann, M. Lüthy, H. Spitzer, J. Neutron Res. 6 (1998) 249.

[Wel87] A. H. Wells, D. R. Marnon, and R. A. Karam, “Criticality Effect of Neutron Channeling Between Boron Carbide Granules in Boral for a Spent-Fuel Shipping Cask,” Transactions of American Nuclear Society, Vol. 54, pp. 205-206, 1987.

[Wil96] S. W. Wilkins, T. Gureyev, D. Gao, A. Pogany, A. W. Stevenson, Phase-contrast imaging using polychromatic hard X-rays, Nature, vol. 384, 28 November 1996, 335-338.

[Wro99] T. Wroblewski, E. Jansen, W. Schäfer, R. Skowronek, Neutron imaging of bulk polycrystalline materials, Nucl. Instr. and Meth. A 423 (1999) 428.

[Wro00] T. Wroblewski, J. Almanstötter, O. Clauss, M. Moneke, T. Pirling, P. Schade, Materials Science and Engineering A 288 (2000) 126-131

Publications

1. N. Kardjilov, E. Lehmann, P. Vontobel, Representation of the image formation in applied neutron radiography in terms of a PSF superposition, Appl. Phys. A 74 [Suppl.], S228–S230 (2002).

2. S. Baechler, N. Kardjilov, M. Dierick, J. Jolie, G. K.uhne, E. Lehmann, T. Materna, New features in cold neutron radiography and tomography Part I: thinner scintillators and a neutron velocity selector to improve the spatial resolution, Nuclear Instruments and Methods in Physics Research A 491 (2002) 481–491.

3. N. Kardjilov, S. Baechler, M. Bastürk, M. Dierick, J. Jolie, E. Lehmann, T. Materna, B. Schillinger, P. Vontobel, New features in cold neutron radiography and tomography Part I: Applied energy-selective neutron radiography and tomography, accepted for publication in Nuclear Instruments and Methods in Physics Research A 501 (2003), 536–546

Acknowledgements

To all who have contributed to the successful completion of this work I would like to warmly thank.

First of all I would like to thank Prof. Dr. W. Gläser for the opportunity to be a member of his excellent scientific group (E21). The profound approach of Prof. Gläser to the physical phenomena, demonstrated in the regular seminars of the group, had a strong pedagogical influence on me. I am grateful to Prof. P. Böni for accepting me in his new group and for supporting me at my experimental work at Paul Scherrer Institute in Switzerland. The dynamical discussions with him about non-trivial experimental problems were invaluable for my further motivation.

During my PhD studentship in E21 I have received a great support and understanding from my supervisor Dr. B. Schillinger. His high motivation and efficiency were very impressive. Dr. Schillinger not only led efficiently my experimental work and data analysis but also had an essential tutorial influence on my result representation skill. I want also to thank him for correcting and revising this thesis.

I am thankful also to my co-supervisor Dr. E. Steichele for the brilliant ideas which were realised in the phase-contrast and energy-selective radiography experiments. For me it was a great chance to be in touch with his versatile knowledge and respectable experience.

The performance of the present PhD would not be possible without the high-quality education offered in the Physics and Chemistry Departments of the Sofia University. For basics in Nuclear Physics and X-ray non-destructive analysis I want to acknowledge Prof. Dr. Tz. Bonchev and Dr. St. Peneva.

Special thanks to the members of the neutron radiography group at the Paul Scherrer Institute in Switzerland: Dr. E. Lehmann, Dipl. Ing. P. Vontobel and G. Frei for the excellent collaboration and for their tireless enthusiasm and motivation. They supported me permanently in my experimental and data evaluation work at PSI.

Warm thanks to my colleagues Dr. B. Masschaele and M. Dierick from the University of Gent, Belgium as well as Dr. S. Baechler from the University of Fribourg,

Switzerland who participated in the performance of key experiments concerning energy-selective radiography and neutron topography. I am also obliged to Dr. J. Stahn who made possible the topography measurements at the two axis diffractometer TOPSI at PSI.

For the realisation of the mobile neutron source project I want to thank Dr. Th. Bücherl for guiding this project and Dipl. Ing. Elbio Calzada for the invested time and efforts designing and optimising the technical details.

I am grateful to Dipl. Ing. M. Bastürk from Atominstitut, Vienna and to F. deBeer from NECSA, South Africa for the fruitful collaborations in the field of Monte Carlo simulations and quantitative neutron radiography investigations.

For the great atmosphere and all the help I want to thank to the former and current members of E21 in particular: Dr. J. Felber, Dr. A. Fleischman, Dr. R. Gähler, Dr. Th. Keller, F. Grünauer, J. Brunner, M. Bleuel and C. Skorski.

I am obliged to the Osteuropäischezentrum at TU München and especially to the head of the Centre Dr. V. Koch for recommending me to Prof. Gläser as a PhD student and for the help in the beginning of my stay in Munich.

Special thanks I owe to my parents Maria and Dimitar Kardjilovi for their love and support during all my study.

Last but not least I thank my wife Daniela Kardjilova. She is the only one who really knows how much time and work was invested by this thesis. She never complained but was always there for me.